

ABSTRACT

Title of Thesis: MECHANICAL DESIGN OF DEXTEROUS
 MANIPULATOR LINKS

Christopher James Carlsen
Master of Science, 2018

Thesis directed by: Dr. David L. Akin
 Aerospace Engineering

This paper explores the challenges of dense structure-electronics packaging, specifically for a structural and electronics upgrade to the Ranger Tele-robotic Shuttle Experiment (RTSX) manipulators at the University of Maryland (UMD). Long serial-link manipulators are popular in the space industry, where the need for a long reach and high manipulability outweighs the need for high tip stiffness. For larger systems with co-located electronics, such as those used to berth vehicles on orbit, electronics packaging is not inhibited by the diameter of the link body. As link diameter decreases, co-locating electronics in the manipulator becomes difficult without adding external extensions to house them. In such densely packed bodies, the control electronics are so integrated with structure that electronics maintenance requires disassembly of primary structure.

MECHANICAL DESIGN OF DEXTEROUS MANIPULATOR LINKS

by

Christopher James Carlsen

Thesis submitted to the Faculty of the Graduate School of the
University of Maryland, College Park in partial fulfillment
of the requirements for the degree of
Master of Science
2018

Advisory Committee:
Professor Dr. David Akin, Chair
Professor Dr. Norman Wereley
Professor Dr. Mary Bowden

© Copyright by
Christopher James Carlsen
2018

Preface

Choosing a design based thesis has given me the opportunity to produce a working system, in addition to the academic studies and rigor involved in any thesis or dissertation. During my term at the University of Maryland College Park I devoted my time nearly equally to academic course work and engineering design. The design work detailed in this paper has been my most rigorous exercise yet, encompassing several years of effort from both myself and my teammates at the Space Systems Laboratory.

This paper is a demonstration of my own skills as well as the capabilities of my peers. I am building upon the work, lessons learned, and creativity of a multitude of people across multiple decades. The robot that I redesign in this thesis was conceived, designed, and constructed by a group of highly skilled and dedicated people years before I entered the university. My formative years in my undergraduate career were spent learning from the design of Ranger and the mountain of documentation that accompanies it. While I spend several chapters in this thesis analyzing and critiquing the decisions made by the creators of Ranger, I do so having the benefit of hindsight and wish to convey my utmost appreciation for the efforts expended before me.

This thesis is also meant to be a reference text for my successors at the Space Systems Laboratory, hopefully shedding some light into the inner workings of Rangers design. To those students, I wish you good luck. I hope this is what you need.

Dedication

This thesis is dedicated to my late mother, Ann. She was there for every event in my life, big or small. She drove me to do my best where ever I could, and see the beauty in the world around me as often as I could.

Thank you so much.

Table of Contents

Preface	ii
Dedication	iii
List of Tables	viii
List of Figures	ix
List of Abbreviations	xiii
1 Thesis Motivation	1
1.1 Introduction	1
1.2 Benefits of the Selected Commercial Motor Controllers	2
1.3 Challenges from the Selected Commercial Motor Controllers	3
1.4 Motivation Summary	3
2 RTSX Overview	5
2.1 Overview	5
2.2 Internal Wiring	8
2.3 Design Space Details	10
3 Introduction of New Motor Controllers	13
4 Design Requirements	15
4.1 Initial Requirements	15
4.2 Post-Prototype Additions and Alterations	16
4.3 Prototype Lessons Learned	16
4.4 Materials Used	17
5 Controller Packaging Experiment	19

6	Design Methods	25
6.1	Bottom-Up Design	25
6.2	Top-Down Design	26
6.3	Part Tree Generation	26
6.4	Design Methods Conclusions	28
7	Second Design Revision Method	29
8	Structural Analysis	34
8.1	Analysis Assumptions	34
8.2	Gearbox Stiffness	35
8.3	Analysis of Original System	36
8.4	Prototype Link Layout	37
8.5	Prototype Analysis	38
8.6	Conclusions	41
9	Structural Inclusion of the Lid	42
9.1	Structural Connection Attempt	42
9.2	Bolted Lid Analysis	44
9.3	Calculating Bolt Forces	44
9.4	Determining Parent Material Geometry	48
10	Stiffness Analysis of Non-Axisymmetric Beams	49
10.1	Verification of Model	50
10.2	Evaluation of Characterization Data	53
10.3	Influence of Tool Tip Stiffness	55
10.4	Conclusions	56
10.5	Potential for Future Work	57
11	Tray Geometry Optimization Study	58
11.1	Varied Wall Thickness	59
11.2	Flange	59
11.3	Orthogrid	60
11.4	Isogrid	61
11.4.1	Base Geometric Design	62
11.4.2	External Mounting Points	63
11.5	Optimization Method	64
11.6	Conclusions	66
12	RTSX Standard Internal Interface	67
12.1	Load Transfer	69
12.2	Surface Pressure	71
12.3	Reducing Thermally Induced Stress	72
12.4	Fatigue	73
12.5	Galvanic Corrosion	74

13	Thermal Analysis of Original RTSX Design	77
13.1	Critical Components of Original Design	77
13.2	Design Comparison to VPX Standard	79
13.3	Preliminary Inspection	80
13.4	Failure Theory	81
13.4.1	PCB Flexure	81
13.4.2	Excessive Mating Pressure	81
13.4.3	Motor Driver Failure	82
13.4.4	Separation of the Heat Spreader from the Card Cage	82
13.4.5	Separation of Heat Spreader from Motor Driver	82
13.5	Steady State Thermal Design Investigation	83
13.6	Contact Pressure Evaluation	84
13.7	Failure Method Review	88
13.7.1	PCB Flexure	88
13.7.2	Excessive Mating Pressure	88
13.7.3	Motor Driver Flexure	88
13.7.4	Separation of Heat Spreader from the Card Cage	89
13.7.5	Separation of Heat Spreader from the Motor Driver	89
13.8	Conclusions	89
14	Thermal Redesign	92
14.1	Mechanical Isolation	92
14.2	Retaining Arm Design	94
14.2.1	Deformation Method	95
14.2.2	Material Selection	96
14.3	Thermal Transfer Between HPU and Link Body	96
15	RTSX Thermal Design Evaluation	98
15.1	Operating Environment	98
15.2	Design Challenges	99
15.3	Thermal Design Solutions	100
15.3.1	Built-In Heatsink	100
15.3.2	Bolt-On Heatsink	100
15.3.3	Thermal Electric Cooler	101
15.3.4	Active Cooling	102
15.4	Impinged Nozzle Flow Design	102
15.5	Fabrication	108
16	Thermal Verification and Testing	110
16.1	Test Hardware	110
16.2	Thermal Testing Results	113
16.2.1	Junction Resistance	113
16.2.2	First Order Calculation of Steady State Values	115
16.2.3	Passive Convection Performance	117
16.2.4	Forced Air Convection Performance	118

16.2.5 Internal Radiative Heating	119
16.3 Thermal Design Conclusions	119
17 Internal Electronics Mounting	121
17.1 Rack Construction Concepts	122
17.1.1 Externally Framed Rack	122
17.1.2 Monolithic Internally Framed Rack	124
17.1.3 Built-Up Internally Framed Rack	124
17.2 Structural Analysis	125
17.3 Wire Harnessing Consideration	128
17.4 Parallel Design Development with Electronics Designs	129
17.5 Electronics Mounting Conclusions	130
18 Link Extension Design	132
18.1 Thin Walled Beam	132
18.2 Link Extension Interface	134
18.3 Link Extension Design	135
19 Conclusions	138
Appendices	140
A RTSX DXE Kinematic Chain	141
B RTSX PXL Kinematic Chain	142
C Experimental Results Studying Minimal Parent Material Geometry About a Threaded Surface	143
C.1 Experimental Setup	144
C.2 Comparison to Expected Values	145
C.3 Conclusions	147
D Conceptual Limits for Joint Design	150
D.1 Powertrain Design	151
D.2 Piezoelectric Motors	153
D.3 Bearing Design	155
D.4 Kinematic Configuration	156
D.5 Mechanical Design	157
D.6 Design Study Conclusions	160
E Wire Harnessing Guide	162
E.1 Connector P4	162
F Interpart Connections	163
Bibliography	164

List of Tables

4.1	Commonly used materials in RTSX	18
5.1	Design constraints for RTSX links	20
5.2	HPU packaging cross sections	21
8.1	Stiffness stackup of the original and ideal links for RTSX	36
8.2	Comparison of torsional stiffness between link designs	39
9.1	Loading values for RTSX 2 bay link design	44
9.2	Stress calculated per bolt in selected configurations	48
9.3	Safety factor for bolts considered	48
10.1	Percentage error between the extended model in the compliance matrix	51
12.1	Coefficients of thermal expansion for selected materials	73
12.2	Galvanic index of materials used in RTSX	75
13.1	Steady state motor drive temperatures	84
15.1	Thermal system design requirements	99
15.2	Table of constants used in the impinged flow calculation	103
16.1	Experimental results for various thermal interface models	114
18.1	Design limits of a 0.33m link extension	134
C.1	Experimental results of test sample failure	146
E.1	Connector P4 Pinout Wire Chart	162

List of Figures

2.1	RTSX system simulating DEXTER in neutral buoyancy	5
2.2	RTSX DXE dexterous manipulator	7
2.3	RTSX's coarse positioning manipulator, PXL	9
2.4	Cross sectional view of the original RTSX DXE design	10
2.5	RTSX Configured as SPDM performing an ORU change out	11
2.6	Wrist link with sheath removed	12
3.1	Motor Drivers	14
5.1	RTSX shoulder packaging study view 1	22
5.2	RTSX shoulder packaging study view 2	22
5.3	Cross section of prototype wrist housing	23
6.1	Example part tree structure	27
7.1	Original Deisn Hierarchy	33
7.2	Redesigned Heirarchy	33
8.1	Bending of original housing	35
8.2	Cross section of prototype shoulder housing	37
8.3	Comparison of original and prototype wrist housings	38
8.4	RTSX prototype flexibility being tested	39
8.5	Final link design for RTSX	40
9.1	External view of an alternate lid design	43
9.2	Cross section view of an alternate lid design	43
10.1	Extended characteristic equation for a link	50
10.2	Characteristic compliance matrix of the final housing	53
10.3	Ideal IPM distribution	54
10.4	Original link IPM distribution	54
10.5	Prototype link IPM distribution	54
10.6	Final link IPM distribution	54
10.7	Contribution to tip deflection	55

11.1	Minimum wall geometry	58
11.2	Thickness Optimized Wall Geometry	59
11.3	Flanged Wall Geometry	60
11.4	Orthogrid lighteneing geometry	60
11.5	Isogrid lightening geometry	61
11.6	Reflective fiducial markers attached to a link	64
11.7	Isogrid geometry optimization, step 1	65
11.8	Isogrid optimization, final iteration	66
12.1	PXL electronics mounting interface	67
12.2	DXE link mounting interfaces	68
12.3	Adapters used between joint module and link bodies in RTSX	69
12.4	Thermally invariant fastener chain	73
12.5	Galvanic corrosion of the threaded holes on the base of PXL	75
13.1	Top view of the servo driver board	79
13.2	Computer rendering showing the geometry of the heatspreader	79
13.3	Bottom view of the servo driver	79
13.4	Servo drivers installed in RTSX	79
13.5	Deformed original wrist link	80
13.6	All controllers powered, Wedge-Lok conduction only	85
13.7	Single contoller powered, Wedge-Lok conduction only	85
13.8	All controllers power, conduction through the full heat spreader	85
13.9	Single controller powered, conduction through the full heat spreader	85
13.10	Unloaded heat spreader pressure distribution	86
13.11	Applied moments to a FEA link model	87
13.12	DDC module unloaded pressure	87
13.13	DDC module worst case pressure	87
13.14	Pressure loading, positive torsion	91
13.15	Pressure loading, negative torsion	91
13.16	Pressure loading, positive vertical bending	91
13.17	Pressure loading, negative vertical bending	91
13.18	Pressure loading, positive horizontal bending	91
13.19	Pressure loading, negative horizontal bending	91
14.1	Kinematic diagram of the servo driver retainer	93
14.2	Grübler's formula for calculating degrees of freedom in a mechanism	93
14.3	New servo driver contact pressure	94
14.4	New servo driver contact pressure	94
15.1	Diagram of impinged flow across a surface	103
15.2	Diagram of flowin the cooler	105
15.3	Pressure-velocity diagram for the selected fan	106
15.4	Calculated ideal impinged flow cooling per motor controller	106
15.5	Cooler assembled onto the thermal testbed	107
15.6	Cross sectional view of the cooler as applied to a link	107

16.1	Thermal test link in an enviromental chamber	111
16.2	Test electronics rack with dummy servo drivers	111
16.3	Thermal test platform being assembled	111
16.4	Rendered graphic of the mock HPU	112
16.5	Rendering of the interior of a HPU with sensor locations labeled . . .	112
16.6	First order temeperature prediction error	116
16.7	Free convection experimental results at room temparature	117
16.8	Maximum disapation from each motor controller as a funciton of ex- ternal temperature	118
17.1	Cross section of the link depicting volume allotments	122
17.2	Prototype electronics mounting rack	123
17.3	Internally framed rack with an underslung structure	124
17.4	Required Young's Modulus for a given deflection	125
17.5	Natural frequency of a massless cantilever beam with a tip mass . . .	125
17.6	Finite element simulation showing the first vibratory mode	126
17.7	Concept for a stiffening beam for the top plate	127
17.8	Final stiffening beam design	127
17.9	Wire harness path	128
17.10	Gap in the built-up structure used for harnessing	129
17.11	Electronics interface example	130
18.1	Critical thickness for the link extension	133
18.2	Proximal link extension iniface	134
18.3	Distal link extension interface	134
18.4	Cross section of the link extension assembly	136
C.1	Detailed cross section of the test sample	143
C.2	Mechanical drawing for tensile test samples	145
C.3	Index test of bolts until failure	146
C.4	Sample test results for 0.35 inch diameter billet	146
C.5	Comparison of experimental results against ideal results	147
C.6	Test sample 016 showing tensile failure	149
C.7	Test Sample 040 showing pullout failure	149
D.1	Comparison of various hypocycloidal gearbox performances	151
D.2	Baseline arrangement of components inside a robotic joint	152
D.3	Surveyed actuator torque performances	152
D.4	Standing Wave Motor	154
D.5	Traveling Wave Motor	154
D.6	Walking foot motion	154
D.7	Geometry depicting how angular contact bearings resist rocking mo- ments	156
D.8	Mockup of Strongman actuators	157
D.9	Strongman joint structural design	158
D.10	Strongman joint cross section	158

D.11 Strongman joint-link interface	159
D.12 Strongman interface detail showing sealing surfaces	159
D.13 Comparison of Strongman shoulder with RTSX DXE Shoulder	160
E.1 Connector P4 Pinout	162
E.2 Connector P4 cable cross section	162
F.1 Sample of RTSX Interpart Tree	163

List of Abbreviations

ABS	Acrylonitrile Butadiene Styrene
CNC	Computer Numerically Controlled
COTS	Commercial Off the Shelf
CTE	Coefficient of Thermal Expansion
DXE	RTSX Dexterous Manipulator
EDM	Electro-Discharge Machining
FEA	Finite Element Analysis
HDT	Heat Deflection Temperature
HPU	High Power Unit
GPIO	General Purpose In and Out
ICD	Interface Control Document
IPM	Impact Percentile Matrix
ISS	International Space Station
MJM	Multi Jet Manufacturing
MOSFET	Metal Oxide Semiconductor Field Effect Transistor
MTBF	Mean Time Between Failure
NASA	National Aeronautics and Space Administration
ORU	Orbital Replacement Unit
PCB	Printed Circuit Board
PXL	RTSX Positioning Leg
RTSX	Ranger Tele-robotic Shuttle Experiment
SLM	Selective Laser Melting
SLS	Selective Laser Sintering
SPDM	Special Purpose Dexterous Manipulator
SSL	Space Systems Laboratory
SSRMS	Space Shuttle Remote Manipulator System
STP	Standard Temperature and Pressure

TEC Thermo-Electric Cooler

UMD University of Maryland

Chapter 1: Thesis Motivation

1.1 Introduction

This thesis was constructed to formally chronicle the redesign process of structural components in a robotic system. The system in question is a multi-armed robotic manipulator, designed for mechanically servicing satellites and other such systems while on orbit. This robotic system is known as the Ranger Tele-robotic Shuttle Experiment (RTSX) platform and will be discussed at length throughout this paper.

The RTSX platform is capable of operating in space, on land, and in water with no modification. While its original application was intended for orbital operations, it has been leveraged more recently as a testing and simulation platform for neutral buoyancy and laboratory based operations. As operations moved away from the need for flight ready hardware and towards long term ground operations, there was a need to switch to commercial hardware with modern capabilities. The motion control electronics for RTSX were the most repaired physical component and they were purpose-built in-house, making them a large contributor to operational costs.

This paper focuses on the design changes that were necessary to implement commercial motion controllers in RTSX. Multiple aspects of the original design were

also improved including thermal management, maintainability, and the total system mass without impacting nominal performance.

1.2 Benefits of the Selected Commercial Motor Controllers

The commercial motor controllers selected improve the overall performance of RTSX while reducing cost and labor. These units are capable of outputting six times the original motor controller current at peak operation. This enables the larger motors of RTSX to operate at full load, allowing the full system to operate outside of a neutrally buoyant environment. This is a huge advantage for testing and development of the full system, reducing the number of operators for testing from a full dive team complement to only one operator and a safety. That reduces the total test team from approximately eight personnel to two.

The commercial motor controllers selected also have onboard processing and pre-made firmware. This means that there is low development overhead for initial deployment and increased development speed for more complex functions. However the total system capability is reduced, for example an external board needs to be added to the system to expand the general purpose I/O (GPIO) bus from the motor controllers in order to correctly read the absolute encoders used in the dexterous arms of RTSX.

1.3 Challenges from the Selected Commercial Motor Controllers

Although the commercial motor controllers have a higher power density than the existing controllers, they have a lower overall packing density. A side by side comparison of the old and new controller is shown in figure 3.1. This means that they are not able to fit into the existing volume for the motor controllers. The entire mounting structure needed to be redesigned to accommodate the commercial motor controllers. Subsequently, this meant that most of the mechanical structure of RTSX needed to be redesigned. This is the crux of this paper and the most challenging redesign component of RTSX.

Additionally, the commercial motor controllers have a much lower maximum operating temperature from the original modules. As these modules have similar thermal output, the thermal design of RTSX must be rethought. This is secondary focus of this paper, consuming several chapters.

1.4 Motivation Summary

The higher level motivation for this thesis is to improve the state of the art of robotic structure design. Most modern design work for robotics focuses on the software development, end effector design, electronics, or even actuator design. This thesis instead focuses on the design of the electronics mounting and structure of a robotic manipulator. RTSX integrates the control electronics locally to the actuators. This reduces wiring bulk, allows the joint segments to be modular and

reconfigurable, and reduces total system volume. As most robotic manipulators do not do this, it also presents a unique opportunity to lend further validity to this design style. Through better management of packing, thermal design, and structural design, this thesis aims to open up the design space for future robotic manipulators.

Chapter 2: RTSX Overview

2.1 Overview

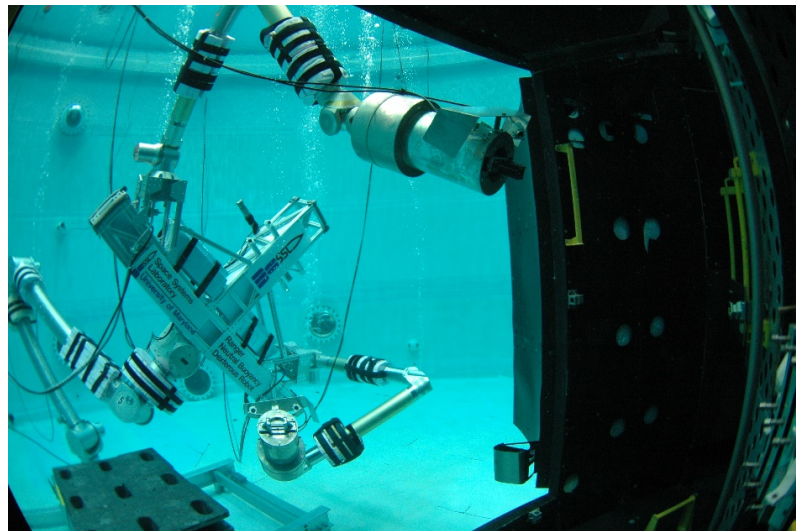


Figure 2.1: RTSX system simulating DEXTER in neutral buoyancy ¹

RTSX is designed to perform servicing tasks while on orbit. In 1992, dexterous manipulators in space were capable only of moving large components or collecting samples on surface probes. The Ranger program, created by the University of Maryland Space Systems Laboratory and sponsored by the NASA Telerobotics program, was intended to demonstrate dexterous robotics on-orbit in the near term. Originally designed for use on a dedicated free-flying servicing vehicle, it was redesigned in

¹Photo courtesy of the Space Systems Laboratory, University of Maryland

1996 to be a shuttle-based experiment. RTSX never got to fly, although the ground development/qualification unit continued to be used until 2015 as a laboratory and neutral buoyancy research system. Problems with electronics systems dying far after end-of-life and desire to switch from custom to COTS for both electronics and software were the driving factors for the redesign process.

Since the inception of the Ranger program, dexterous robotic manipulators have become much more common. A number of different solutions are commercially available for terrestrial operation. However, terrestrial robotic manipulators have far different operating requirements such as tip velocity and a tool tip stiffness that is orders of magnitude higher than space based robotic manipulators. For the purpose of this thesis, the focus will be chiefly on space based manipulator design.

Broadly, there are two different categories for space manipulators, coarse and dexterous. *Coarse manipulators* are those that move heavy loads long distances with coarse positioning and low tip stiffness, similar to a crane. An example of a coarse manipulator is the Space Station Remote Manipulator System (SSRMS), also known as Canadarm2. *Dexterous manipulators* have fine positioning control and much higher tip stiffness than coarse systems, and are generally intended to be able of performing many tasks previously reserved for humans. The Special Purpose Dexterous Manipulator (SPDM) is a dexterous manipulator system, designed to replace orbital replacement units (ORU). RTSX features one coarse and two dexterous manipulators. The coarse manipulator moves the two dexterous manipulators to their task, similar to how SSRMS moves SPDM about the International Space Station (ISS).

The dexterous arms of RTSX feature eight degrees of freedom and two powered tool drives. Although it is capable of being reassembled into multiple kinematic configurations, RTSX is typically used in an anthropomorphic configuration. Each dexterous manipulator is highly modular, and is designed as integrated shoulder, elbow, and wrist modules incorporating both actuators and electronic controllers. Each arm segment can be lengthened with simple link inserts to create the desired reach.

The following section uses the yaw-pitch-roll notation to describe the sequencing of revolute joints. These are notated as Y-P-R respectively. This notation is commonly used to give a brief description of how a serial-link manipulator behaves kinematically. For example, a Y-Y manipulator would have two joints both in the yaw plane, making it a planar manipulator. A Y-P manipulator would be for pointing to a spherical coordinate, such as you would need for a camera mount.

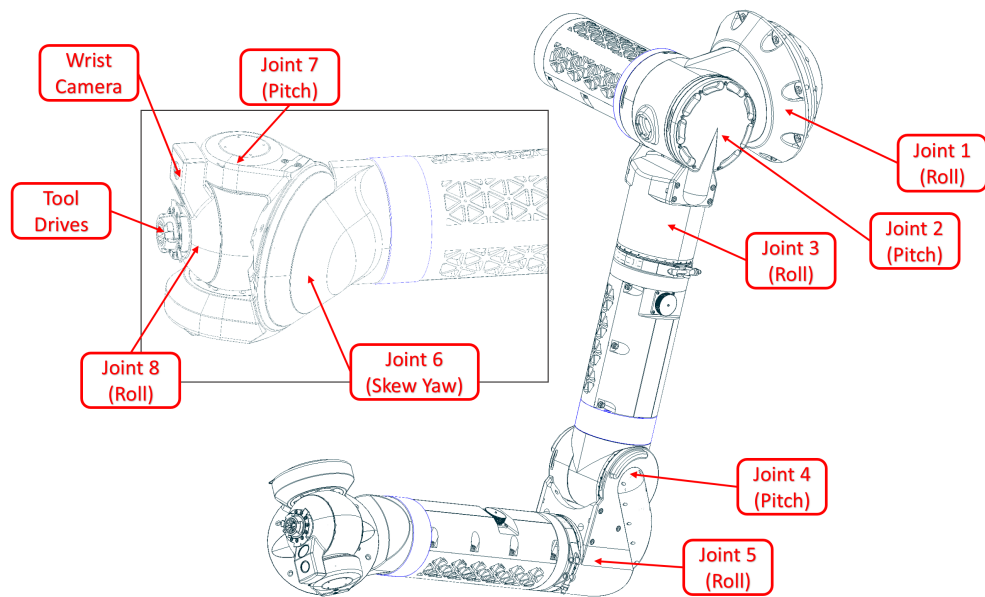


Figure 2.2: RTSX DXE dexterous manipulator

The shoulder module is built in a R-P-R configuration, giving it a simple kinematic chain. The drive electronics are not structural in this module, but attached as an external extension. The elbow and wrist modules both have their drive electronics packaged into their kinematic chain, sitting proximal to the module that the electronics control. The elbow is a P-R configuration featuring the only kinematic offset in the whole system. This offset allows the dexterous arm to fold up for launch and storage. Hidden in the image on the opposite side of the elbow are tie down points for a flight releasable bolt to hold the arm in position.

The wrist is the mechanically densest of all of the modules featuring three actuators and two tool drives. Joint 6 is non-orthogonal, mounted at a 45 degree offset, allowing the kinematic axes of joints 6, 7, and 8 to intersect. This greatly simplifies the arm kinematics mathematically.

The positioning leg of RTSX is far simpler kinematically. Each module contains two joints and an external extension housing the control electronics. PXL features a R-P-P-R-P-R configuration and is used for coarse maneuvering of the dexterous arms to a task.

2.2 Internal Wiring

All wiring for each dexterous manipulator (DXE) and the positioning leg (PXL) is internal to the manipulator. Keeping wiring internal eliminates the possibility of abrasion of cables or entanglement with the arm itself or its environment. Cabling passes through each actuator through its rotational axis inside of a shielded

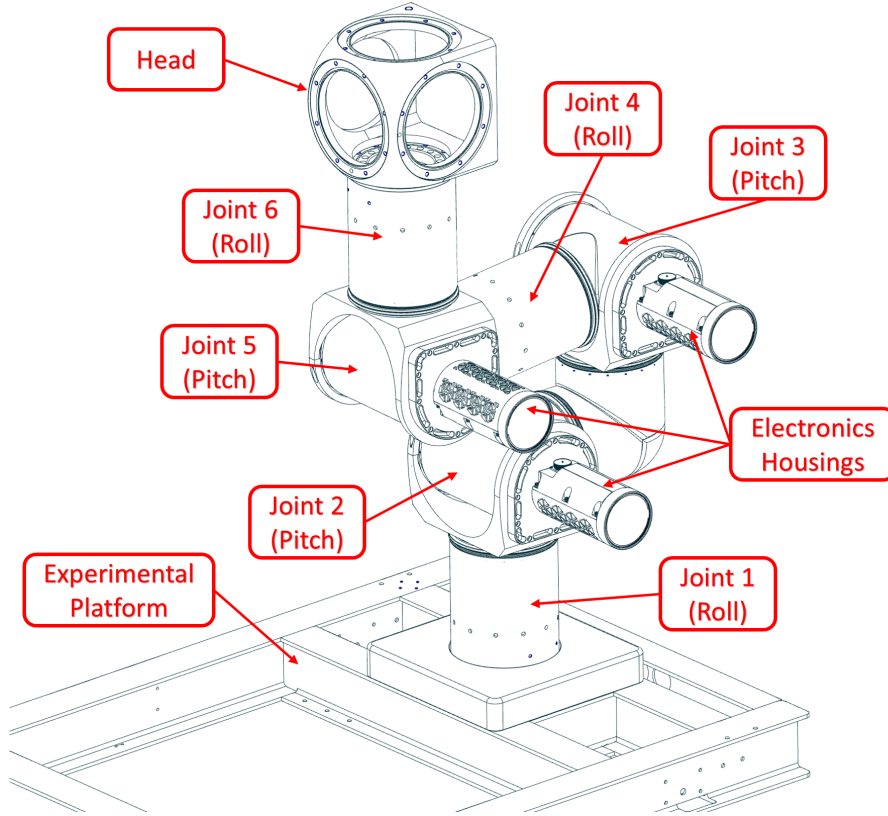


Figure 2.3: RTSX's coarse positioning manipulator, PXL

conduit. Internal wiring is limited by the geometry of the joint it passes through. In DXE, internal cable diameter is very restricted because the majority of volume in each joint is consumed by the powertrain. To make the most of this small cable pass through, motor drivers and their control electronics were packaged into the arm itself. Rather than pass all of the encoder, sensor, and motor cables through the entire length of the arm to a control box at the base, only power and a data bus are required. This also reduces problems associated with long cable runs, such as resistive losses and inductance.

The RTSX platform can have link extensions inserted between each joint module to increase its link length. With the power and data pass-through limited to

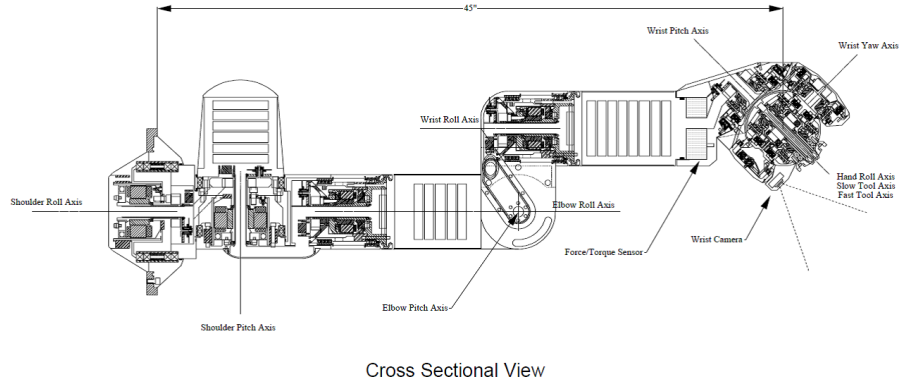


Figure 2.4: Cross sectional view of the original RTSX DXE design

a few wires, and electronics packaged in proximity to the joint modules they control, the link lengths of the arm can be modified with few modifications. The link extensions use a common mechanical interface and contain a power and data bus extension to pass through all necessary wiring. Changing the link lengths alter the kinematics of the manipulator and allows the RTSX platform to mimic the kinematics and capabilities of other manipulators on orbit or under development. In 2005, RTSX was used to mimic the kinematics of SPDM, pictured in Figure 2.5.

2.3 Design Space Details

The forearm and upper arm links of DXE are densely packed with both structure and electronics. The link is responsible for stiffly connecting proximal components to distal components, protecting the electronics housed within from the environment, and dissipating heat from those same electronics into the surrounding environment.

Difficulties arise when trying to package electronics densely with primary struc-

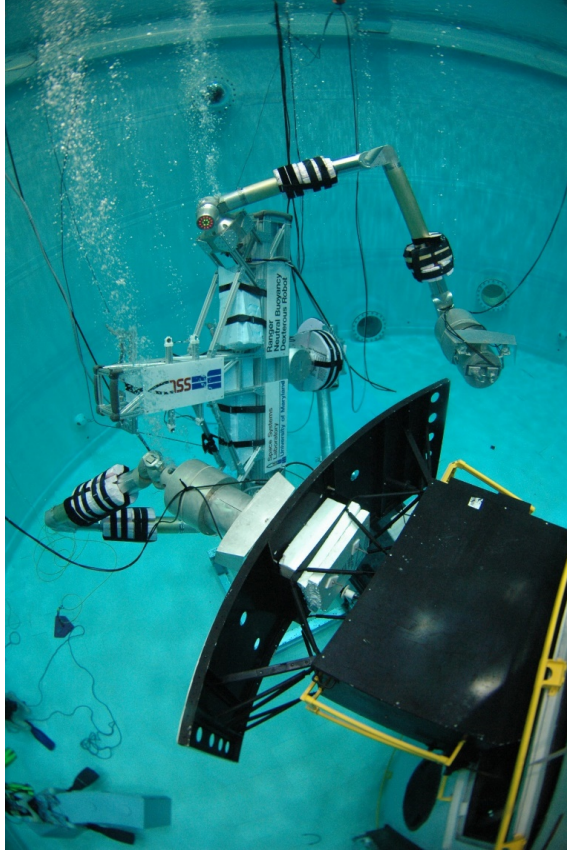


Figure 2.5: RTSX Configured as SPDM performing an ORU change out

ture. Most electronics do not do well with strain and most primary structure does not do well with large internal voids to hold electronics. In the case of RTSX, all of the link volume that was not occupied by electronics or wiring was occupied by primary structure [2.6](#). There are multiple schools of thought on whether this is a good design limit. There is no residual volume for potential design expansion, but as this was a purpose built robotic platform, is expansion volume necessary? We will explore in chapter 3 why this highly-dense layout is counterproductive to the upgrade process undertaken throughout this paper.

One downside to such a dense design was the difficulty of maintenance. For space flight hardware this is frequently not an issue, since the cost of the mass of the

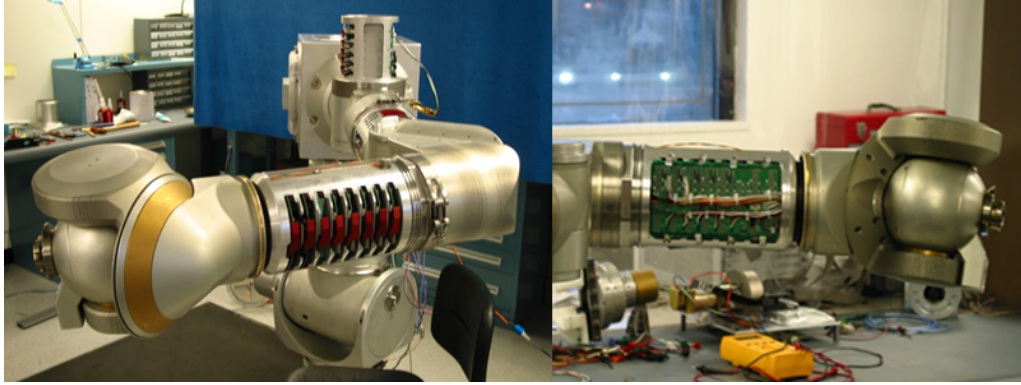


Figure 2.6: Wrist link with sheath removed. Dorsal view [left] and Ventral view [right]

design greatly exceeds the maintenance and operations costs. As RTSX transitioned in purpose from a flight experiment to a ground based testing and simulation platform, maintenance time and cost became a larger factor. The original RTSX design took measures to reduce volume and increase system reliability by limiting the number of electrical interconnects. As a result of this, the actuator wiring was soldered directly to the backplane that controls it. This can be observed in Figure 2.6 on the ventral side. This design choice was one of the largest contributors to maintenance time. In order to modify any part of the backplane, all of the connections to the PCB had to be de-soldered and tested, taking multiple days to complete.

As the links to house new electronics were redesigned, we had to keep in mind that the design goals and the design space differs from RTSXs original intent. We had to consider which design concepts to retain and which to rethink in order to produce an effective manipulator for ground testing.

Chapter 3: Introduction of New Motor Controllers

The driving cause for this redesign is the introduction of new electronic motor controller hardware. The original design used three daughter board control cards in addition to the motor driver cards. It required a DC-DC regulator card, a communications card, motion control card, and a motor driver card. Additionally, a backplane board was required to connect all of these cards together and to provide additional signal filtering. This system performed all of the requisite functions, but featured a large number of components. By extension, the large number of components in this system lead to a reduced Mean Time Between Failure (MTBF).

The original motor driver was based on a DC motor torque controller manufactured by DDC. This module was designed to withstand high temperatures and could output 10 amps of continuous current. This module was sufficient for driving any actuator in PXL and DXE, and is used as a minimal baseline for future modules. This motor driver board had no other functionality beyond supporting and driving the DDC module using the hall-effect sensors embedded in the motor stator for feedback. The actuator control loop was run on the separate motion control card.

All of this can currently be achieved on a single commercial module, available

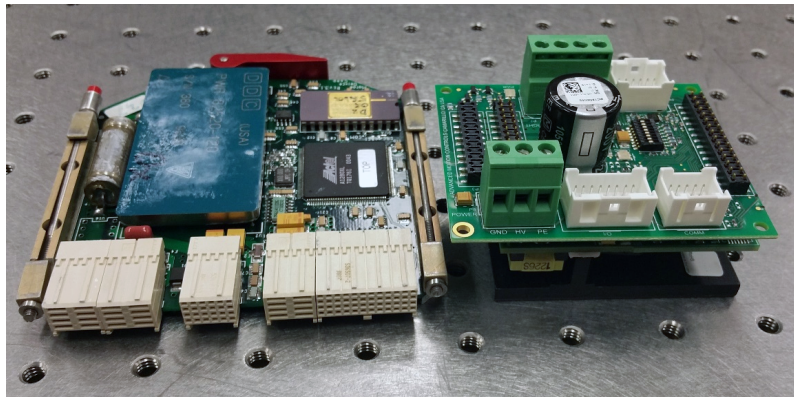


Figure 3.1: Original Motor Driver (left) and new servo driver (right)

from a variety of different manufacturers. These new all-in-one modules are referred to as servo drivers instead of motor drivers, as they have their own closed-loop control system onboard which can slew the actuator to specific positions as well as specific velocities. The module that was selected for this project is the DZCante-020L060¹ made by Advance Motion Control, capable of outputting 12 amps of continuous current.

The 12 amp module was originally specified for use with all actuators in RTSX, but an opportunity was found to increase total system performance. By using a higher power controller in joints that are subjected to higher torque, RTSX can increase in utility. By using the DZCante-060L080 in PXL and the DXE shoulder, the maximum tip load of DXE is increased and PXL is capable of operating outside of neutral buoyancy. This controller capable of supplying 30 amps of continuous current and occupies the same volume as the 12 amp module. The only difficulty created by using the 30 amp controller is an increased thermal load. Enhanced methods of cooling need to be created, and are addressed in section 16.

¹More information about this module is available at www.a-m-c.com

Chapter 4: Design Requirements

At the start of the redesign process a set of design requirements were established. These were used to create a prototype link to determine the effectiveness of the design modifications. After the prototype was completed, additions were made to these requirements using the lessons learned.

4.1 Initial Requirements

P-1 The redesign shall package all appropriate electronic hardware and motor controllers¹ into the link volume between joints in the dexterous arms, and into the side mounted volumes on the positioning leg.

P-2 The redesign shall provide an adequate operating environment for the contained electronics. This includes operation at 10 meters depth in chlorinated water.

P-3 The redesign shall be compatible with existing RTSX hardware.

P-4 The redesign shall be adequately stiff as to not impact the performance of RTSX and adequately strong as to withstand all internal forces that can be exerted by RTSX.

P-5 The redesign shall decrease maintenance time for replacing the contained elec-

tronics.

P-6 The redesign shall maintain current operable tip mass and should increase the maximum allowable top mass.

4.2 Post-Prototype Additions and Alterations

P-4a The redesign shall result in a dexterous top stiffness greater than 10 N/mm and should survive a tip force greater than 890N.

P-7 The redesign shall not exceed 137mm in diameter to eliminate self-collisions.

P-8 The redesign shall make large components common across all electronics housings to reduce manufacture tooling and setup.

P-9 The redesign shall have discrete allotments for wiring paths to avoid collisions during assembly.

4.3 Prototype Lessons Learned

Additions were made to the initial design requirements after several prototypes were completed, listed previously in section 4.2. After the prototype was constructed, a series of laboratory tests help further define the tip deflection requirement defined in P-4, resulting in the addendum P-4a. This update makes the prototype unacceptably soft, necessitating another design revision. This is addressed further in section 8.4.

¹Hence forth known as the "contained electronics"

Requirement P-7 sets a maximum link diameter. Although no self-collisions occurred during testing of the prototype links, their diameter did increase from the original design to the maximum permissible diameter. Unfortunately, additions to the design for fastening the lid to the link extended outside of this maximum permissible diameter and could have resulted in self-collisions. Operators had to be careful to not collide with these fasteners when operating the elbow joint near maximum flexion.

After the prototype housings were manufactured, an assessment was made of the overhead requirements in the machine shop. Approximately 30% of the manufacturing person-hours were expended on creating unique tooling for each independent housing. Requirement P-8 was created to reduce tooling time by creating a standard design for the bulk of the intricate components. This proved worthwhile and reduced the total component cost approximately 20%.

4.4 Materials Used

The materials in table [4.1](#) are those used for the modifications covered in this thesis. For reference, the critical parameters for each of these materials are summarized in the table.

Table 4.1: Commonly used materials in RTSX

Material	Density	Young's Modulus	Yield Strength	CTE	Thermal Conductivity
Name (alloy)	g/cm ³	GPa	MPa	$\mu\text{m}/\text{m}^\circ\text{K}$	W/m ^{°K}
Aluminum (6061)	2.7	68.9	276	23.6	167
Aluminum (6063)	2.7	68.9	214	23.4	200
Aluminum (7075)	2.8	71.7	503	23.6	130
Stainless Steel (316)	8.0	193	290	16.0	16.3
Stainless Steel (A286)	7.9	200	938	16.9	12.6
Copper (101)	8.94	117	150	17.6	390
Titanium (6AL-4V)	4.43	113	880	8.6	6.7

Chapter 5: Controller Packaging Experiment

The first priority in starting this design was to establish a coarse structure. All of the electronics housings in RTSX needed to be redesigned to accommodate new electronic hardware. While each housing could have been designed on a case-by-case basis to minimize mass across the system, this is often an expensive and marginally futile effort. Instead, a common base design was created that was capable of satisfying all design constraints and was modified for special cases.

All of the housings to be designed have a common set of design requirements. They must be water tight to protect the internal electronics from the environment. The structure must be sufficiently stiff so the total system stiffness is acceptable. The housings must conduct heat from the servo drivers contained within to the environment to be dissipated. Their internal electronics must be accessible and replaceable; permanent installation is unacceptable. The link solution must be compatible with existing joint module. Any design that does not meet all of these basic requirements will be deemed unacceptable.

The electronics housings have three varying design requirements across four types of housings. PXL uses three identical housings, and DXE uses six housings of three different configurations across two manipulators. The variable design require-

Table 5.1: Design constraints for RTSX links

Housing Location	Quantity	Servo Driver	Accessory	Low Power Accessories	Major Structural Loads
PXL	3	2x 60A	1x Brake Controller	—	Survive poor lift 6kN Load
DXE Shoulder	2	3x 60A	—	—	Survive poor lift 6kN Load
DXE Elbow	2	2x 20A	—	—	500 N-m bending
DXE Wrist	2	5x 20A	—	Wrist Camera Processor	175 N-m bending

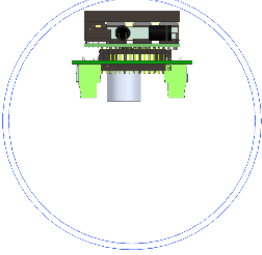
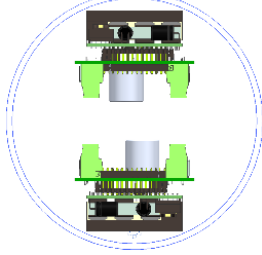
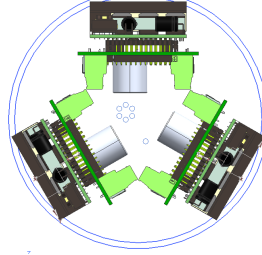
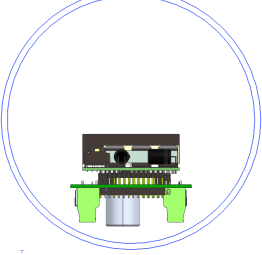
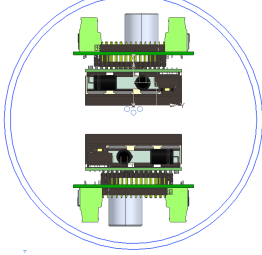
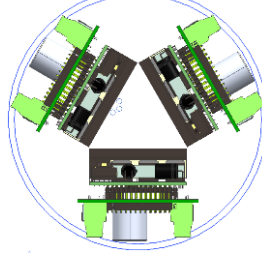
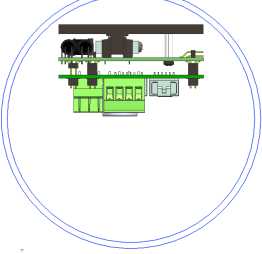
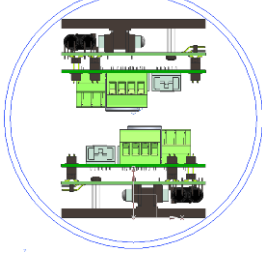
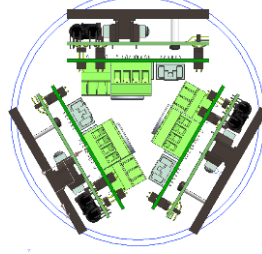
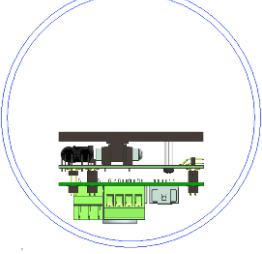
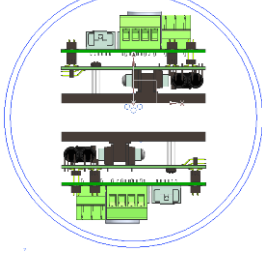
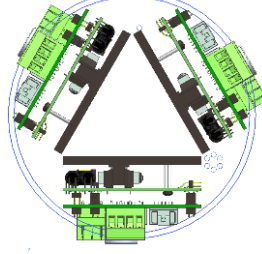
ments for each housing type and its location is listed in the table below. Finding commonality in these sets of design constraints will allow for a faster design process and a more affordable product.

These housings break down easily into three types by grouping how many high power units (HPUs) each housing will need to contain. A HPU is considered any component that consumes a large amount of power, such as motor controllers and brake drivers, which would require the high level of thermal dissipation this mounting scheme achieves. Two housings will need to contain five HPUs, five will house three HPUs, and two will house two HPUs. Further grouping of the housings can be achieved, but is dependent on packaging geometry for the HPUs. For that reason, the following packaging study was conducted to achieve maximum packing density of HPUs.

Multiple packaging configurations were considered for orienting HPUs inside of a housing. The geometry of DXE limits the cross sectional diameter to 5.375 inches. Two basic orientations of the servo driver were considered, as well as facing the heatsink inward or outward. Link cross sections were considered that packaged one,

two, or three HPUs. While it would have been advantageous to package three HPUs into one section, in no configuration did they fit within the cross section without modification. Several alternate designs were explored to package the HPUs, but it was found that wiring allowances prevented any form of the three unit cross section from working, even with modification to the HPU.

Table 5.2: Packaging cross sections considered for RTSX links

	One HPU	Two HPUs	Three HPUs
Orientation A			
Orientation B			
Orientation C			
Orientation D			

A test packaging was created to explore orientation D2 and B2, placing three servo drivers onto a central structure to be used for development on the shoulder of RTSX. The assembly was designed to use the same waterproof covering as the original housing, which constrained the exterior bounds of the packaging. This unit was fully assembled and implemented to observe any issues in packaging. It was immediately found that the limited clearance between controllers in configuration D2 proved difficult for wiring. It was also found that the geometry required to interface with the I-beam section was costly and required tighter tolerances than desired. Later versions of the D2 or B2 configuration forewent the use of I-beam stock, switching to a monolithic structure to eliminate as many tolerance stack-ups as possible.

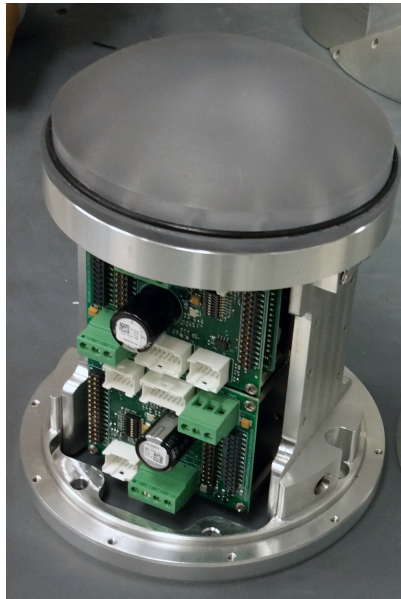


Figure 5.1: Packaging study of RTSX shoulder

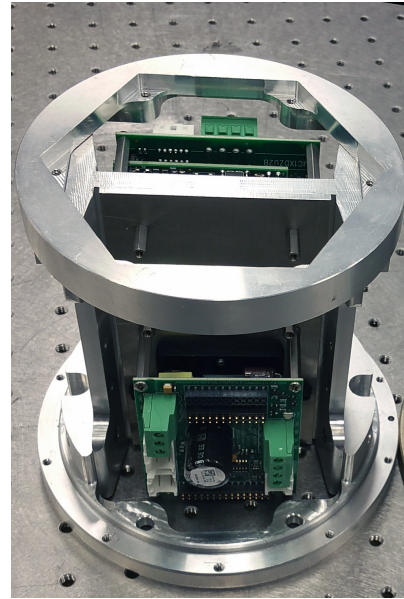


Figure 5.2: Obverse side of RTSX shoulder packaging study

This test packaging was an attempt at reusing the sheath made for the original design. While this did reduce cost, it imposed highly limited volume constraints.

This design approach was abandoned as it caused more problems than it solved. After this trial, the length and diameter of the link housing was treated as variable as well.

In its place a new format was created, using a modified form of layout 2A. The HPUs were oriented into a V configuration, so they could be mounted to an internal structure and wedged into the outer structure to conduct heat. This configuration required a 12% larger diameter than the original design to make allotments for wire paths and to fit the stock heat spreader packaged with the servo drives.

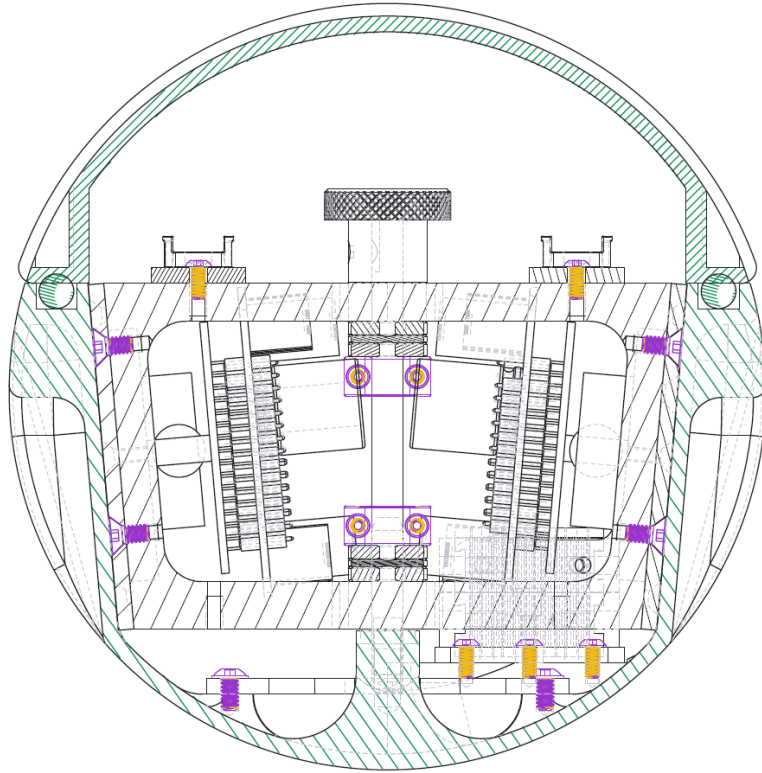


Figure 5.3: Cross section of prototype wrist housing

This prototype housing was a study in both packaging and maintainability. Arguably the most important component of this design was the inclusion of a lid, allowing the internals of the link to be accessed from the side. This side-access

concept has variety of benefits which are enumerated in chapter 8 and discussed throughout this paper. It provides a great benefit for reducing system maintenance and electronics development time by allowing direct access to the driving electronics. While the design pictured in Figure 5.3 was not selected for the final revision, many features and concepts from this design are used.

Chapter 6: Design Methods

As computer aided design software progresses, there is an increasing focus on the methodology used to design a product in the software. This design process used two different software packages, PTC Creo for the prototype links and Siemens NX 10 for the final design. Both software packages are capable of the top-down and bottom-up design methods discussed in this chapter. However, bottom-up design was practiced in PTC Creo and top-down was practiced in Siemens NX, largely due to operator experience.

6.1 Bottom-Up Design

This methodology was used for the packaging test unit in the shoulder and the prototype links. Bottom-up design is commonly used in assemblies with a low part count. In this method, all of the parts are designed individually and edited individually to interface with the final assembly. Only at the final assembly of all the components does the larger system exist. This is like designing a house by drawing the foundation, then the floor, the walls, and finally the roof. Overall, if the user has enough experience and design intuition, this method can be very quick, but will rarely produce optimal results.

6.2 Top-Down Design

A top-down design methodology was implemented for the final link design. This flow defines the geometry and features of all the components in an assembly from a top-level assembly file, sometimes referred to as a skeleton design. While seemingly more complicated than a bottom-up design process, top-down flow allows for faster system design studies and for quick spawning and destruction of components in the system. Top-down design also removes ambiguity by focusing on the interfaces and utility of each component, rather than the details of the component itself. Using the same house analogy, the entire house would be sketched roughly and refined multiple times and then used as a template to design individual parts of the house separately.

6.3 Part Tree Generation

Top-down design flow reduces total design time for large and complex designs, but does little to reduce the design time for individual components. To eliminate the time spent designing multiple similar components, such as fasteners or gaskets, a design tool known as family trees was used. A template part governed by a series of equations was created for each family of parts, and all parts in that family were generated from a parameter table.

This method can also be used for more complex components and was implemented for multiple major components in the link design. An example of this can be

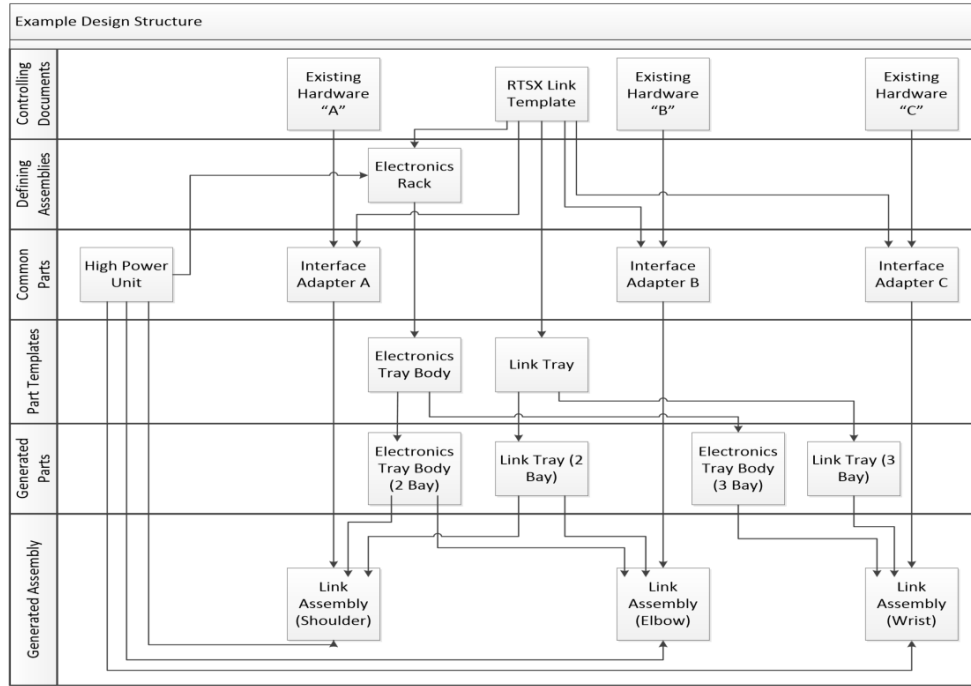


Figure 6.1: Example part tree structure

found in figure 6.1 in the generation of the electronics tray body and link tray. Two versions of each component were required, one supporting two HPU bays, and one supporting three HPU bays. Instead of designing two permutations of the same base design separately, a single template part was created. This template took in interface requirements from multiple sub-level components as well as exterior interfaces. From this template, both two- and three-bay versions of the link were generated automatically.

Generated parts were used extensively throughout the final link design. It was found that to use this method properly, extensive notes and mapping were required in order to understand the flow of design-driving constraints. Unfortunately, this design technique is somewhat obtuse to new users and takes an inordinate amount of time to train new designers on. It is suggested that future designs focus heavily

on documenting the flow of variables inside the generated parts tree. It is likely that a project of this scale is too small to benefit from this design method, however more iterations and refinement of documentation methods will be needed to fully understand this.

6.4 Design Methods Conclusions

The study of design methods within this process yielded useful results. The design of the prototype links, both the built up shoulder design and the monolithic tray designs, were constructed using the bottom up design method. These parts were designed quickly, taking approximately six months from conception to final design review. However, these parts had multiple fit-up issues as well as a large total system mass. The final design took approximately one year to complete but was able to achieve a far better performing design, as is detailed in the rest of this paper. The overall conclusion reached is that the balance between performance and design time should be weighed when selecting a design method.

Chapter 7: Second Design Revision Method

Using the lessons learned from the test packaging, the design was reconsidered abstractly. Ease of maintenance and speed of operations greatly outweigh the need for simplicity of design. Accepting harder-to-manufacture and -calculate designs allows for a system with higher utility. Tolerance stack-up is also detrimental to the system, making assembly difficult and reducing the positioning accuracy of the manipulator. Switching from a built-up primary structure to a monolithic design again increases cost and design complexity, but allows a more accurate product.

There are two major design concerns for operation and repair of RTSX, the length of the thermal path and disassembly procedures for maintenance. Thermal energy must be conducted from motor through the intermediate components in the manipulator, where it will be dissipated into the environment. Common materials used in space robotics have a thermal conductivity between 6.7 to 390 W/mK. Active heat pumping methods such as liquid cooling or refrigeration loops are to be avoided as the added complexity reduces the total system reliability. So when the thermal path between the heat load and the environment proves to be insufficient, the options for resolving the problem is limited to either switching to a higher thermal conductivity or reducing the characteristic length of the geometry.

Improving the disassembly procedures reduces the time for maintenance as well as development time. For the original design hierarchy, three major features limit the disassembly procedure. First, disassembly requires that all joints distal to the link must be removed before the link may be disassembled. This is problematic as each assembled joint segment is over 15kg, making them ungainly to maneuver precisely. Secondly, there is no method to disconnect the backplane from the joint actuators it controls. This can be seen in figure 2.6. earlier in this paper, where the backplane is soldered directly onto the harness. To replace the backplane due to a failed component, it must be painstakingly unsoldered, modified, and re-soldered to the harness. Third, the primary structure chain within the link must be broken to remove any electronics for maintenance. This is caused by the sheath which is used to seal the link internals from the environment. It resists hydrostatic pressures while allowing the card cage to transfer all the primary loads. While this design simplifies the flow of forces inside the link, it makes it impossible to access the internal electronics without breaking the primary structure chain.

To improve both of these design concerns, the following top level changes were made. Observe the differences in figure 7.1 and figure 7.2 . The flow between “Proximal Interface” and “Distal Interface” remains continuous, but the components between them are manipulated. Also note the change in the “Remove for Maintenance” region and how this will affect disassembly procedures. As is discussed later in this chapter, extracting the distal interface from the maintenance region has great benefit for the maintainability of the system.

Leaving the primary structure path unbroken during maintenance is the first

concern. The sleeve was eliminated in favor of a non-structural side access door with a face seal, so the internals of the link can be accessed while leaving the link structure intact.

In addition to making the electronics easier to access, a modification was made to ease the bulk of operational issues. An external, water tight connector was added to the lid, giving the operators a direct connection to all of the debugging ports onboard the electronics, the communication bus, and the power buses. While the connector will not resolve all of the difficulties in trouble shooting the internal electronics, it makes the majority of modifications easier.

An electrical disconnect was added between the joint actuators and their controlling electronics, eliminating the need to solder the wiring harness for any regular maintenance. The servo drivers were packaged into a removable electronic bay along with all other electronic components inside the link. All of the electronics inside the link may now be exchanged by disconnecting the tray connector and removing the entire rack.

The thermal path from the servo driver to the environment was simplified in the new methodology. Instead of flowing through multiple components to heat sink to the ambient environment due to the poor thermal characteristics of the waterproofing sleeve, heat is conducted directly through the sidewall of the tray and into the environment. This change removes three thermal interfaces and shrinks the characteristic length from several inches to a fraction of an inch. All of these modifications will lead to a greatly improved thermal profile.

Top level modifications to the design were not conducted in isolation from the

detail design. What figure 7.2 shows is the result of multiple design iterations and design space explorations.

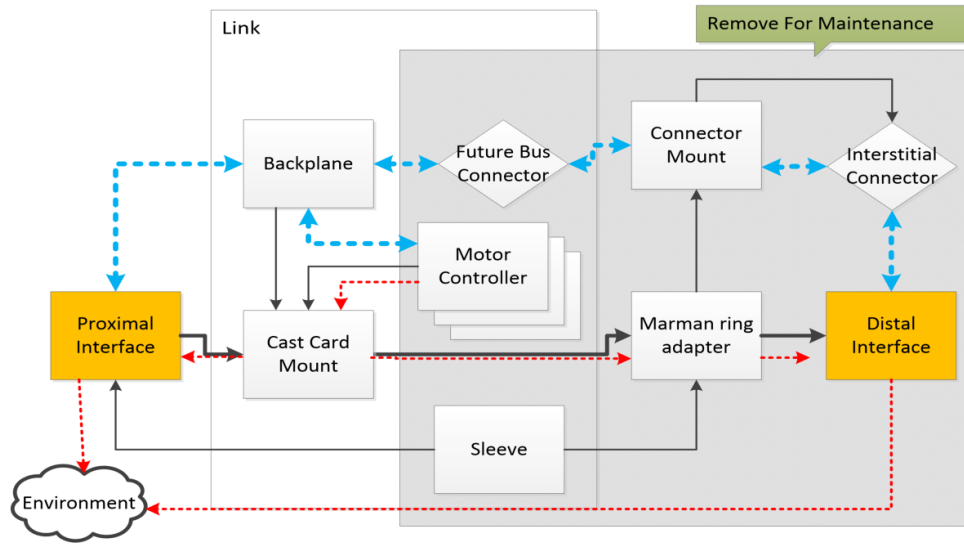


Figure 7.1: Original Design Hierarchy

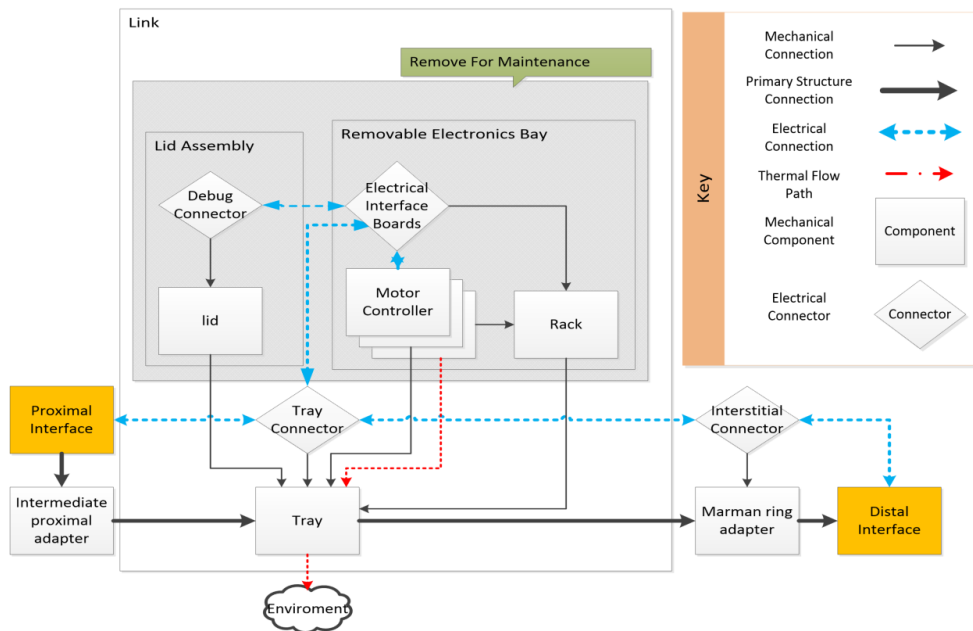


Figure 7.2: Redesigned Hierarchy

Chapter 8: Structural Analysis

A concern for primary structure components in a robotic arm is stiffness. The stiffness of a serial manipulator directly impacts its harmonic frequency and positioning accuracy. With a decrease in either, the load carrying capacity and operating speed must be decreased for stable operation. For most serial revolute robotic systems, the bulk of the tool tip flexure is due to the spring rate of the gearboxes, but this is not necessarily true if the drive electronics are packaged into the interstitial links. The packaging and accessibility requirements inherent in placing drive electronics inside serial robotic links may cause a reduction in flexure stiffness that must be accounted for in determining total system stiffness.

8.1 Analysis Assumptions

Serial link manipulators have a structure with a large length to width ratio, which allows for some simplifications in the following analysis. RTSX is accurately modeled using Euler-Bernoulli beam theory, as the dominant forces on the link body are bending moments. The individual link segments of RTSX have a relatively low length to width ratio but are integral into a longer system, so the deflection of interest will be angular displacement, not linear. Note that this is the same

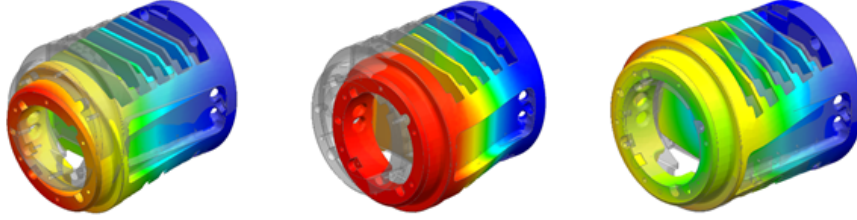


Figure 8.1: Bending in XX, YY, and ZZ respectively

flexure metric by which the revolute joints are analyzed. By these assumptions, the flexibility of RTSX will be modeled as a series of torsional springs spaced at geometric nodes across the length of the arm.

8.2 Gearbox Stiffness

As stated before, torsional stiffness of revolute joints has the greatest influence on tool tip stiffness for the majority of serial link manipulators. For comparison, the following are the performance characteristics of the gearboxes used in RTSX. As stiffness is a critical factor in gearbox selection, two types of gearing systems dominate the robotics market: strain wave and hypocycloidal (colloquially known as cycloidal drive). Both have high gear ratios with good torque to mass ratios, are compact, and have theoretically zero backlash. Strain wave gearboxes have two distinct programmatic advantages over hypocycloidal: they have been used in space flight since 1971, and they are readily available on the market. Given these criteria, RTSX was constructed with strain wave gearboxes manufactured by Harmonic Drive.

Harmonic Drive gearboxes have a non-linear torque response. In the region of torque that RTSX operates in, the response can be approximated as linear. The

torsional stiffness of the gearbox models used is approximately 67 kNm/rad and yields an approximate first mode harmonic frequency of 4.0Hz.

8.3 Analysis of Original System

To calculate the torsional stiffness of the RTSX links, a finite element model was created and analyzed using NASTRAN SOL 101. For the maximal loading conditions, their response was found to be roughly linear and their spring constants are listed in table 8.3. For comparison, an ideal link was formulated using the same volume of aluminum, length, and diameter, to show what the ideal performance would be for a link without internal electronics. While bending can occur across a number of axes, the chosen alignment gives the minimum and maximum bending stiffness for the body. For the system wide analysis, the bending axis of lowest stiffness will be used. As seen below, stiffness is reduced when using non-optimal link geometry by an order of magnitude. Thus, the assumption that the link stiffness has little influence on system harmonic frequency and stiffness is no longer true.

Table 8.1: Stiffness stackup of the original and ideal links for RTSX

Axis of Torsion	Ideal Link Stiffness Limit kNm/rad	Original Link Stiffness kNm/rad	Gearbox Stiffness kNm/rad	Ideal Joint/Link Combined Stiffness kNm/rad	Original Joint/Link Combined Stiffness kNm/rad
Bending (XX)	6066	50.7	67	66	59
Bending (YY)	6066	3437	67	66	65
Torsion (ZZ)	13714	181.3	67	67	49

8.4 Prototype Link Layout

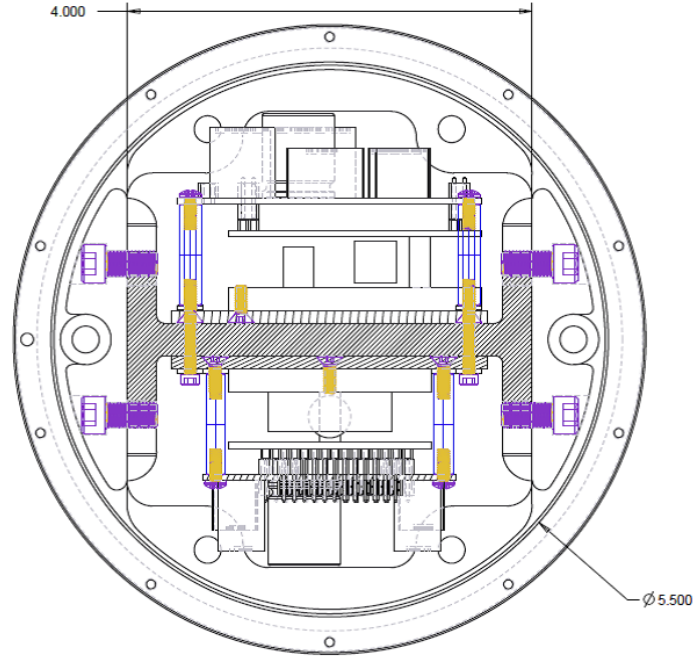


Figure 8.2: Cross section of prototype shoulder housing

After exploration of the design space, a prototype shoulder module was constructed with the goal of minimizing cost. As mentioned in figure 5.2, the shoulder module was constructed using the B2 and D2 cross section design, which necessitates an endoskeleton type structure. To reduce cost, the system was sized to use an American Standard I beam as stock. Assembly tolerances prevent any welding along the structure, so all components in the primary structure chain must be bolted together. This results in more components in the assembly and requires more precise machining tolerances to reduce error stack-up.

This design was quickly abandoned for future links because of assembly difficulties, torsional stability, and the quantity of components. The next housing design



Figure 8.3: Side-by-side comparison of original and prototype wrist housings

to be produced was constructed in an attempt to greatly reduce the number of critical mechanical components. Instead of bolting together fittings to the primary structure, both ends of the link were limited to using the original marman band fasteners only. The challenge exists in trying to find a common bolting design that can be adapted to fit each of the multiple interfaces on the RTSX platform, as well as survive all of the forces that the arm is subjected to.

8.5 Prototype Analysis

One redesign goal for RTSX was to make the electronics more accessible to reduce maintenance time. After several design iterations considering tradeoffs between structure, machinability, and operation, a side-loading design with a removable lid was selected. To assess the usefulness of such a design, a prototype was constructed and implemented on RTSX. This design concept was found to be effective, but it came with several disadvantages. Most importantly to this analysis, the side-loading housing created an open cross section, which proved to be unacceptably flexible.

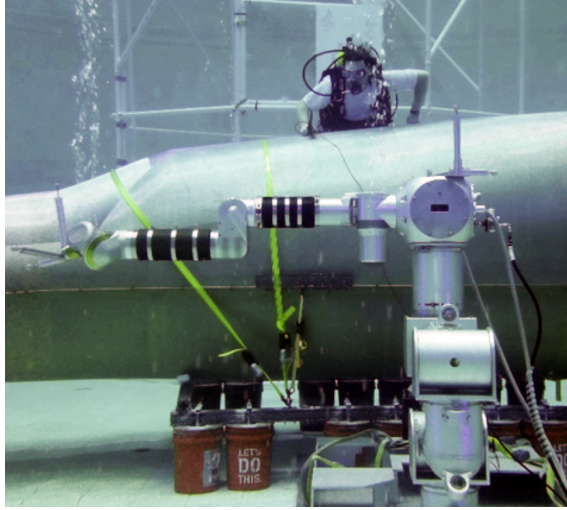


Figure 8.4: RTSX prototype link flexibility being tested using a visual tracking system.

Table 8.2: Comparison of torsional stiffness between link designs

	Original Link Stiffness	Prototype Side-Access Link Stiffness	Final Side-Access Link Stiffness
Worst Case Bending kNm/rad	507	161	584
Torsion kNm/rad	181	127	345
Average Link mass kg	8.6	8.0	4.3

The prototype side-loading design greatly decreased servicing time for RTSX, but its open cross section did not meet the required stiffness in bending or torsion. Flexibility tests were conducted in neutral buoyancy 8.4, evaluating the tool tip deflection throughout a variety of poses and tip forces. Tip deflection was measured using a multi-camera motion capture system. Over the range of forces RTSX was designed to output, tip deflection was found to be as much as 11mm, which is out of acceptable bounds for many of the intended operations. To improve performance to acceptable levels and still use the side-loading design, the lid must be integrated to the link structurally to close the cross section.

While there are several structural disadvantages to using a side loading link



Figure 8.5: Final link design for RTSX

configuration, it is possible to mitigate these through analysis and design. By loading the electronics into the side of a structural link, the cross section must be split to allow for access. This is problematic as the torsional stiffness of the link is greatly reduced and the shear center is moved outside of the link body. Unless the link body is sufficiently built up, which would be very massive, a lid must be firmly bolted to the link body to close its cross section. While we have found it possible to operate the robotic system without closing the links, the tool tip stiffness is noticeably reduced. Machinability is easier as the geometry of the link is restricted to the outside perimeter, but machine time is increased to support lightening features such as isogrids. Accepting these requirements, allowing link-integral electronics to be accessed through the side of the link reduces maintenance time from days to hours.

The side-loading housing was updated to use a series of shear bolts to pin the lid of the housing to the body of the link. This design change reduced the flexibility of the link to acceptable ranges. Due to packaging constraints, it was not possible

to bolt continuously along the length of the lid. Some flexure and slippage occurs in the interstitial space between the bolts, but the increase in stiffness was found to be acceptable. Lightening features were also added to the link body to increase the allowed tip mass of RTSX, reducing the total assembled mass of the link by 30%. A geometric optimization was also performed on the link design to determine its isogrid geometry while still maintaining adequate stiffness.

8.6 Conclusions

Integrating electronics into the link of a robotic arm is a non-trivial design process. While there are several advantages to doing this for the electrical system and general operations, it invalidates the standard assumption that the tool tip spring rate is calculated using only the stiffness of the gearboxes. The structural design process now relies on finite element methods to evaluate the link stiffness instead of simple Euler-Bernoulli beam theory due to the non-symmetric and irregular geometry inherent in electronics packaging. Given the benefits to electrical systems and operations, packaging the drive electronics in a side-loading link design was found to be preferable to the original design.

Implementing non-symmetric link cross sections requires a higher level of modeling than the simplistic results found in table 8.2. To fully quantify the geometric feature impact on performance of the asymmetric link, we must form a characterization matrix for the response of the link to external loads. The following chapters are a detailed expansion of this analysis.

Chapter 9: Structural Inclusion of the Lid

A preliminary design analysis shows that even if the entire structural volume allowed for the tray, pictured in Figure 8.3, were occupied with titanium, the tray would still be too torsionally flexible to produce an acceptable design. To increase the stiffness of the link in the designated design volume, it is necessary to either reinforce the tray using stiffer materials such as carbon composites, or to use the lid as a structural component.

9.1 Structural Connection Attempt

The prototype design assumed no structural connection between the lid and the tray, as they were secured together with marman bands. The bands were designed to impart only enough force to compress the perimeter face seal between the lid and the tray. If the lid is to contribute to the torsional stiffness of the link, it needs to transmit shear forces between the lid and the tray.

An attempt was made to provide a high normal force between the lid and the tray and transmit the forces via friction between the tray and the lid. The design selected used two tension members running through the diameter of the assembled link. They can be seen at either end of the link shown in figure 9.2. These members

were tensioned by a set of Belleville springs to provide a high, but known tensile force. The springs were compressed by a 7/16 double height hex fitting, seen in figure 9.1, and locked into place by a spring loaded retaining fixture to prevent unintentional actuation.

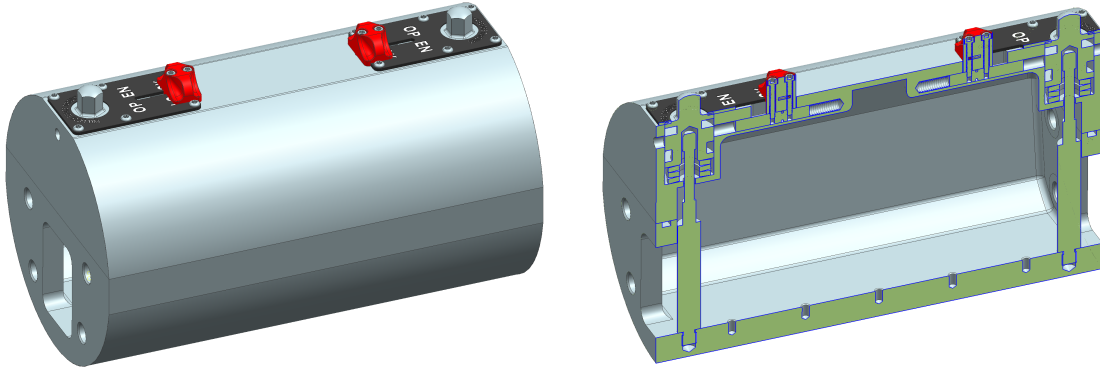


Figure 9.1: External lid of an alternate lid design Figure 9.2: Cross section view of an alternate lid design

While this design is simple for an operator to actuate, the tensile members were not able to produce adequate surface friction between the lid and the tray. This design was simulated using a linear static FEA with surface contact and friction between the lid and the tray. The lid was not capable of distributing the normal pressure across a wide enough surface to be effective, resulting in concentrated areas of shear transmission only at the ends of the lid. Limits on the structural geometry of the link prevented a sufficiently rigid design of the lid. A design had to be devised to transmit shear across the length of the lid/tray connection, preferably by means of a mechanical joint rather than frictional connection. After some design exploration, it was found that shear bolts placed along the perimeter of the lid could be sufficient.

9.2 Bolted Lid Analysis

To alter the stiffness of the side-loading link design, a lid must be bolted to the open face of the link to close its cross section. While forces on the bolts spaced at regular intervals and placed on an infinite beam can be simply calculated, understanding their interaction with the stiffness of the system is not as clear. A set of system level loads were established and used to generate table 9.1. The following analysis shows the numerical methods used to characterize the forces that the lid bolts will be subjected to. These methods were then used for fastener selection and placement, documenting the motivation behind the bolts selected.

Table 9.1: Loading values for RTSX 2 bay link design

Symbol	Value [units]	Description
V	1000 N	Shear force imparted to the link
T	240 N-m	Axial torque imparted to the link
R	0.068 m	Radius of the link cross section
M	440 N-m	Bending moment imparted to the link
L	0.2286m	Effective length of the link
P	41000 Pa	Internal differential pressure in the link

9.3 Calculating Bolt Forces

By bolting along the edge of the link housing, shear forces can be transmitted between the link body and the lid. To simplify analysis, the link body was calculated as a tube of constant wall thickness, bisected along its axis. The region of this bisection is of interest. The goal of the analysis was to determine the forces to be reacted by N number of bolts placed along the bisected edge to effectively “glue”

the sides of the tube back together. This calculation is done using the following parameters.

For a hollow shaft under axial torque and small deflections equation 9.3 relates geometry and torque to shear force.

$$\tau_{torque} = \frac{T}{2\pi tr^2} \quad (9.1)$$

Pressure forces are also a significant contributor to the forces on the bolts. These forces are calculated by observing the hoop stress generated for the cross section of the link, detailed in equation 9.3. As we are not concerned with the hoop stress across the link/lid system, merely the stress along their 1D interface, the thin walled assumption can be used to simplify calculation. This yields the following.

$$F_h = \frac{PrL}{2} \quad (9.2)$$

Bending of the beam will also impart a shear stress across the bolt head. This load is approximated by the resultant force from the moment as reacted through the centroids of each shell half, shown in equation 9.3.

$$F_{bending} = \frac{M\pi}{4r} \quad (9.3)$$

For calculating the shear force involved in the transverse shear loading of the link section, equation 9.3 was used.

These forces generate a tensile, shear, and moment force on the bolt. To implement this design without failure, the following relations must be true:

$$F_{shear} = \frac{VL}{2\pi r} \quad (9.4)$$

1. The sum of all forces on the bolt must result in a Von-Mises stress lower than the yield stress of the bolt.
2. The clamping force across the effective seam length of the bolt must be high enough to overcome the moment generated along the seam. This prevents the bolt shank from bending and breaking.
3. The preload force must be greater than the sum of all tensile forces required of the bolt.

From these relations the following loads on each bolt can be estimated. They are calculated on the surface of the thin walled cylinder at the seam. The sum of shearing forces are denoted in equation 9.3 and the sum of compressive stresses are in equation 9.3, totaling into equation 9.3

$$\tau_x = \left[\frac{T}{2\pi r^2} + \frac{M\pi}{4rL} + \frac{V}{2\pi r} \right] \frac{L}{NA_{bolt}} \quad (9.5)$$

$$\sigma_y = \left[\frac{Pr}{2} + \frac{1}{2} \frac{T}{2\pi r^2} \right] \frac{L}{NA_{bolt}} R_{PL} \quad (9.6)$$

Given the known values, and with a preload ratio (R_{pl}) of 2, the previous equations simplify to equation 9.3.

After some examination of this design space, it was found that a likely solution was by using between 2 and 5 bolts per side, using either 10-32, 1/4-28, or 5/16-32 bolts.

$$\sigma_{von} = \sqrt{\sigma_y^2 + 3\tau_x^2} \quad (9.7)$$

$$\sigma_{von} = \frac{33100}{NA_{bolt}} \quad (9.8)$$

Packaging requirements made using four or more bolts difficult, as it impinged on the packaging cross sectional area for the servo drivers. Finite element models revealed that using less than three bolts per side caused the lid to lift free of the gasket under certain loading conditions, leaving only the option of using three bolts per side. For this application, high strength National Aerospace Standard (NAS) or Military Standard (MS) bolts should be used, the yield strength of which is approximately 1.1 GPa (160 Ksi), to reduce or eliminate the probability of fatigue-based failure.

Another loading scenario must be considered. If the bolts are not preloaded at all, they are subjected to a bending moment. This moment is equivalent to bending the bolt shank with the sum of all shear loads at a distance of the lid thickness, in this case 0.2 inches. Observing the yielding safety factor using a 1.1 GPa bolt, the following holds true.

Operating RTSX with untightened bolts due to human error is possible. In order to not yield the lid bolts in this case, bolt size 10-32 should not be used. While the higher safety factor of 5/16-32 bolts is appealing, it makes packaging more difficult and would add 5% to the length of the housing. Given these factors, a 1/4-28 bolt size was selected for mating the lid to the link body.

Table 9.2: Stress caluclated per bolt in selected configurations

	Von-Mises stress in bolt [MPa]			
Bolt Size	2 bolts per side	3 bolts per side	4 bolts per side	5 bolts per side
10-32	807	538	403	323
1/4-28	437	291	218	175
5/16-32	272	181	136	108

Table 9.3: Safety factor for bolts considered

Bolt Size	Nominal Safety Factor	Untightened Safety Factor
10-32	2.0	0.6
1/4-28	3.8	1.6
5/16-32	6.1	3.1

9.4 Determining Parent Material Geometry

With bolt geometry selected, the geometry and properties of the parent material must be selected to ensure proper operation. The goal of this design is to minimize geometry volume without compromising the maximum bolt load. An experiment was conducted to examine the minimum volume of material required about a threaded surface in the parent material. Details about this experiment can be found in [Appendix C](#).

The results of this study were used to create keep out boundaries for subtractive features that could intersect threaded features. These boundaries are modeled as tapered cylinders with the base of the cylinder starting at the face of the threaded surface. This was very useful for the design process and provided a better sense of what subtractive features would be allowed. The final geometry was selected as to not intersect with the keep out boundaries at all, so the tapered cylinder surface is not visible. This method may be of more utility in other designs were a subtractive feature must intersect a threaded surface.

Chapter 10: Stiffness Analysis of Non-Axisymmetric Beams

This section details mathematical and analytical methods for characterizing the structure of the link. Typically, the link stiffness would conform to the structure in equation 10. This matrix is created as a characteristic equation of a link section assuming it is analogous to an Euler-Bernoulli beam. When the center of shear of a beam is coincident with the centroid and neutral bending axis, there is limited coupling between shear and moment forces in a beam. Figure ?? illustrates the minimum characteristic matrix for a cantilevered beam. However, once the center of shear begins to deviate from the centroid, cross coupling becomes rampant.

$$\begin{bmatrix} \frac{L^3}{3EI_{xx}} & 0 & 0 & 0 & \frac{L^2}{2EI_{xx}} & 0 \\ 0 & \frac{L^3}{3EI_{yy}} & 0 & \frac{-L^2}{2EI_{yy}} & 0 & 0 \\ 0 & 0 & \frac{L}{EA_{zz}} & 0 & 0 & 0 \\ 0 & \frac{-L^2}{2EI_{yy}} & 0 & \frac{L}{EI_{yy}} & 0 & 0 \\ \frac{L^2}{2EI_{xx}} & 0 & 0 & 0 & \frac{L}{EI_{xx}} & 0 \\ 0 & 0 & 0 & 0 & 0 & \frac{L}{GJ_{zz}} \end{bmatrix} \begin{bmatrix} V \\ M \end{bmatrix} = \begin{bmatrix} \delta \\ \phi \end{bmatrix} \quad (10.1)$$

When an eccentricity exists between the shear center and the center of bending, the effective bending stiffness is reduced and axial torsion is coupled with beam deflection. This interferes with the system in two ways: decreasing the stiffness and causing out-of-plane responses to forces. The results of such an eccentric distance ε in the X and Y axis can be found in equation 10.1.

$$\begin{bmatrix} \frac{L^3}{3EI_{xx}} & 0 & \frac{-\varepsilon_x L^2}{2EI_{xx}} & 0 & \frac{L^2}{2EI_{xx}} & \frac{-\varepsilon_y L}{2GJ_{zz}} \\ 0 & \frac{L^3}{3EI_{yy}} & \frac{-\varepsilon_y L^2}{2EI_{yy}} & \frac{-L^2}{2EI_{yy}} & 0 & \frac{\varepsilon_x L}{2GJ_{zz}} \\ 0 & 0 & \frac{L}{EA_{zz}} & 0 & 0 & 0 \\ 0 & \frac{-L^2}{2EI_{yy}} & \frac{\varepsilon_y L^2}{2EI_{yy}} & \frac{L}{EI_{yy}} & 0 & 0 \\ \frac{L^2}{2EI_{xx}} & 0 & \frac{-\varepsilon_x L^2}{2EI_{xx}} & 0 & \frac{L}{EI_{xx}} & 0 \\ \frac{-\varepsilon_y L}{2GJ_{zz}} & \frac{\varepsilon_x L}{2GJ_{zz}} & 0 & 0 & 0 & \frac{L}{GJ_{zz}} \end{bmatrix} \begin{bmatrix} V \\ M \end{bmatrix} = \begin{bmatrix} \delta \\ \phi \end{bmatrix}$$

Figure 10.1: Extended characteristic equation for a link accounting for eccentricity of the center of shear

It should be noted that the coordinate frame for this transformation is not typical for Euler-Bernoulli beam bending. As this design will be applied to robotics, a different frame was selected. Denavit-Hartenberg parameters, a common coordinate frame convention for robotics, aligns the Z axis along the axis of rotation for the previous joint.

10.1 Verification of Model

This modeling method of deriving offsets and gross geometry properties from experimental finite element analysis was tested using a simplified model. The test beam was a 25.4mm diameter, 305mm long cylinder with a Youngs modulus of 68.9 GPa. The orthogonal test forces were applied individually to solve for each column of the matrix, using a tip force of 90 N and a tip moment of 2.26 N-m. Two more test cases were run, using a -25.4mm eccentricity in the x and then y axis. Solving for the magnitude of error between the predicted matrix and FEA matrix, the following error range was found, averaging across all solutions.

Very little deviation exists between a finite element model and the Euler-Bernoulli model except in C_{16} and C_{26} . There is almost no correlation between

Table 10.1: Percential error between the extended model in the compliance matrix modeled in equation 10.1

	C_{x1}	C_{x2}	C_{x3}	C_{x4}	C_{x5}	C_{x6}
C_{1y}	1.92%	0%	0.783%	0%	2.38%	100%
C_{2y}	0%	1.92%	0.783%	2.37%	0%	100%
C_{3y}	0%	0%	0.569%	0%	0%	0%
C_{4y}	0%	0.562%	0.011%	0.059%	0%	0%
C_{5y}	0.562%	0%	0.011%	0%	0.059%	0%
C_{6y}	0.766%	0.766%	0%	0%	0%	2.27%

these values in the model and the results from the finite model simulation, showing a breakdown in the simplified model. Fortunately, these values are relatively small and have little influence on the overall performance of the link. Considering these error ranges to be reasonable without refining the finite element mesh, the same methods were applied to the original, prototype, and final upper arm link.

Deviation of a link design from a predictable Euler-Bernoulli model can be considered detrimental to the control and operation of a robotic manipulator. Very simple control models do not account for the flexure of components in the system. More complex models predict and compensate for the flexure of components, but only in simple terms to reduce controller complexity. It is expected that deflection will be in plane with the deforming forces. Deviating from a simply predictable Euler-Bernoulli model causes deflections to deviate out of the plane of the deforming forces. While this will occur in axisymmetric cases due to out-of-plane warping, limiting this deformation to an insignificant level is important. The resulting compliance matrix of the original housing is shown in equation 10.1

The dominating region in the compliance matrix in equation ?? is C_{44} C_{55} C_{66} , equating applied moments directly to angular deflection about the same axis.

$$\begin{bmatrix} 28.6 & 0.3 & 0.5 & -1.1 & 337.2 & 40.8 \\ 0.2 & 199.9 & 0.4 & -110.4 & 8.5 & -33.6 \\ 0.4 & 0.4 & 2.6 & -2.7 & 6.9 & -1.8 \\ -0.9 & -98.1 & -2.0 & 772.3 & -35.9 & 35.6 \\ 313.9 & 7.8 & 7.8 & -35.7 & 3861.3 & -42.4 \\ 39.2 & -39.2 & -1.8 & 18.9 & -24.1 & 5405.9 \end{bmatrix} = C_{original} \times 10^9 \quad (10.2)$$

As mentioned before, due to the geometry of a long serial-link manipulator, angular deflections in manipulator components dominate the stiffness of the tool tip. While the largest component is C_{66} , this deflection only affects tip stiffness in off-axis poses where a significant torque can be applied to the link body.

$$\begin{bmatrix} 85.7 & -0.1 & 11.4 & -0.7 & 449.6 & -0.7 \\ -0.1 & 228.4 & 0.0 & -112.4 & 1.9 & 1123.9 \\ -11.4 & 0.0 & 5.7 & -0.1 & -86.4 & -0.2 \\ -0.7 & -137.3 & -0.1 & 772.3 & -5.8 & 55.6 \\ 412.0 & 1.4 & 78.5 & -6.4 & 3089.1 & 1.9 \\ -0.6 & 1569.5 & -0.3 & 49.7 & 7.2 & 14673.1 \end{bmatrix} = C_{prototype} \times 10^9 \quad (10.3)$$

A large amount of coupling can be observed in C_{62} and C_{26} of equation 10.1. This is attributed to the open cross section of the prototype link, which places the center of shear away from the neutral bending axis. It should also be noted that the magnitude of C_{66} is much greater in the prototype housing, denoting that is more compliant. This too is due to the open cross section of the link tray. Note that the magnitude of C_{44} and C_{55} are nearly comparable between the original and prototype housing, which follows as one was used as the design basis for the other.

The final housing compliance matrix, shown in figure 10.2 shows an overall stiffer link. Coupling has been greatly limited from previous designs. To fully understand how this improvement impacts the performance of RTSX, an evaluation

$$\begin{bmatrix} 85.7 & 0 & -8.6 & 0.2 & 337.2 & -0.2 \\ 0 & 28.6 & 0 & -112.4 & -0.3 & 56.5 \\ -8.6 & 0 & 5.7 & 0 & -70.4 & 0 \\ 0.2 & -117.7 & 0 & 772.3 & 1.7 & 31.9 \\ 333.5 & -0.2 & -78.5 & 1.5 & 3089.1 & 1.8 \\ -0.4 & 58.9 & 0.0 & 33.7 & 1.2 & 2316.8 \end{bmatrix} = C_{final} \times 10^9$$

Figure 10.2: Characteristic compliance matrix of the final housing, shown in N, m, N-m, and radians

method was constructed to compare how the link designs flex, not just their overall magnitude.

10.2 Evaluation of Characterization Data

To demonstrate the impact of coupling terms on the tool tip stiffness, we can examine a simplified scenario in Cartesian space. Say the link is the most proximal component of a serial-link manipulator with a tool tip located at [1,1,1]m. A linear force is applied to the tool tip and the resulting forces on the link are [1,1,1,1,1,1]. Using these components as generic inputs, the impact of each value in the compliance matrix can be calculated. This result will be referred to as the Impact Percentile Matrix (IPM).

An ideal distribution for the IPM was created using the ideal link geometry described in section 18. Note that in an ideal IPM $P_{44}=P_{55}=P_{66}$, $P_{15}=P_{24}=P_{42}=P_{51}$, $P_{11}=P_{22}$ and all other values have little impact on the deflection of the tool tip. This observation again confirms the starting simplification of this design process, that angular deflection of the link due to applied moments has the largest impact on tool tip stiffness.

$$\begin{bmatrix} \mathbf{6.58} & 0 & 0 & 0 & \mathbf{2.58} & 0 \\ 0 & \mathbf{6.58} & 0 & \mathbf{2.58} & 0.01 & 0.01 \\ 0 & 0 & 0.06 & 0 & 0.01 & 0 \\ 0 & \mathbf{2.58} & 0 & \mathbf{25.42} & 0.03 & 0 \\ \mathbf{2.58} & 0.01 & 0 & 0.03 & \mathbf{25.42} & 0 \\ 0 & 0.01 & 0 & 0.04 & 0.04 & \mathbf{25.42} \end{bmatrix}$$

Figure 10.3: Ideal IPM distribution

$$\begin{bmatrix} 0.25 & 0 & 0 & 0.01 & \mathbf{2.93} & 0.35 \\ 0 & \mathbf{1.74} & 0 & \mathbf{0.96} & 0.07 & 0.29 \\ 0 & 0 & 0.02 & 0.02 & 0.06 & 0.02 \\ 0.01 & \mathbf{0.85} & 0.02 & \mathbf{6.70} & 0.31 & 0.31 \\ \mathbf{2.73} & 0.07 & 0.07 & 0.31 & \mathbf{33.52} & 0.37 \\ 0.34 & 0.34 & 0.02 & 0.16 & 0.21 & \mathbf{46.93} \end{bmatrix}$$

Figure 10.4: Original link IPM distribution

$$\begin{bmatrix} 0.37 & 0 & 0.05 & 0 & \mathbf{1.96} & 0 \\ 0 & \mathbf{0.99} & 0 & 0.49 & 0.01 & \mathbf{4.89} \\ 0.05 & 0 & 0.02 & 0 & 0.38 & 0 \\ 0 & 0.60 & 0 & \mathbf{3.36} & 0.03 & 0.24 \\ \mathbf{1.79} & 0.01 & 0.34 & 0.03 & \mathbf{13.44} & 0.01 \\ 0 & \mathbf{6.83} & 0 & 0.22 & 0.03 & \mathbf{63.85} \end{bmatrix}$$

Figure 10.5: Prototype link IPM distribution

$$\begin{bmatrix} \mathbf{1.13} & 0 & 0.11 & 0 & \mathbf{4.46} & 0 \\ 0 & 0.38 & 0 & \mathbf{1.49} & 0 & 0.75 \\ 0.11 & 0 & 0.08 & 0 & \mathbf{0.93} & 0 \\ 0 & \mathbf{1.56} & 0 & \mathbf{10.22} & 0.02 & 0.42 \\ \mathbf{4.42} & 0 & \mathbf{1.04} & 0.02 & \mathbf{40.90} & 0.02 \\ 0.01 & 0.78 & 0 & 0.45 & 0.02 & \mathbf{30.67} \end{bmatrix}$$

Figure 10.6: Final link IPM distribution

The out of plane deformations observed in the finite element results are due to warping and the location of the shear center. A cross sectional center of shear that is not coincident with the neutral axis of bending of the beam will result in torsion of the beam in addition to Euler-Bernoulli based deflection. This out-of-plane deflection is problematic as the tool-tip deflection is no longer in line with the applied forces.

Unequal contribution of C_{44} C_{55} C_{66} to the tool tip stiffness will result in a higher influence of manipulator pose on the stiffness. To simplify the control scheme of the manipulator, it is desirable to have equal contributions from all three components. A comparison between the original, prototype, and final redesign link is shown in figure 10.7. Note that the magnitudes of C_{44} C_{55} C_{66} deviate more than the original design in the prototype, and less than the original design in the final version. This shows a significant improvement in performance between the

prototype and final design.

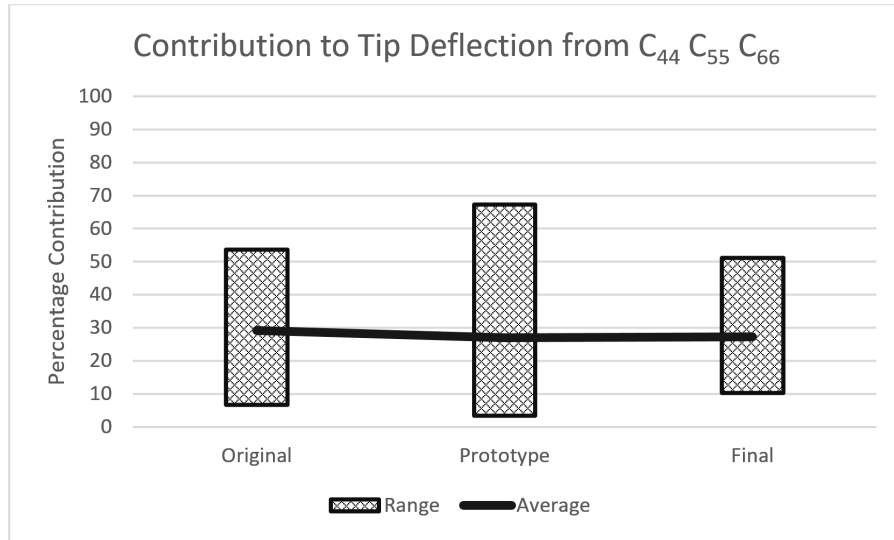


Figure 10.7: Spread of tip deflection contribution

10.3 Influence of Tool Tip Stiffness

Tool tip stiffness is one of the driving design characteristics of a robotic manipulator. In terms of positioning error; the stiffer the tool tip, the lower the force deflection, the more accurate positioning becomes. Compliance control uses a force-torque sensor at the tool tip to observe the tool force and to allow the manipulator to be compliant in desirable ways. Ideally, this would be conducted with a manipulator of infinite stiffness, but this is unfortunately impossible.

When performing a task that requires an accurate tip force, such as making an incision in surgery or laying carbon fiber on a form, the manner in which the tip deflects can affect the performance. If the tip deflection is not symmetric to the tip force, unintended motion will result. As an example, let's consider a 6 degree of freedom manipulator with an asymmetric tip stiffness that is being programed

to cut out a pattern with a knife. A simple method would be to make a trajectory across the surface with the tool tip and apply a specific force normal to the cutting surface. As the blade edge presses in, it will react with a force normal to the surface, but lateral forces will also be generated due to the asymmetry. The robot may be able to trace a perfectly straight line across the face of the surface, but when trying to cut using the same trajectory the line will warp.

Predictability of motion is extremely important for any robotic task. If a robot tasked with surgery or welding cannot keep a straight line, it is of little use for automation beyond coarse positioning. While it is possible to leave the task of correcting this malfunction to the controls engineers, by using the analysis and design techniques in this paper, it can be corrected in the mechanical design instead.

10.4 Conclusions

Based on the metrics created and evaluated in this chapter, the final structural design of the link is empirically better. The final link design is more rigid in all bending axes, but more importantly it is more uniform in its deflection. Eccentric Euler-Bernoulli type beam loading is limited with the final design by reducing the eccentricity of the shear center, compared to the prototype link. In making the link design similar to an ideal beam, dominated by the torsional deflection components C_{44} , C_{55} , and C_{66} , the link will deflect in a more predictable manner when implemented in a long serial-link manipulator.

10.5 Potential for Future Work

This method of analysis has shown that eccentricity between the center line of shear and the load axis causes a moment about the center of shear, resulting in a torque applied to the link. In robotic manipulator design the joints are frequently offset from one another, either to increase the range of motion, or for stowing the manipulator. A serial link robotic manipulator can be designed with asymmetric links such that the position of the center line of shear intersects the joint, and virtually eliminates the structural offset. This would allow the use of massively asymmetric link structures and would increase the tip stiffness of the manipulator. However, this may result in reduced torsional stiffness of the link, which should be studied and manipulated as needed.

Chapter 11: Tray Geometry Optimization Study

A study was conducted to find the optimum material geometry for the tray. Previous design requirements have determined the bounding inner and outer cross sections. Initial deflection simulations determined that leaving the sidewalls of the link solid resulted in a design that was rigid, but excessively heavy. However, if the sidewalls are reduced to the minimum machinable thickness of 0.125 inches, shown in Figure 11.1, the link becomes unacceptably compliant.

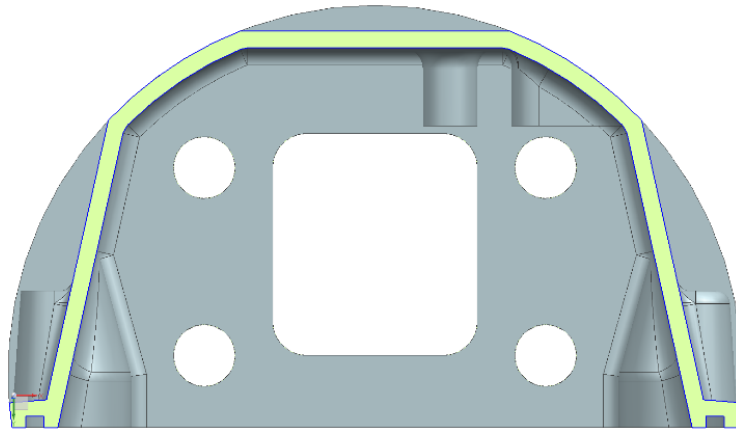


Figure 11.1: Cross section of the link featuring the minimum wall thickness

Using these two extreme cases as bounds, the following designs were explored. To limit degrees of freedom in this design study, the base material was set to 7075-T6 aluminum, no other materials could be added to the system, and the final design must be machined using subtractive methods.

11.1 Varied Wall Thickness

The simplest method to lighten the outer walls was to find the minimum wall thickness that achieves the desired stiffness. This was a simple process, allowing the optimizer to manipulate the thickness of each of the three walls independently while targeting a minimum torsional stiffness. The result, shown in Figure 11.2, reduced the mass of the link marginally, but not to any desired range.

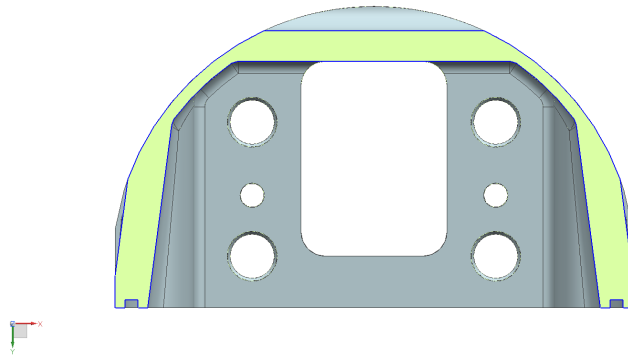


Figure 11.2: Cross sections of the link featuring optimized wall thicknesses.

11.2 Flange

To reduce mass but maintain bending stiffness while keeping machining simple, a stiffening fin design was created, pictured in Figure 11.3. The concept was to add I-beam-like flanges to the exterior of the link housing to increase bending stiffness. While this design did function properly in bending, it was not stable in torsion. This design was not put through the optimizer, as it was determined to not be viable at even its extreme cases.

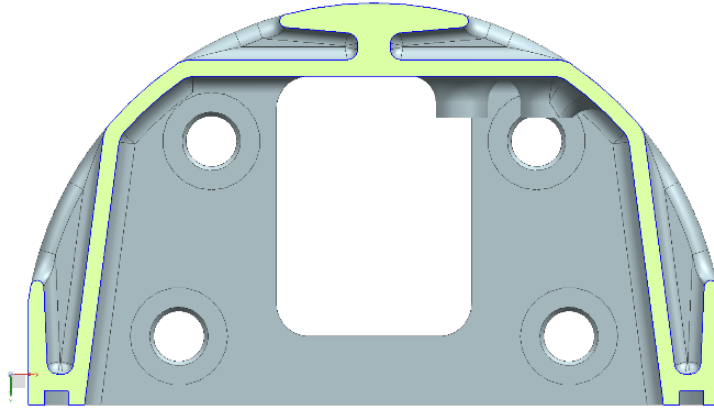


Figure 11.3: Cross section of the link featuring flanged wall features

11.3 Orthogrid

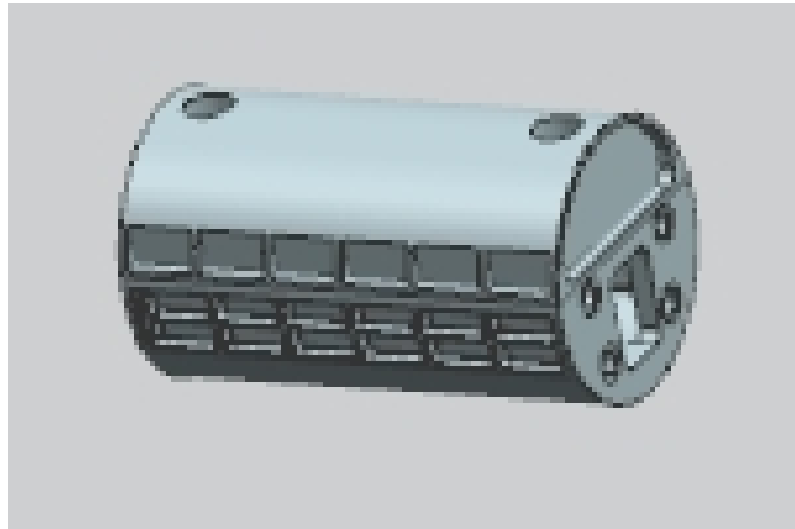


Figure 11.4: External view of the orthogrid geometry tested for the link ¹

Orthogrid geometry is orthotropically stiff across the surface it occupies. This is frequently used on the exterior of a pressurized cylinder, given the two primary forces: hoop stress and axial stress. This can be found everywhere in aerospace, from the fuselage of a plane to the pressurized modules on the space station. It is

¹Due to a computer error, the archived copy of this design was lost. This is the best image available, taken from an uncorrupted thumbnail.

a useful geometry to prevent buckling of a thin outer shell. Coincidentally, when applied to this design, the minimum machinable thickness for the inner wall is not very susceptible to buckling. Extremes of this geometry were unsatisfactory when the structure was subjected to torsion. Geometry optimization was not conducted.

11.4 Isogrid

Another common geometry used for stiffening structures is isogrid. This geometry was created with the intention of creating a surface that is isotropically stiff at the node points. Unlike the flange and orthogrid geometry, this has a high torsional stiffness and optimization was allowed to proceed. Isogrid has multiple geometry features that can be varied for optimization, so preliminary manual searches were conducted to down-select optimization variables.

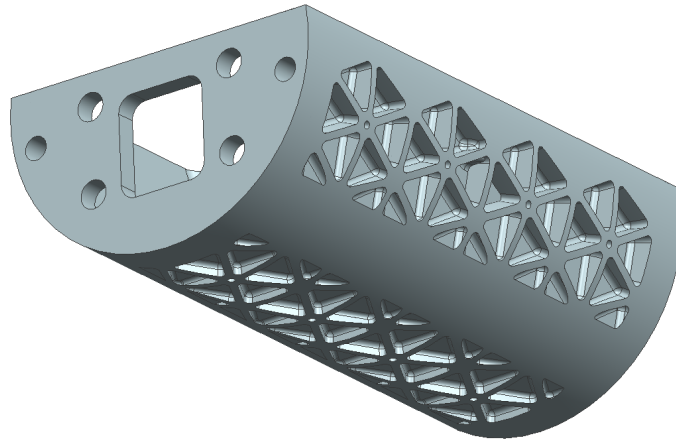


Figure 11.5: External view of the tray featuring isogrid lightening geometry

11.4.1 Base Geometric Design

The *Isogrid Design Handbook* [1] describes various methods of analytically designing isogrid for certain scenarios. Isogrid designs on cylinders are generally optimized for two primary loading conditions: axial and torsional stiffness. This is achieved by aligning one of the three rib chords either along the axis of the cylinder or along the diameter respectively. In this case, the latter orientation was selected, as the biggest design limitation has been the torsional stiffness of the link.

It should be noted that due to the ratio in this design between rib height, node separation, and wall thickness, it does not observe the classical properties of an isogrid. In a classic isogrid, the wall of the structure carries the bulk of the load, and the ribs exist to stiffen the wall from buckling and other phenomena. In the case of the design in Figure 11.5, the ribs take the bulk of the load of the structure. This makes the structure more of an isotruss than an isogrid, since it behaves as if there is no wall. We are able to design in this region because of improvements in finite element methods since the creation of the *Isogrid Design Handbook*.

Node spacing is another important aspect to isogrid design. While it can be used as a variable for improving the specific stiffness of a design, node spacing is more frequently altered to improve mounting point position. In this design, nodes are spaced to align with the fasteners for the lid. Coincidentally, this eliminates the geometry generated through an extensive study to find the minimum parent material geometry about a threaded hole. The results of this study are noted in Appendix C.

11.4.2 External Mounting Points

A beneficial design aspect for isogrid is the geometry of the nodal points. Because of the rounded corners of the equilateral triangle pockets, a somewhat massive region of featureless volume remains at the nodal points. In some instances this volume is diminished by a circular hole bored into the node. This feature can be sized to have little to no impact on the performance of the isogrid surface and is an additional mass saving measure. However, the nodal area can also be used as a mounting point, taking advantage of the unused material volume and the flexural properties of the isogrid at its nodes.

External mounting points on a link body are of great utility for several reasons. Fiducial based visual tracking systems require accurate knowledge of the locations of the markers. By adding an absolute set of mounting points on the surface of a robotic manipulator, visual tracking markers can be attached and calibrated easily.

Mounting points also allow for the addition of additional structure. During testing of robotic manipulators it is not uncommon for them to suffer collisions, either with themselves or with the environment. This is true of RTSX as well. However, while industrial robotic systems are capable of withstanding such collisions, aerospace manipulators are far more fragile. To reduce the probability of damage to the system due to collision, a sacrificial cover was designed to be mounted to the exterior of the link. In the event of a collision, this plastic cover will crush to absorb energy from the impact. Thanks to the recent reduction of cost in 3d printing technologies, we are able to produce replacement cages cheaply and quickly in house,

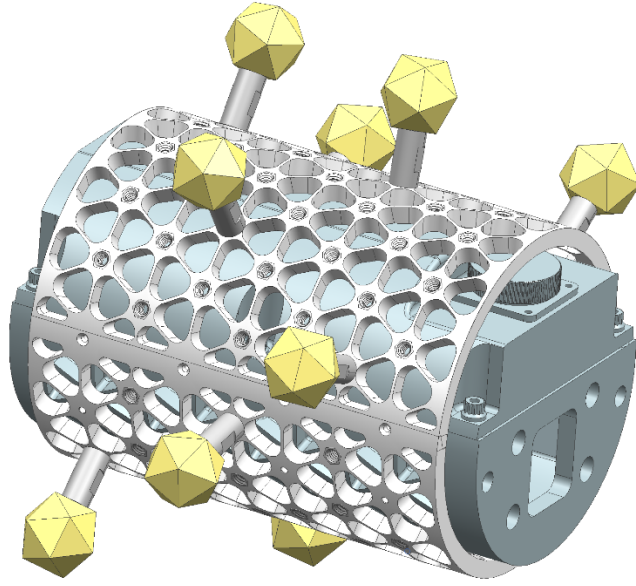


Figure 11.6: Reflective fiducial markers attached to a protective housing making a disposable crash cage affordable. A rendering of this design is shown in [figure 11.6](#)

11.5 Optimization Method

Optimization was carried out by using the Geometric Optimization toolkit built into Siemens NX [\[2\]](#). This toolkit navigates the design space by manipulating selected variables, such as the thickness of the isogrid web, and testing the design in finite element analysis (FEA) software. In this instance, the optimization was carried out using the NX NASTRAN Solver 101, observing maximum angular deflection of the link. The finite element analysis performed used the extreme tip loading cases found in [Table 5.1](#).

Optimization of the isogrid geometry was done by varying the wall thickness of the tray and the web thickness of the isogrid. The test case was torsional loading

of the assembled link and lid, using the maximum angular deflection as the output for the optimizing function. Additional geometry was attached to either end of the simulated link in order to mimic the properties of the joint hardware at either end of the assembly. The goal of this process is to engineer a link with the required stiffness and minimum mass.

Initial finite element runs were conducted using an initial wall and web thickness of 0.04 inches. While not easily machinable, it is within a generous span of potentially manufacturable geometries. The results of this first simulation are shown in figure 11.7, which depicts the absolute nodal displacement. In this figure, the center of shear is visualized by the blue dot on the closest face, the area of least displacement since it is the center of the rotation. Note that with this very thin geometry, the center of shear is almost centered on the mid-line of the link.

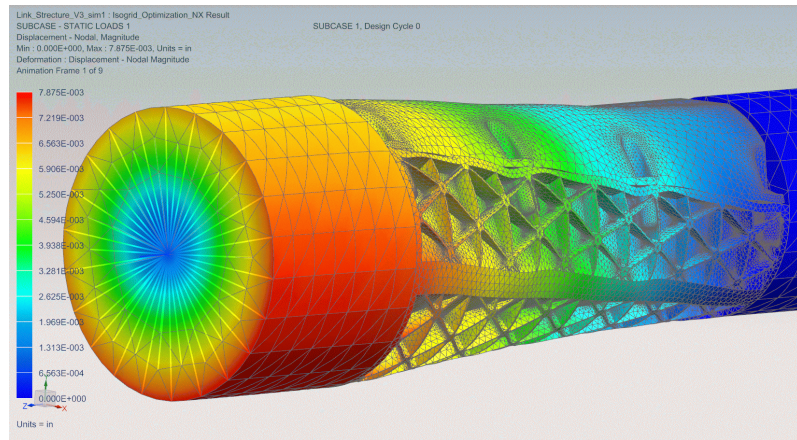


Figure 11.7: Isogrid geometry optimization, step 1

The design converged to a nominal thickness of 1/8 inch, an easily machinable geometry. Figure 11.8 shows the results of the final simulation, depicting the absolute nodal displacement again. Observe that not only is the magnitude of dis-

placement smaller, but the center of shear has shifted. While previously considered to be undesirable, it was found that a moderate amount of eccentricity of the shear center is allowable if a higher torsional stiffness can be achieved.

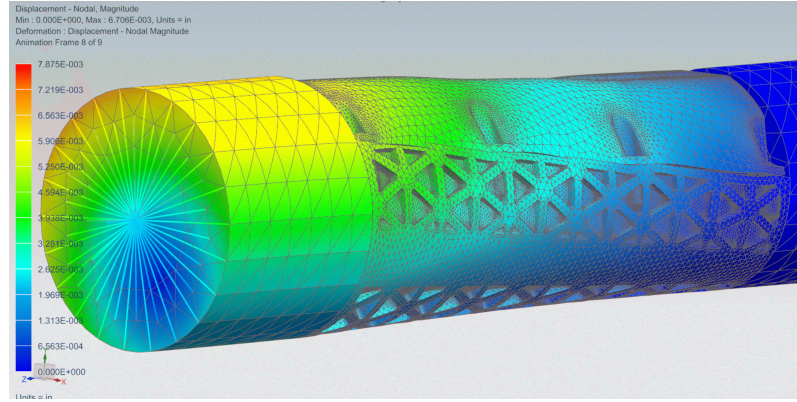


Figure 11.8: Isogrid optimization, final iteration

11.6 Conclusions

This design method explored the possible lightening geometry for the exterior of the link tray. The process was conducted assuming the interior boundaries were invariable and predefined by the motor controller packaging study which was previously conducted. The exterior boundary was formed by the diameter of the original link, a geometry which prevents self-collision of the links. This study explored five different methods for lightening the exterior geometry while maintaining adequate bending and torsional stiffness. Further lightening methods could be explored, but the performance produced by the selected isogrid design was found to be acceptable and the iteration study stopped, although further iteration is possible.

Chapter 12: RTSX Standard Internal Interface

The RTSX platform features six unique mechanical interfaces between the joint modules and their accompanying link body, or the previous link. These are shown in figures 12.1 and 12.2. A question arises as to approach: should a unique link body be manufactured to interface with each joint module, or should a component be manufactured to adapt each joint module to a standard mechanical interface? This was prototyped to understand the constraints imposed on the design space.

The original design for DXE used stainless steel fittings for both side of the marman band interface. This served as the only adapter in the kinematic chain of DXE. PXL used a large mounting plate to attach the electronics housing to the joint module, which when removed allowed for access to the internals of the transverse

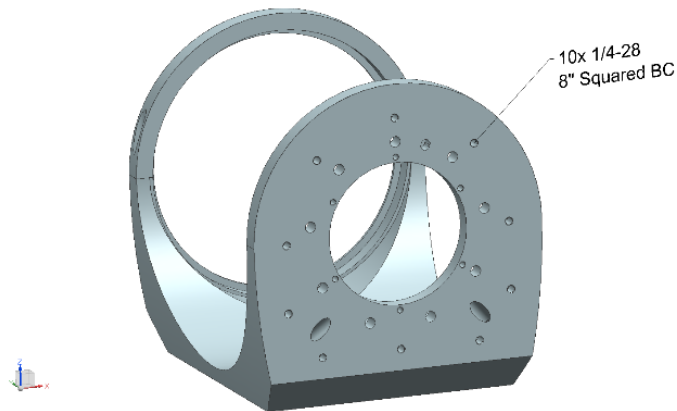


Figure 12.1: PXL electronics mounting interface

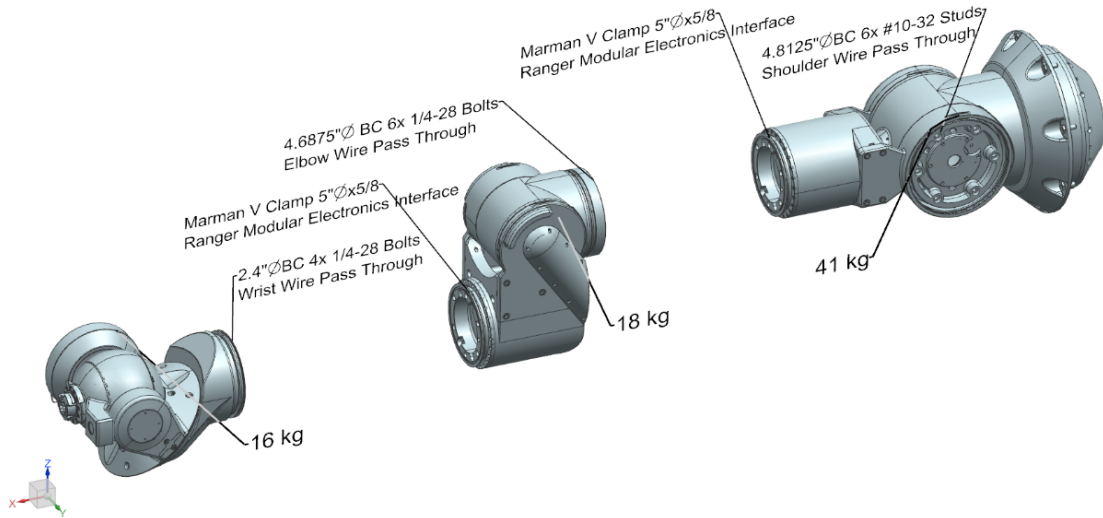


Figure 12.2: DXE link mounting interfaces

link. Both of these adapters in DXE and PXL are heavy, constructed from stainless steel or thick aluminum. This approach was re-thought for the DXE prototype housing, opting to make the marman interface an integral feature on the link body, rather than a separate part.

A survey was taken of all of the mechanical interfaces across the reused hardware from the original RTSX design, depicted in figure 12.3. It was found to be possible to remanufacture the mating components to have a more advantageous connection scheme. This was investigated but deemed too costly given the size and complexity of the components involved. Therefore, a common link design was created, using adapters to connect to existing hardware.

	Original		Test		Final	
	Proximal	Distal	Proximal	Distal	Proximal	Distal
Wrist Link	●	○	○	●	●	●
Elbow Link	●	○	○	●	●	●
Shoulder	○	○	●	●	●	○
PXL	●	○	N/A	N/A	●	○

Figure 12.3: Use of adapters between joint modules and link bodies in all three RTSX revisions

12.1 Load Transfer

The RTSX standard link interface is the point of highest stress in the entire RTSX kinematic chain. The available area for fasteners is very limited by packaging concerns, drastically reducing options for connecting the link body to the system.

A regular distribution of fasteners across a surface will react an out of plane moment about the elastic center of the distribution. For symmetric distributions such as bolt circles or four bolts in a square, the elastic center is also the center of the bolt circle or square. As the bending plane is rotated about this elastic center, a set of limber and stiffer axes of bending are established. The most limber axis of bending will yield the maximum pullout force on a single fastener for a regular distribution. For a rectangular bolt pattern, the worst case pullout force applied to

each bolt given an applied moment is defined by equation 12.1 and 12.1, produced by Moo-Zung Lee [3].

$$F = \frac{M}{2a \sin \theta_d} = \frac{M}{2a} \left(\frac{\sqrt{a^2 + b^2}}{b} \right), a \leq b \quad (12.1)$$

$$F = \frac{4M}{ND}, N \leq 3 \quad (12.2)$$

A variety of bolting patterns were analyzed to find an acceptable mounting pattern. Exploration of the geometry found that the maximum dimensions of a rectangular bolt pattern were 1.375 by 2.5 inches with a 5/16 bolt diameter. Using the formula in figure ?? and the loading conditions in Table 5.1, the maximum tensile force on the bolt is 3200 lbf with a fastener stress of 41 ksi. Circular bolting patterns were limited by the half-moon shaped mounting area, making the maximum possible bolt circle approximately 1.5 inches in diameter with 6 fasteners and limited to 0.250 inch diameter bolts. The maximum tensile force is 1700 lbf with a fastener stress of nearly 35 ksi.

Since both bolting patterns yield approximately the same fastener stresses, other factors must be considered in selecting an appropriate layout. Finite element models were constructed of both fastener patterns to explore potential issues resulting from stress flow. This revealed that the bolt circle layout generated a large bending moment across the bolted face. The moment is caused by the increased distance between the fastener and side walls of the tray. The rectangular bolt pattern places each fastener as close to the side walls as possible, reducing the bending distance to a minimum.

12.2 Surface Pressure

In most cases, fasteners are constructed from materials with a higher yield force than the parent material they interact with. This has an unfortunate effect on the fastened joint in where the parent material may start yielding before the fastener. The contact surface between a bolt head and the parent material must be examined for potential wear and eventual loosening of the fastener.

The bolts implemented on the standard RTSX interface are NAS6307-8 bolts, a 7/16-20 hex head bolt constructed from A-286 stainless steel. Each bolt has a tensile breaking strength of 17000 lbf and a contact area of 0.146 in², resulting in a maximum contact pressure of approximately 116 ksi. The parent material is constructed from aluminum 7075 with a yield strength of 73 ksi, which will cause the contact surface to plastically deform if the bolt is ever subjected to forces that high. If such an event occurs, it would be advantageous if the bolt deformed and broke before the parent material.

Shigley [4] models the compressed member under a bolt head as a frustra spreading from the bolt head to the midpoint of the grip. There is some debate over the half-angle of this cone, ranging from 45° to as small as 25°. Based on this range, the bolted connection would need to have a stiff washer to spread out the load to the maximum acceptable surface pressure with a thickness between 0.09 and 0.04 inches.

12.3 Reducing Thermally Induced Stress

There are several concerns in a bolted interface outside of load transfer and surface pressure. Galvanic corrosion and fatigue can lead to cycle induced failure of a bolted connection, but there is another more frequently overlooked phenomena that can be more damaging. Bolted connections are frequently built up with several different materials, all with different coefficients of thermal expansion (CTE). The defining equation showing thermally induced axial forces on the bolt are shown in equation 12.3 Considerations must be made for thermally induced stress caused by a differential between CTE in materials used in the connection.

$$\Delta F_T = \frac{\sum_{i=1}^n L_i \Delta T (CTE)_i - \sum_{j=1}^m L_j \Delta T (CTE)_j}{\frac{1}{\sum_{i=1}^n L_i \frac{E_i A_i}{L_i}} + \frac{1}{\sum_{j=1}^m L_j \frac{E_j A_j}{L_j}}} \quad (12.3)$$

$$F_y > \Delta F_t + \Delta F_{pl} > 0, \Delta F_{pl} > 0 \quad (12.4)$$

If the system exceeds the boundaries in Figure 12.3, it will be considered to have failed. If the sum of preload and thermally induced forces exceed the yield strength of any material in the chain, yielding will occur. Yielding would cause the fastened connection to loosen, possibly enough to remove all preload once the connection returns to its assembled temperature. If the sum of forces are negative, the connection will become loose, resulting in the same complications.

It is possible to create a bolted connection that is thermally invariant. If the proportions and CTEs of all components in the connection chain are selected carefully, the fastener and the sum of the parent materials will have the same effec-

$$\sum_{i=1}^n L_i(CTE)_i = \sum_{j=1}^m L_j(CTE)_j$$

Figure 12.4: Thermally invariant fastener chain

tive CTE. This is useful for decoupling the fastener preload from the CTE of the materials. This was done for the bolted connection in the RTSX standard interface.

The bolted section of the interface uses three different materials. The bolt is constructed from A286 stainless steel, the tray is aluminum 7075, and the thrust plate is titanium 6AL-4V. For simplicity, their CTEs from Table 1 have been copied to Table 11 below.

Table 12.1: Coefficients of thermal expansion for selected materials

Material	Location	CTE ($\mu\text{m}/\text{m}^\circ\text{C}$)
A286	Fastener	16.9
7075-T651	Tray Body	23.6
Ti 6Al-4V	Thrust Plate	8.6

The wall of the tray body has a known thickness of 0.333 inches and the thrust plate has a minimum thickness of 0.15 inches, as determined in Section 12.2. Solving for the thickness of the thrust plate, we find that the invariant plate thickness exists at about 0.27 inches thick. For flight designs this is highly desirable, but was not possible for this design iteration due to cost.

12.4 Fatigue

It is easy to overlook the loading cycles for fasteners in any design. For a robotic manipulator, the number of cyclic stresses the system will endure throughout

its lifetime is quite large. For that reason, the fatigue life of the fasteners used in the primary structure must be considered. While there are many different schools of thought and analytical methods for determining fastener fatigue life, NAS standards for fastener design were used. Design standards for high cycle fatigue dictate that the fastener must be loaded to 10% of its total yielding strength at maximum. This results in a fastener that is greatly over-sized for all other purposes, but will not fatigue through the lifetime of RTSX.

12.5 Galvanic Corrosion

RTSX is designed to operate in a submerged environment, making it susceptible to galvanic corrosion. To combat this, the exterior of RTSX is constructed almost entirely from anodized aluminum. While the anodized coating is effective at eliminating galvanic corrosion, difficulties arise at bolted interfaces. These fastener assemblies feature bolts that do not match the galvanic potential of the aluminum it is bolted into. Unaddressed, this will cause the interface to quickly corrode. For that reason, the following mitigation measures were taken to reduce or eliminate galvanic corrosion. The abrasion caused by the tightening of fasteners or applying threaded inserts allows for oxidation and other coatings to wear. This can be seen in the exterior bolts used to hold the base of PXL to its test platform in Figure [12.5](#).

To eliminate galvanic corrosion in the primary structure chain, fasteners are shielded from the environment by o-rings. This allows for material selection for the primary structure to be conducted without concern for the galvanic index of the

Table 12.2: Galvanic index of materials used in RTSX, taken from [5]

Material	Min. Galvanic Index [Volts]	Max. Galvanic Index [Volts]	Area of Use
7075-T651	-0.78	-0.7	Primary Structure
316 Stainless	-0.18	-0.1	Helical inserts and pins
Ti-6Al-4V	-0.12	-0.04	Exterior fasteners
A286	-0.19	-0.11	Primary structure fasteners



Figure 12.5: Galvanic corrosion of the threaded holes on the base of PXL

materials, but is difficult to package correctly.

Note the pattern of corrosion found on the PXL base, shown in figure 12.5 as a white chalky buildup about the threaded feature. This galvanic corrosion is caused by interaction between the parent material, fastener, and stainless steel threaded inserts. Outside of the threaded feature and the countersunk hole it sits in, no corrosion can be observed other than mild discoloration. Neither the coating standard specified [6] nor the production drawing states that this feature should be masked before or machined after the anodizing process. This corrosion is most likely due to damage sustained while assembling the helical inserts. Note that the threaded feature on the left has not sustained the same level of corrosion.

The prevalence of corrosion between parent material and threaded inserts is

problematic for the implementation of the threaded feature for the lid. This feature must be exposed to the environment, so an adequate barrier between the thread insert and the parent material must be formed. To solve this, a barrier coating is pre-applied to the inserts used on the lid which should inhibit any potential corrosion caused by assembly abrasion.

Chapter 13: Thermal Analysis of Original RTSX Design

The DXE link design integrated the servo drivers directly with the primary structure. This reduced the number of parts and the number of thermal and mechanical interfaces. The electrical system was subject to several failures during development. Multiple failures of the motor driver module and digital to analog converter occurred due to an unknown and inconsistent mechanism. Failure was attributed to assembly error and thermal issues by the operators, who remedied this with a few design adjustments. In this section, a theory will be proposed as to why these components suffered frequent failure, demonstrate how this mechanism occurred, and justify several aspects of the redesign of the system.

13.1 Critical Components of Original Design

The original RTSX link structure was heavily integrated with a modular back-plane design. The servo drivers sat perpendicular to the link body and penetrated all the way through the structure. The link was produced by casting to allow for several internal features unavailable with subtractive machining. The majority of the design was finish machined with computer numerically controlled (CNC) milling, but the card cages were finished via wire electro-discharge machining (EDM) due

to their thin but deep geometry. To waterproof the link design, the card cage was encased with a stainless steel sheath which did not touch the cage. This meant that all thermal load generated by the servo drivers must be conducted along the link to either end where it could then be conducted to the environment. This design feature limited the arm operationally, as it could not run on a continuous duty cycle without overheating.

Wedge-Lok fasteners sat on either end of the servo driver board. They serve two functions: locking the servo driver daughter card into place, and compressing the heat spreader against the body of the link. The Wedge-Lok design was intended to transfer heat out of the system through the clamped area directly under the Wedge-Lok, similarly to the VPX standard discussed later. The final design used this to also compress thermal grease across the entire motor driver card to increase its transfer area.

The motor driver module was a large rectangular module and accounted for nearly all of the thermal load generated in the drive electronics for RTSX. The module was heat sunk through a milled hole in the back of the servo driver PCB, against the heat spreader. This module contained only the drive electronics to commutate signals from the motor, and to apply appropriate voltages and currents to the brushless motor it controls. While its thermal output varied, it was estimated at forty watts peak.

The servo driver heat spreader, pictured in [Figure 13.2](#), conducted heat from the motor driver directly into the link body behind it and to the Wedge-Lok interface at both ends of the card. There are several points where it contacted the PCB, which

conducted away some heat, but more importantly prevented the heat spreader from shorting against the servo driver. Thermal grease was applied between the motor driver module and the heat spreader, as well as the heat spreader and the link body to increase conductivity and account for any surface imperfections.



Figure 13.1: Top view of the servo driver board

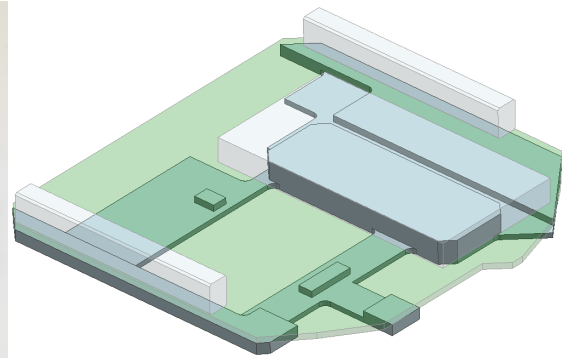


Figure 13.2: Computer rendering showing the geometry of the heatspreader

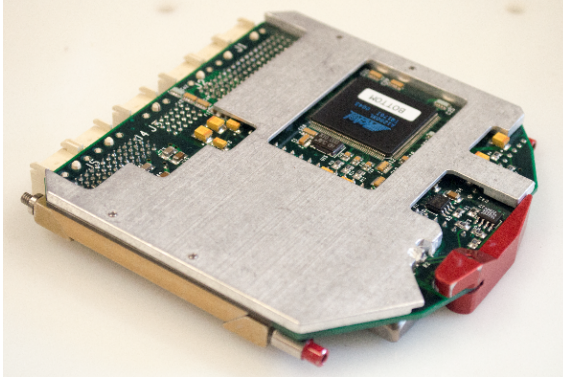


Figure 13.3: Bottom view of the servo driver

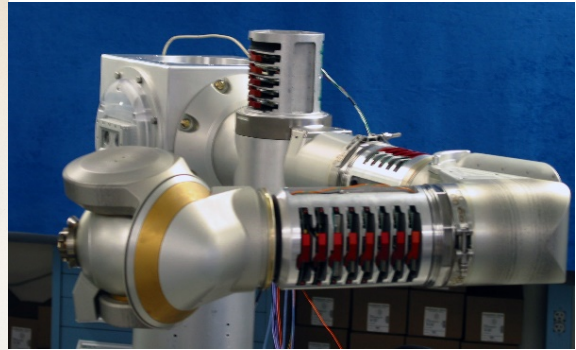


Figure 13.4: Servo drivers installed in RTSX

13.2 Design Comparison to VPX Standard

This design bears a similarity to the VPX/VME64 standard frequently found in military and aerospace computer systems. The standard connects a daughter

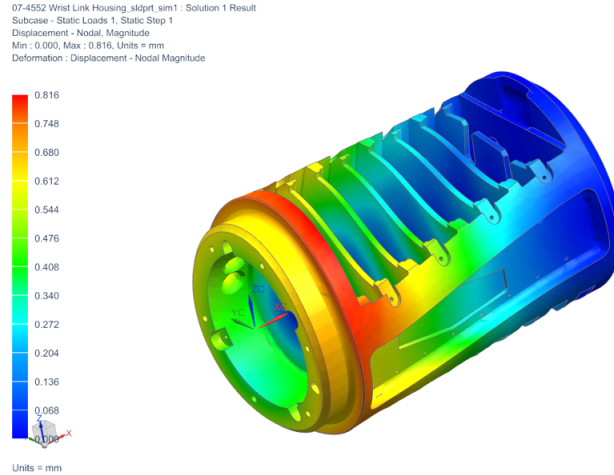


Figure 13.5: Finite element simulation of original forearm link showing out of plane warping of the card cage

card to a backplane, and conducts all heat out of the system through a cold plate and into the clamped Wedge-Lok ends. However, the heat spreader on RTSX is insubstantial compared to the normal VPX implementations. The thermal flow in this component should be studied further.

13.3 Preliminary Inspection

Inspection of the link structure reveals that its basic shape is two parallel rails connecting the proximal and distal end of the structure, tied together with multiple thin plates. In bending and torsion, this design proved sufficiently stiff for nominal operation. This part suffers from a reduced torsional stiffness, as it features only two separate continuous rails that run the length of the casting. As the link is torqued, the card cages deform and warp. The planar feature separating each card is no longer planar and has deflections up to one millimeter. This is of great concern as its surface is the only conduction path for the servo drivers.

13.4 Failure Theory

While the failure of the motor driver modules was originally attributed to thermal failure, the elements of the failure may be much more complex. As seen in the preliminary analysis, the link body, and by extension the card cage, cannot be considered rigid. This can allow for the following failure mechanisms for the servo driver.

13.4.1 PCB Flexure

Flexure of the card cage can lead to flexure of the printed circuit board (PCB) and its components, leading to premature failure. As this is a difficult mechanism to examine due to the intricacy of the assembled board, we will leave this mechanism mostly unexamined analytically.

13.4.2 Excessive Mating Pressure

The heat spreader directly contacts the motor driver. As the assembly bends and flexes, it is possible to generate regions of high force from excessive mating pressure on the module. This mechanism can be examined through finite element analysis, though interpreting the results may be too subjective as even a low pressure could cause fatigue failure.

13.4.3 Motor Driver Failure

Similar to PCB flexure, this mechanism may play a large role in failure, but is very dependent on the complex interaction of electrical components inside the module. This should be observed, but further study was not possible within the scope of this project.

13.4.4 Separation of the Heat Spreader from the Card Cage

We can safely assume that the area of the heat spreader located below the Wedge-Lok clamps are held firmly in place. However, it is possible that the majority of the area for the heat spreader could separate from the card cage. This is not a critical failure point, as the heat able to transfer through the Wedge-Lok should be sufficient.

13.4.5 Separation of Heat Spreader from Motor Driver

This mechanism is arguably worse than separating the heat spreader from the card cage. Once separated, there is no thermal path out of the motor driver module, save for the pins connecting it to the PCB. This has the added effect of disconnecting the temperature monitor located on the PCB, which would allow for unobserved thermal run away of the servo driver.

With the possible failure modes established, we can form a finite element model to better judge these failure mode influences. Model geometry for the upper arm link, PCB, Wedge-Lok, heat spreader, and the motor driver were all created and

then greatly simplified. Geometry that is of the most influence; the heat spreader, PCB, and link body was preserved as accurately as possible. Connector pins were replaced on the motor driver with a thin wall, and nearly all of the geometry on the Wedge-Lok was eliminated. Only a single card was modeled near the center of the housing for mechanical stress simulation, as this is the region of largest warping of the card cage.

13.5 Steady State Thermal Design Investigation

To understand the impact on heat spreader separation, nominal thermal operation was studied. Using finite element analysis, the card cage design was evaluated to examine performance with or without conduction through the back of the heat spreader. For completeness, this is also explored for one or all servo drivers at max thermal flux. The following evaluation was done using NASTRAN SOL153 and observed only steady state temperatures.

The motor driver module has a maximum thermal flux of approximately 40 watts, and the joints that the link conducts heat out of has an approximate maximum temperature of 60 degrees centigrade. The motor drivers have a maximum operating temperature of 125 degrees centigrade, above which we can assume they will incur damage.

All of these simulations were performed assuming perfect conduction across mating surfaces, most importantly the card cage to the heat spreader and the heat spreader to the motor driver module. As there is no margin or even negative margin

Table 13.1: Steady state motor driver temperatures under various contact and loading conditions

Test Condition	Maximum Temperature °C	Failure Margin °C
Single controller with only Wedge-Lok conduction	125	0
All controllers with only Wedge-Lok conduction	170	-15
Single controllers with full heat spreader conduction	87	38
All controllers with full heat spreader conduction	100	25

allowed for operating without conducting through the rear of the heat spreader, it can be concluded that some amount of rear conduction is required. This is evident from the physical hardware, as many motor driver cards had thermal paste applied to the rear of their heat spreader with the intent of doing just that. With this knowledge, it can be safely assumed that separation of the heat spreader from the link body is capable of causing thermal damage to the motor driver module.

13.6 Contact Pressure Evaluation

Analysis was performed using NASTRAN to calculate contact loops and observe contact pressures. Initial contact pressure for the motor driver module was established by enforcing the maximum tolerance interference with the heat spreader. Seven different loading conditions were simulated to observe the various loading pressures on the heat spreader from both the motor control module and the card cage. For the purposes of this analysis, a contact pressure of zero is considered not contacting and therefor thermally insulated.

The highlighted region in Figure 13.10 shows the contact pressure on the interface between the heat spreader and the card cage, directly behind the motor

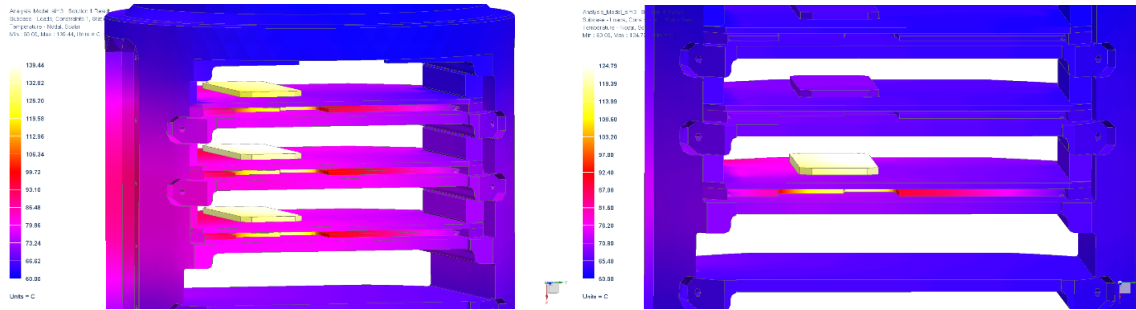


Figure 13.6: All controllers powered, Figure 13.7: Single controller powered, Wedge-Lok conduction only

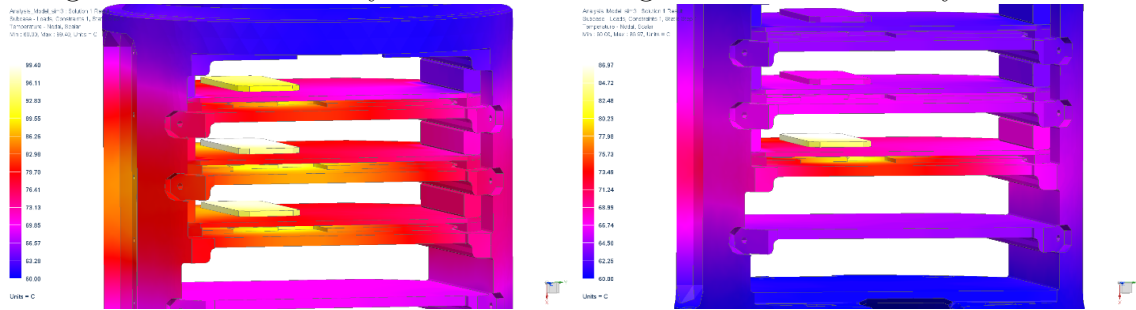


Figure 13.8: All controllers power, conduction through the full heat spreader

Figure 13.9: Single controller powered, conduction through the full heat spreader

driver module. Contact pressure between the heat spreader and the motor control module is concentrated sharply along one outer edge. This appears to be due to the increased stiffness around this region. Observing Figure 13.10 it can be noted that this region of high pressure is close to the edge of the card, and also features a larger volume of the heat spreader. Due to an access window cut into the body of the heat spreader, the centerline of the component has nearly no bending stiffness and is unable to react the forces evenly. Already we are able to observe a point of thermal resistance, as the heat spreader does not apply pressure to the majority of the surface it is conducting to and from.

To test mechanical deflection and change and surface pressure, one end of the link housing was fixed and moments were applied to the other. As a long serial

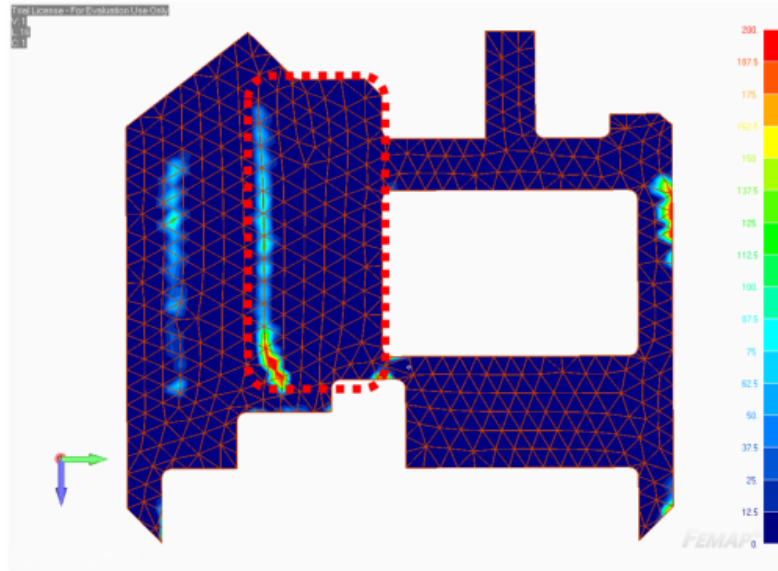


Figure 13.10: Unloaded heat spreader pressure distribution. The area under the motor driver module is highlighted with a red dashed box.

manipulator such as RTSX is accurately modeled using Euler-Bernoulli beam theory, the dominant forces on the link body are bending moments. This analysis was done using the maximum nominal bending moments the link will experience. Impacts, overloading, and manufacturing defects will likely yield more extreme results; however, that is beyond the scope of this analysis.

There was no appreciable change in contact pressure for the interface between the heat spreader and the motor driver module while under bending. Similarly, at the interface between the heat spreader and the card cage, only the very edge of the heat spreader makes any measurable contact. While there may be a growing gap in the non-clamped region of the module, analyzing the effects of that accurately is beyond the scope of this study. What can be said from this analysis is that the contact pressure is not distributed across the component, and that the efficiency of thermal transfer will be reduced.

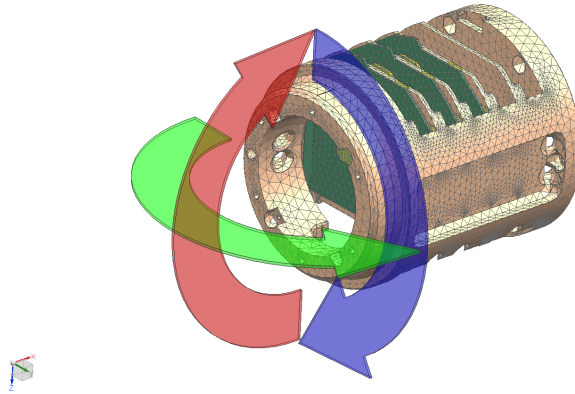


Figure 13.11: Applied moments. The red, green, and blue arrows represent positive vertical bending, positive horizontal bending, and positive torsion respectively.

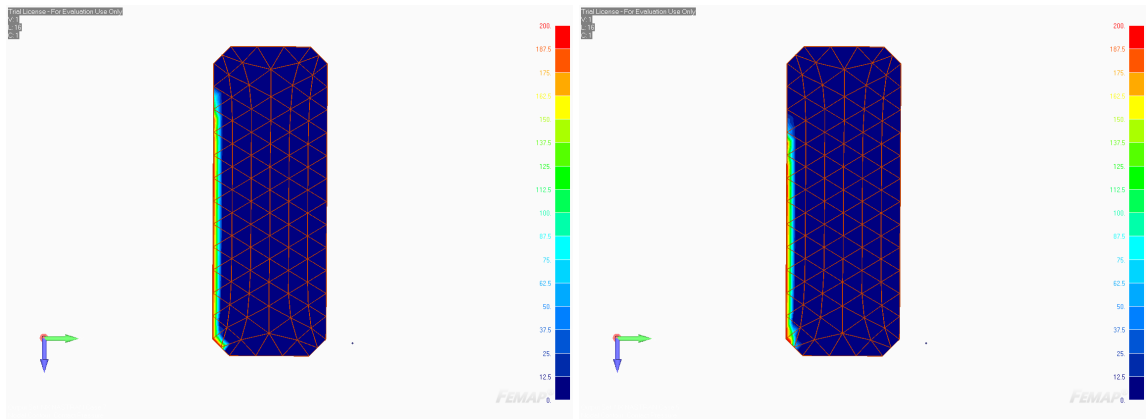


Figure 13.12: Contact pressure on the motor driver module, unloaded

Figure 13.13: Contact pressure on the motor drive module, worst case loading

Several observations can be made by examining the contact pressure distributions of the six primary loading cases shown in figures 13.14 through 13.19. As predicted, torsion of the link does affect the pressure distribution on the motor driver, though they are comparable to the distribution change for vertical bending. This is to be expected, as vertical bending produces comparable bending in the card cage. Vertical bending causes nearly no change in pressure distribution.

The severity of change in contact pressure as a result of nominal structural loads is of great concern. While a vertical bending event does not greatly affect the

contact pressure, torsion and horizontal bending nearly separate the contact area completely.

13.7 Failure Method Review

Earlier in this chapter, five possible failure modes were stated. Given the analysis above, the following statements can now be made.

13.7.1 PCB Flexure

Mechanical stresses and strains measured in the simplified finite element model were far below yielding for any part of the board. While it was found that flexure did occur, it is not known if that would have definitively impacted any component.

13.7.2 Excessive Mating Pressure

Mating pressures were concentrated into small regions across the entire motor driver board and its components. However, there was no evidence that any of these pressures were large enough to cause any component to fail.

13.7.3 Motor Driver Flexure

The motor driver module was modeled as a solid epoxy block of equivalent dimensions. While the module did flex and had some mechanical stresses, they were nowhere near the estimated yielding strength. Similarly to the PCB Flexure theory, this may have impacted the component performance, but it is not possible

to estimate that given our knowledge of the system.

13.7.4 Separation of Heat Spreader from the Card Cage

As demonstrated, this is the most problematic mechanism and was most likely the root cause of failure.

13.7.5 Separation of Heat Spreader from the Motor Driver

Pressure distributed across the motor driver module was insufficient and created a poor thermal path. This pressure also varied and lessened during flexure of the card cage. Overall, this region is under-performing and may have led to a reduced operational duty cycle.

13.8 Conclusions

With this knowledge, several simple modifications can be made to this card system to improve its performance. If the heat spreader material is changed from aluminum to copper, the peak temperatures while only conducting through the Wedge-Loks changes from 170°C to 108°C. The geometry of the heat spreader could also be altered to equalize bending stiffness across the component to distribute clamping force evenly and reduce inefficiencies in the system. By not depending on contact through the rear of the heat spreader and by increasing the efficiency of the thermal junction between the motor driver module and the heat spreader, the coupling of mechanical flexure and thermal performance should be substantially

reduced.

Systematically, this has demonstrated multiple problems with prior packaging of electronics which require large thermal dissipation inside of the primary structure of a robotic arm. The primary structure cannot be assumed to be rigid, and its flexure could be quite problematic to sensitive electronic components. Due to this flexure, it is suggested that the electronic systems are mechanically decoupling from the primary structure as much as possible. This can be problematic where thermal junctions or high vibrations exist, but as is demonstrated later in this paper, it is possible. It is also suggested that the length of the thermal path be reduced to increase thermal efficiency. In the original RTSX design, heat must travel at least half the length of the link before it can be dissipated. This can be greatly improved if a few design aspects are changed.

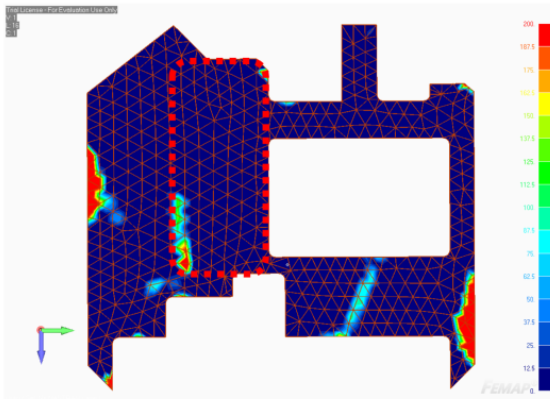


Figure 13.14: Pressure distribution on the heat spreader under positive torsion

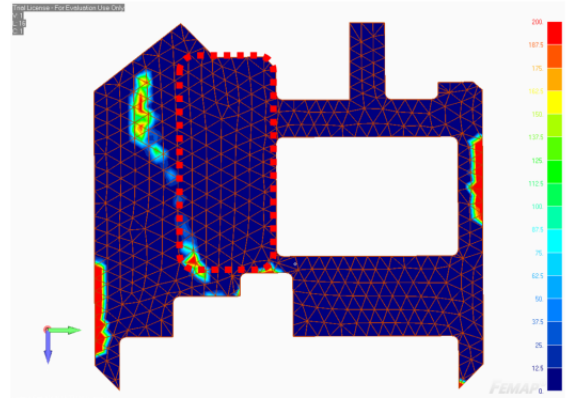


Figure 13.15: Pressure distribution on the heat spreader under negative torsion

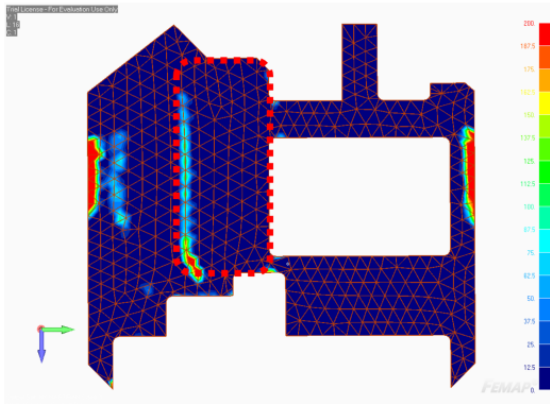


Figure 13.16: Pressure distribution on the heat spreader under positive vertical bending

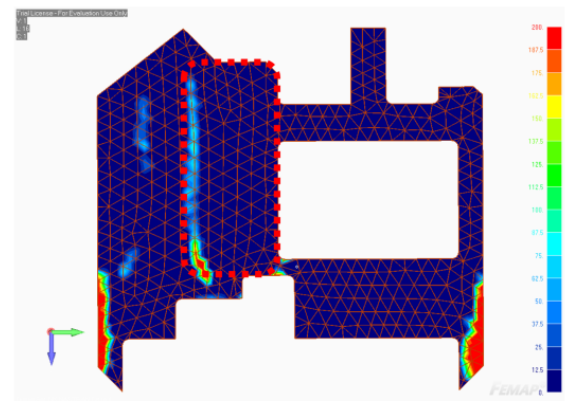


Figure 13.17: Pressure distribution on the heat spreader under negative vertical bending

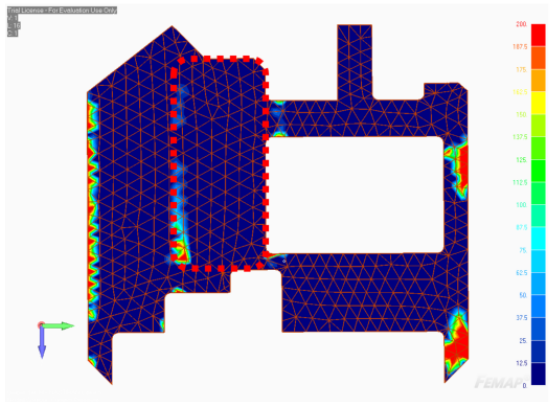


Figure 13.18: Pressure distribution on the heat spreader under positive horizontal bending

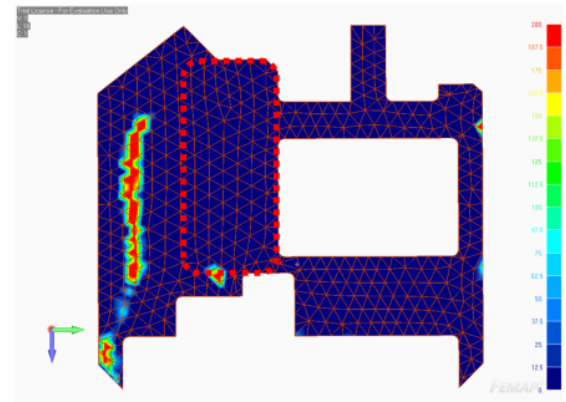


Figure 13.19: Pressure distribution on the heat spreader under negative horizontal bending

Chapter 14: Thermal Redesign

To improve performance and reliability, the thermal management system for RTSX was completely redesigned from the original concept. The redesign considers mechanical isolation, packaging, and thermal flow with the goal of reducing the system temperature while preventing flexure of the link body from flexing the servo drivers.

14.1 Mechanical Isolation

In the previous design, servo drivers were rigidly clamped on both sides by Wedge-Loks. This rigid connection caused the forces in the card to be statically indeterminate, and allowed the PCB to be twisted and bent by the flexure of the link housing. To prevent this from occurring, the connection method was rethought assuming the link body it mates to will flex under load.

Grüblers formula, equation [14.2](#), solves for the number of degrees of freedom (F) of a system. The input is the number of links (L) (including the world frame), the number of joints (N), and the degrees of freedom for each joint (f_i). Figure [14.1](#) details the kinematic diagram for holding a servo driver against the inside wall of a link, showing five link bodies (including the world frame), six joints, and a sum total

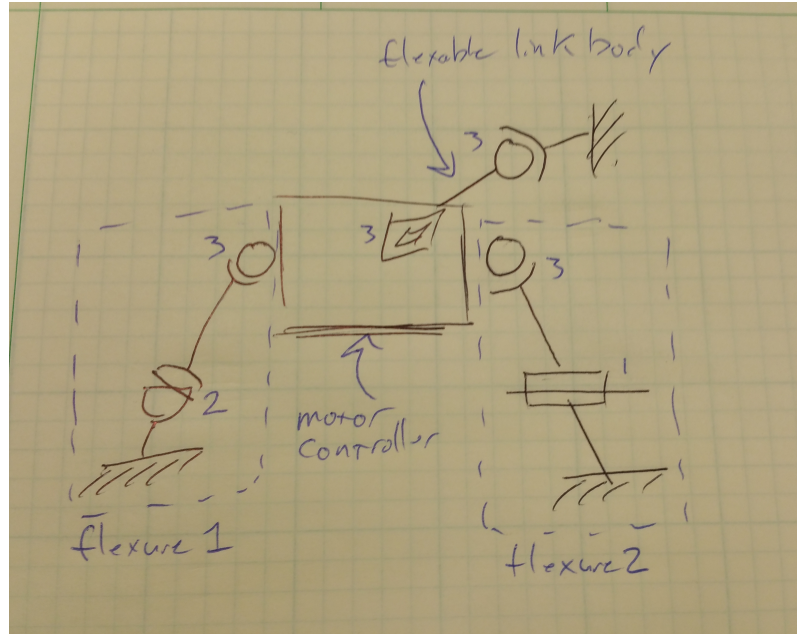


Figure 14.1: Kinematic diagram of the servo driver retainer

$$F = 6(L - N - 1) + \sum_{i=1}^N f_i$$

Figure 14.2: Grübler's formula for calculating degrees of freedom in a mechanism

of 15 degrees of freedom. Using Grüblers formula, three degrees of freedom remain in this system. These degrees of freedom are the three rotational degrees that the motor controller can move in to compensate for primary structure flex, allowing it to maintain constant contact with the wall. As it is assumed that the heatsink has a sliding contact against the inner wall of the link, the only forces imparted to the servo driver as a consequence of the link flexing are a small change in contact pressure due to the linear spring rate of the retaining arms. This is discussed further in section 14.2.

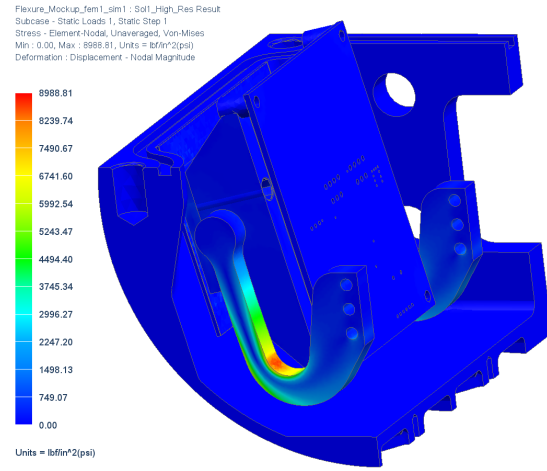
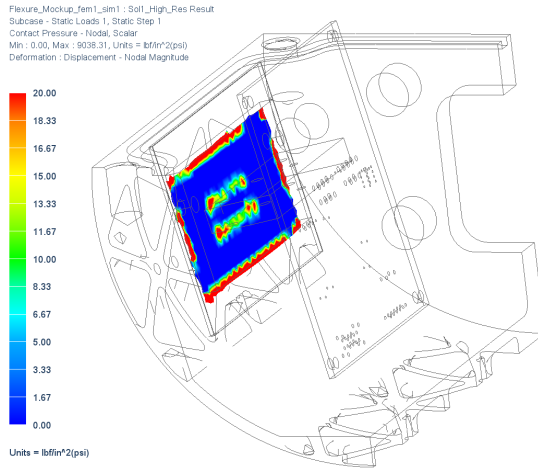


Figure 14.3: Finite element analysis showing surface pressure gradient at the servo driver contact

Figure 14.4: Finite element analysis showing stress in the pre-loaded retaining arm for the servo driver

14.2 Retaining Arm Design

One of the unique challenges in this design is to apply rigid clamping pressure to the heatsink of the HPU across a wide gap. Normally such a design is accomplished with spring loaded bolts or wedge-loks. Instead, a novel method of retaining electronics must be created to satisfy this design. This uses two semi-flexible can-

tilevered arms to hold the motor controller against the outer wall and provide a constant clamping force by virtue of their spring rate.

14.2.1 Deformation Method

The retaining arms themselves can take on several forms. Original concepts had the retaining arms use torsion springs to push a solid lever arm. While this has the benefit of a discrete moving part and high stiffness outside of the intended motion, it does suffer from several drawbacks. At the scale required by the design volume, there are few commercially available springs that will exert the desired force. It is nearing the limit of simple torsion spring design.

Tension spring based articulations were also explored, but they suffered from similar problems. These discrete-spring based articulations are costly due to the number of components required. They also suffer from high surface pressures, making their durability low. Instead, a flexible structure was explored.

The final spring arm design uses a flexible cantilevered arm with all necessary geometry machined into it. The geometry of the design was dictated by three factors: desired tip stiffness of the cantilevered beam, maximum stress in the cantilever beam, and maximum stress in the interface between the beam and the mounting rack. The former two are defined by the Euler-Bernoulli slender beam equations, and the latter is defined by a simple finite element analysis. To determine geometry, the properties of the material it is constructed from must also be known.

14.2.2 Material Selection

A search was conducted to find a material with a high strength to stiffness ratio, while not causing yielding to occur under small deformations. Nearly all metals were incompatible with these when fully stressed. Many plastics have an unacceptably low yield strength, making them also incompatible. Several compatible plastics in the search area were found, including several 3D printed materials. Prototypes were produced using the appropriate geometries and were tested. The 3D printed plastics were found to be too brittle, and their allowable deformations to be too small. All of the prototypes eventually fractured and failed catastrophically.

It was necessary to return to the original material search and select for materials with very high safety factors which fail ductilely. Now the concern was no longer ease of manufacture, so non-additively manufactured materials were considered. Ultem 1000 was selected as it met all of these factors, and can still be machined. New prototypes were manufactured and found to be superior to the 3d printed models, and more than adequate to implement.

14.3 Thermal Transfer Between HPU and Link Body

The original RTSX card cage systems used thermal paste to improve conduction between the heat spreader on the motor controller card and the link body. While it is possible to use thermal paste in this updated design, RTSX would benefit greatly operationally by abstaining from the use of any pastes or fluids. Several different connection methods were tested, including bare metal on metal, and a brass

coated thermal gap filler was selected. Details about this test can be found in the thermal testing section in [Section 16.2.1](#).

Chapter 15: RTSX Thermal Design Evaluation

In order for RTSX to operate in numerous environments, it must be able to output the heat generated by its servo drivers. Space manipulators typically expel their generated thermal energy by radiation, and by conducting heat back to the base vehicle [7]. RTSX will only be operating on land and in water now, so redesigning the thermal path to transfer heat directly into the surrounding fluid by free convection is a sensible solution.

15.1 Operating Environment

The operating environment for RTSX consists of three locations: laboratory, water, and on deck at the Neutral Buoyancy Research Facility (NBRF). Laboratory testing will be conducted in an air conditioned and dry short=sleeve environment, which will account for the bulk of Ranger’s use. In-water testing occurs fully submerged in a pool of chlorinated water kept at 30°C. A staging area, known as the “deck” of the NBRF is a temporary testing area for RTSX between water operations, which can reach temperatures of up to 44°C and 100% humidity.

Table 15.1: Thermal system design requirements

Geometric property of a sing servo driver's external surface area						Surface Area
Simplified cylindrical link without stiffening geometry						0.014
Final link geometry with isogrid						0.02
Environmental and operational conditions that the thermal solution must survive						Minimum Required Surface Area
Scenario Description	#	Q [watts]	T_{mc} [°C]	T_{inf} [°C]	H_{min} [W/m² °C]	[m²]
Wrist stall in laboratory	1	11	65	20	0.5	0.49
PXL stall in laboratory	2	27	70	20	0.5	1.08
Wrist stall in water	3	11	65	30	20	0.02
PXL Stall in water	4	27	70	30	20	0.03
Wrist stall on deck	5	11	65	44	0.5	1.05
PXL stall on deck	6	27	70	44	0.5	2.08

15.2 Design Challenges

The tray of the new RTSX link serves as both as primary structure and the only thermal path for the servo drivers. As was discussed earlier in this text, the geometry of the tray was optimized for structural stiffness with minimal mass, with only basic consideration given to thermal issues. Examining the outer surface of the tray, the isogrid paneling increases external surface area by 40%.

Table 15.1 above illustrates several issues with the base design. The values for free convection were taken from [8], and represent the approximate minimum value for natural convection in that respective medium. Operation of DXE and PXL in the water is roughly in the acceptable range; tests will need to be conducted to demonstrate that this is acceptable. Operation on deck or in the laboratory appears to fall at least one order of magnitude short of the acceptable range for free convection. By the data above, the surface area of the link would need to be

increased by more than a factor of 100 to be within acceptable operating conditions for scenario #6.

15.3 Thermal Design Solutions

Several options were considered to increase the rate of thermal transfer between the link body and the environment. Two active and two passive options were considered: active cooling, solid state heat pumps, bolt-on heatsinks, and built-in heatsinks respectively. The goal was to produce a design that can be physically implemented on RTSX with low mass and preferably low cost.

15.3.1 Built-In Heatsink

Possibly the simplest solution would be to added additional features, such as fins or pin heatsink geometry into the outside of the tray. No additional components would be added and, as the geometry of the tray already requires a four axis CNC to create, adding additional surface features is arguably simple. After some preliminary design, this concept was found to require fin geometry that is too small for normal milling. A built-in heatsink is not possible at this power density and free convection coefficient.

15.3.2 Bolt-On Heatsink

A bolt on heatsink would be able to conduct thermal energy to a much larger surface area to then be dissipated into the environment. The addition of a bolt on

heatsink was found to be viable, with several possible solutions. This solution necessitates two costly but critical design features: mating geometry to the base of the external isogrid to conduct heat into the heatsink, and finned geometry to increase surface area to the environment. After a review of options with manufacturing, it was found that machining finned geometry was prohibitively expensive. Pursuing other methods, two options were found: to create a monolithic part containing both features using additive manufacturing, or to machine the isogrid adapter and bolt on an off-the-shelf heatsink. The former option is effective and compact, but is far more costly than the latter. Designs for both were created and judged against the other solutions.

15.3.3 Thermal Electric Cooler

By increasing the operating temperature of the external surface, the surface area would not need to be modified. The operating temperature required to extract the thermal energy through free convection is prohibitively high, nearing 1400°C . In this regime, thermal transfer by radiation dominates, stabilizing at around 185°C . While more manageable, this is still too high for both human safety and is beyond the operational temperatures for thermal electric coolers. It is not possible to implement thermal electric coolers on RTSX.

15.3.4 Active Cooling

The only environments of operational concern are in air, which allows the consideration of powered cooling. Forced air convection has the possibility to increase the convection coefficient from 0.5 to 200 $W/m^2 \text{ } ^\circ C$ or higher, though it is highly dependent on fluid flow. The isogrid surface is a challenging structure to remove heat from through forced air convection, as the pocketed structure will create regions of high pressure but stagnant flow inside of them. With this in mind, ducted flow paths are a necessity. After some review, impinged nozzle flow was found to be a practical solution with the possibility of high convection coefficients, while remaining simple to calculate. This design was compared to the only other possible option, the bolt-on heatsink. As the bolt-on heatsink required a number of thermal connections and was a great deal more massive, the active cooling solution was selected for prototyping and testing.

15.4 Impinged Nozzle Flow Design

Cooling the bottom of a milled pocket with convective airflow is challenging. Without properly shaped airflow, the closed shape of the pocket can stagnate. As computation of flow across a non-planar surface can be complex, a solution that only cools with flow against the bottom of the pocket feature, rather than the sides, greatly simplifies calculation and design. Impinged nozzle flow forces airflow normal to a planar surface to transfer heat effectively by creating a turbulent region of airflow known as the impingement region. Compared with flow parallel across

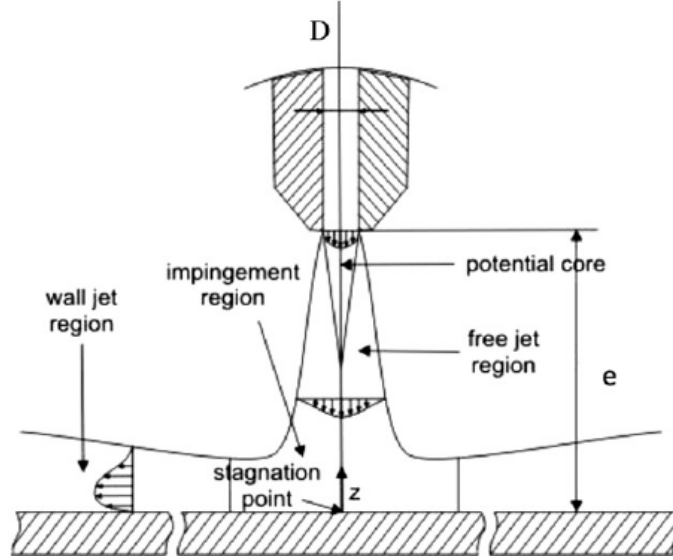


Figure 15.1: Diagram of impinged flow across a surface [9]

a surface, the turbulent region of impinged flow allows for high thermal transfer across a small area. This method of cooling also has the benefit of being simple to calculate numerically.

As the following calculations are done for air starting at standard temperature and pressure (STP), the following constants will be used.

Table 15.2: Table of constants used in the impinged flow calculation

Symbol	Name	Value	Units
ν	Dynamic Viscosity	1.589×10^{-5}	m^2/s
Pr	Prantel Number	0.707	Unitless
ρ	Density	1.3947	kg/m^3
κ	Kinematic Viscosity	2.63×10^{-2}	$W/m^\circ K$

Effective area (equation 15.4) is a dimensionless ratio between the diameter of the nozzle (D) and the radius of the impinged region (r).

$$A_r = \frac{D^2}{4r^2} \quad (15.1)$$

The Reynolds Number (equation 15.4) is calculated as follows, where ν is the dynamic viscosity for the fluid.

$$R_e = \frac{V_e D}{\nu} \quad (15.2)$$

The Grashof number (equation 15.4) is the dimensionless ratio between buoyant and viscous forces in a fluid, where H is the height of the nozzle opening above the surface.

$$G_r = 2\sqrt{A_r} \frac{1 - 2.2\sqrt{(A_r)}}{1 + 0.2\left(\frac{H}{D} - 6\right)\sqrt{(A_r)}} \quad (15.3)$$

The thermal convection coefficient (equation 15.4) generated in the impinged flow region is then calculated as follows. The Prandtl number and κ are empirical values specific to the working fluid, they are listed in table 15.2.

$$h = \frac{P_r^{0.42} \kappa}{D} G_r (2R_e^{0.5} (1 + 0.005R_e^{0.55})^{0.5}) \quad (15.4)$$

As stated by [9], the calculations for impinged flow cooling are only valid for the following regions.

1. Reynolds number between 2000 and 400000
2. Nozzle exit velocity below Mach 0.3
3. An effective area between 0.004 and 0.04
4. Nozzle height to nozzle diameter ratios between 2 and 12

Using the prior equations and bounds, the convection coefficient can be calculated given nozzle geometry and exit velocity. A relation between nozzle geometry and exit velocity (equation 15.4) must be formed to create a design space. By assuming that air passes from the environment, into a compressor, and then into a stagnant plenum from which the nozzles are fed, exit velocity can be calculated as a function of plenum pressure.

$$V_e = \sqrt{\frac{2P}{\rho}} \quad (15.5)$$

Nozzle diameter is governed by the operating limits of the compressor used to pressurize the plenum. A compressor has a nearly linear relationship between volumetric flow rate (equation 15.4) and operating pressure. The pressure and volumetric flow equation for a pump can be simplified by observing volumetric free flow, flow at maximum pressure, and maximum pressure.

Using this relation, a market survey was performed analyzing a wide range of fans and compressors. The surface area directly external to the servo driver

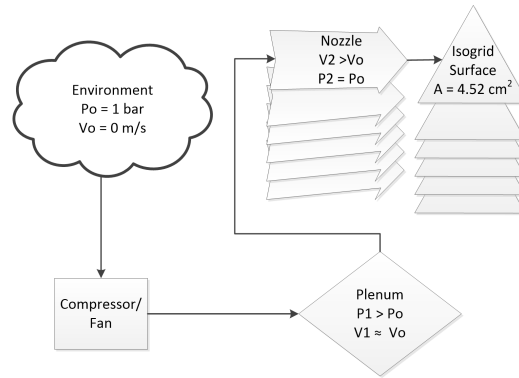


Figure 15.2: Diagram of flow in the cooler

$$\dot{Q} = \frac{P}{P_{max}}(Q_{open} - Q_{closed}) \quad (15.6)$$

features a set of twelve full isogrid pockets. Using one nozzle per each of the pockets yielded the best total heat transfer from the servo driver. A search was conducted considering packaging, thermal transfer, mass, and decibel level. The initial study attempted to use a single compressor to cool all three HPUs in the links considered, but the commercially available options were too large to package easily and ducting was found to be too complex to quickly design. Diaphragm pumps were initially considered to be the optimal pump for this design, but the survey found that the permissible flow rate and pressure fall outside of the acceptable design space for impinged flow.

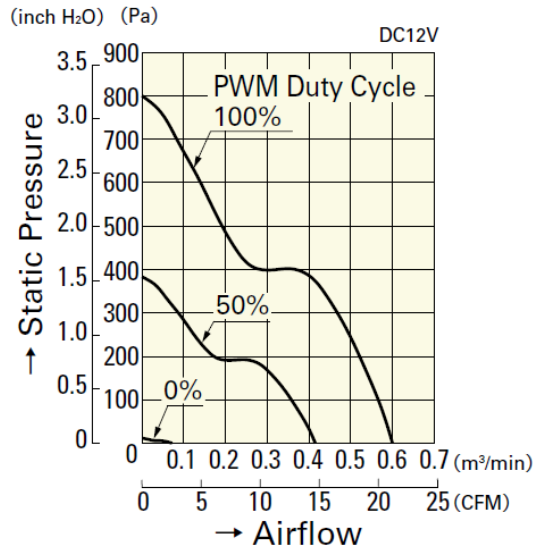


Figure 15.3: Pressure-velocity diagram for the selected fan [10]

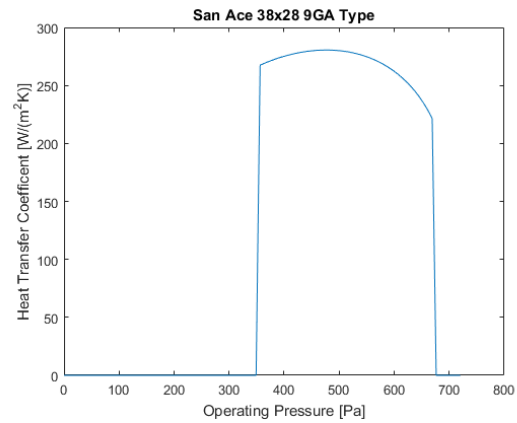


Figure 15.4: Calculated ideal impinged flow cooling per motor controller

The market survey yielded multiple acceptable fans. The selected high static pressure fan has a useful operating pressure for nearly half of its operating regime.

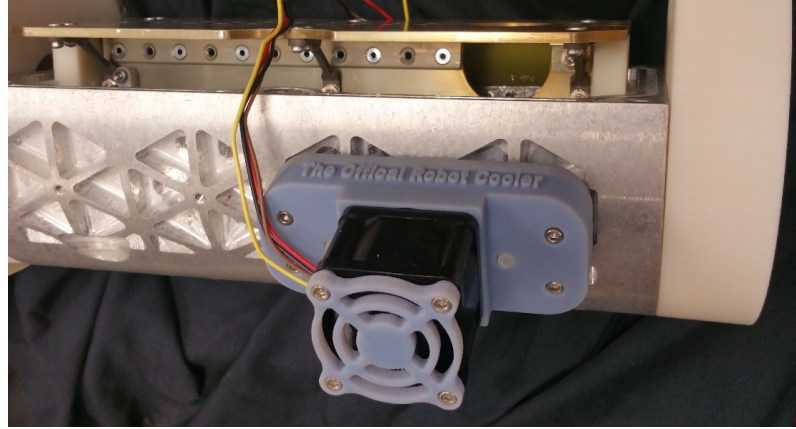


Figure 15.5: Cooler assembled onto the thermal testbed

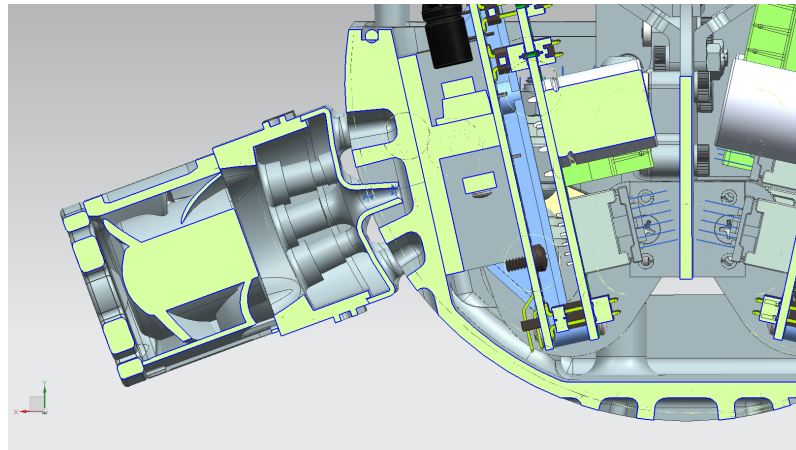


Figure 15.6: Cross sectional view of the cooler as applied to a link

Unfortunately RTSX only has two power buses, 48v and 5v, so the selected fans will require some form of voltage regulator to operate. Each prototype fan was equipped with its own buck-boost converter packaged into the plenum area directly under the flow of the fan.

15.5 Fabrication

The structure for each cooler module was fabricated using Multi Jet Manufacturing¹ (MJM) in a matter of hours. To reduce manufacturing time and support material volume, the plenum was bisected at its mid-plane and assembled using bolts. The plenum was constructed from RGD840 on a Stratasys Objet30. The print area and orientation of the design was manipulated to reduce print time as the printing process is very sensitive to certain features, such as object height and cavity orientation. The full list of optimizing practices can be found in the Objet30 Users Guide [11]. These rules dictated many of the small design choices in the shape of the plenum/nozzles.

While the MJM process is well suited for this design because of its speed and geometry, the material used proved to be problematic. RGD840 has a heat deflection temperature (HDT) of 45-50°C at 0.45 and 1.82 MPa. While the operating environment does not extend exceed 44°C (Table 15.1), the close vicinity of the HDT caused warping to occur over time. This opened the seam between the bisected components, venting the pressure of the plenum to ambient. As a design revision, the plenum should be constructed from a material with a higher HDT to prevent further issues.

Attachment to the isogrid of the link was done using nylon 4-40 bolts. This mounting requirement is strictly enforced to prevent damage to the link body. In the event of an unexpected failure or collision, the attached bolts will be sheared off

¹Also known as polyjet manufacturing

rather than damaging the aluminum housing. Two threaded features are located by each servo driver and are used to secure each cooling unit. To stabilize this design, four hemispherical contact points are included in the geometry for the plenum. As the fasteners are tightened, these points are pre-loaded against the exterior of the link to eliminate vibration.

Chapter 16: Thermal Verification and Testing

To verify the thermal design and to refine uncertain design features, a series of experiments were conducted, using a mixture of mock-up and final hardware to reduce testing costs.

16.1 Test Hardware

A prototype test link was created to validate the design of the thermal system in RTSX and the values in Table 15.1. The prototype link consists of a tray and electronics rack with dummy servo drivers designed to emulate the thermal load from a stalled servo driver. To eliminate unknown or unpredictable components of thermal transfer, all other exterior components were created using ABS plastic. Free convection can be greatly influenced by the orientation of the geometry, as it is dependent on buoyant forces. For that reason a two degree of freedom poseable joint was designed and placed between the test link and its stand, allowing the cylindrical link to be placed into any orientation.

The test electronics rack features three dummy servo drivers and five thermal probes. Four additional thermal probes were placed about the test tray. This array of sensors was designed to measure maximum temperatures about the system

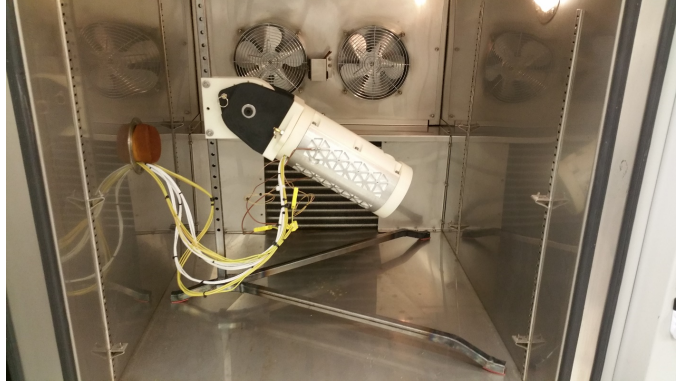


Figure 16.1: Thermal test link in an environmental chamber

as well as the resistance across thermal junctions and free convection coefficients. Each dummy servo driver can be heated in two different zones, up to 50 watts per zone. The servo drivers these are approximating have multiple MOSFETs across their heatsink which are individually activated based on motor commutation, so two zones were made to examine the possibility of MOSFET location dependent heating.

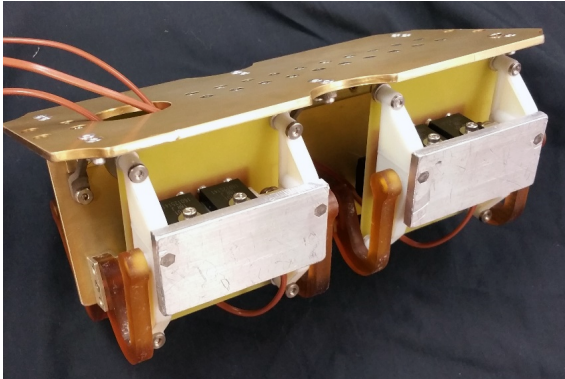


Figure 16.2: Test electronics rack with dummy servo drivers

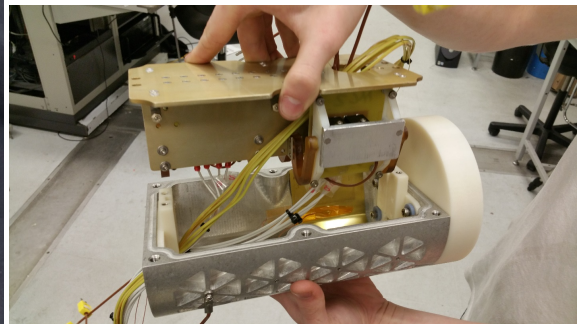


Figure 16.3: Thermal test platform being assembled

One mock HPU was sensed in greater detail than the others, to observe phenomena inside of the HPU. In Figure 16.5, the location of sensor 1 is common across

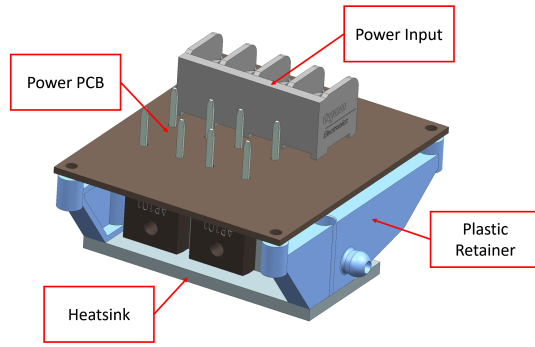


Figure 16.4: Rendered graphic of the mock HPU

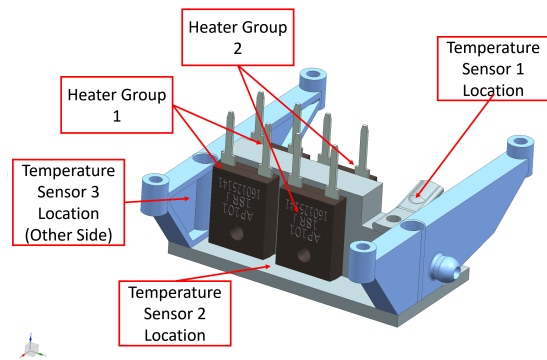


Figure 16.5: Rendering of the interior of a HPU with sensor locations labeled

all three mock HPUs and is located approximately where the built in thermistor is on the servo drivers. This will provide a more accurate estimate as to when the servo drivers will enter an over temperature state. Sensor 2 is located at the closest point between the heater units and the outside wall, providing the temperature just before heat is transferred to the outside wall. Sensor 3 is located on the outer plastic wall to study internal radiation. How this functions is explained later in this chapter.

Four resistive heaters are located on the heat sink, pictured in Figure 16.5, and grouped into two pairs. The motor controllers these are imitating have six separate MOSFETs spaced across the length of the heatsink, which are activated in pairs. This mock grouping is to verify that the variation in thermal loading location across the heatsink does not impact the performance of the unit. Thermal load is established by measuring total electrical power input to each heater group to produce accurate measurements.

16.2 Thermal Testing Results

The thermal test was conducted to study a range of attributes. In total, approximately 100 hours of testing was performed on this system in a wide variety of configurations. For all test procedures, steady state conditions are assumed to have been achieved when the change in temperature is less than $0.01^{\circ}\text{C}/\text{min}$. Monitoring mechanisms were used to make sure that temperatures did not exceed acceptable limits to prevent damage to the test hardware.

16.2.1 Junction Resistance

Thermal resistance was studied across the thermal junction between the servo driver heatsink and the link body. Several options were considered at the start of this experiment for this thermal junction as it provides a unique challenge: a sliding thermal junction. As mentioned earlier, thermal paste was used in the original VPX rack for Ranger. While this is effective, it leads to operational challenges when the paste needs to be cleaned and reapplied after de-mating to ensure proper contact. The prototype housing manufactured to test the side loading design did not make use of any thermal joining compound, merely placing two relatively flat aluminum plates against each other. While this was permissible for the simple kinematic checkouts that DXE was subjected to, it was insufficient for operation near the load limit of the arm and overheated in those conditions. Junction resistance was never characterized for the prototype system, but was deemed unacceptable and it was noted that thermal conductivity would need to be improved on the final design.

The thermal test link was used as a test platform to evaluate thermal junction designs. Three baseline designs were tested: bare metal, thermal paste, and a gap filler. The gap filler selection was investigated with the cooperation of the manufacturer. Off-the-shelf foamed gap filler has a very high coefficient of friction, practically adhering to any clean surface. This is incompatible with the assembly method used to contact the HPUs to the outer walls. During assembly, the HPU must slide across the surface while the retaining arm is pre-loaded. Gap filler would bind and tear during this assembly. Ultimately, a thin brass coating on the gap filler was found to have little impact on the materials thermal performance, while allowing the HPU to slide across the now brass coated surface during assembly.

Table 16.1: Experimental results for various thermal interface models

	Bare Metal	Thermal Paste	Brass Coated Gap Filler
ΔT [°C]	32.8	12	13.8
Junction Resistance [°C/W]	1.27	0.466	0.536

The results of the thermal junction test are shown in Table 13.1. During testing it was found that the bare metal junction resistance, approximately 1.27 K/W, was too high to allow any HPU to operate at capacity for more than a few minutes. However, both the thermal paste and gap filler had acceptable performances. Although it is possible to gain a slightly better thermal connection by the use of thermal paste, the brass coated gap filler is far easier to work with. This junction method is now used for every HPU connection in the system.

16.2.2 First Order Calculation of Steady State Values

It was theorized that during testing, it is possible to predict the steady state temperature of the system from a set of initial values. This method was derived assuming that the heating system acted like an ideal first order system. This assumes the system can be modeled as having a linear dissipation rate of energy to the environment, a constant rate of energy input, and a linear heat capacity. Given that, when the system is at ambient temperature and the heat is turned on, the temperature rise will act as Heavyside step function with arbitrary inputs. This can be modeled as follows where $h(x)$ is the Heavyside step function.

Experimental data is gathered in the time domain. It is thus useful to have a final form using a time constant to make its form easily understandable. Manipulating equation 16.2.2 to use time constants yields equation 16.2.2.

$$\frac{dT}{dt} + \frac{1}{\tau}T = Ah(t) \quad (16.1)$$

$$T(t) = T_0e^{\frac{-t}{\tau}} + A\tau(1 - e^{\frac{-t}{\tau}}) \quad (16.2)$$

In this form, T_0 is the initial system temperature, A is a scalar, and τ is the time constant of the system. This is a very useful form, as A/τ is also our steady state temperature, which will be denoted as T_{ss} from now on. Given that there are three unknown variables in this equation, the system should be able to be characterized by fitting the curve to a series of three data points.

A 6 hour test was conducted to gather data to verify this model. The first

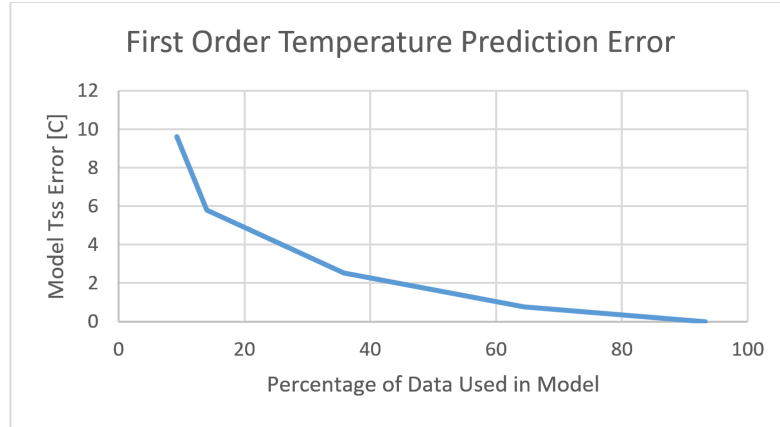


Figure 16.6: First order temeperature prediction error

order model was applied to a set of linearly spaced data points taken from the experimental results. As was expected, when the sampled data increases in size the steady state error decreases. Depending on the accuracy of T_{ss} desired, this model may be useful for reducing testing time by 60% or more.

Multiple attempts were made to create a more accurate predictive model. Possible sources of deviation examined were increases in ambient temperature, unequal heating rates of the bulk materials, and radiative thermal dissipation. Increasing the system order and adding additional linear terms had limited success in consistently lowering the prediction error. Ultimately this prediction method was abandoned for collecting experimental data as the repeatable accuracy was deemed unacceptable.

This method was used extensively during the testing process, but not for any gathered data. This was used as a safety check, in addition to finite element models predicting the steady state temperature of the experiment. To prevent potential damage of the hardware, the steady state error was continuously predicted using the data gathered. When an egregious overshoot of the maximum temperature was

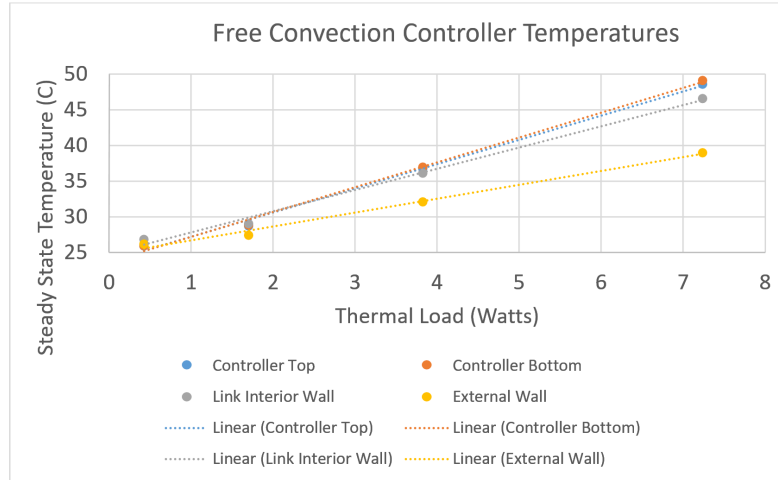


Figure 16.7: Free convection experimental results at room temperature

predicted, the experiment was carefully monitored until the predicted steady state error returned to acceptable ranges or was shut down.

16.2.3 Passive Convection Performance

The majority of the testing conducted was to observe the free convection based cooling of a link. Free convection performance was limited by the maximum operating temperature of the motor controller. The test was concluded when the steady state motor controller temperature exceeded 50 degrees Centigrade. The test was operated at 22 degrees ambient temperature and the maximum operating thermal load was 7.25 watts. Detailed results can be found in figure 16.7. It was found that the average free convection coefficient is approximately 14 W/m-K.

It was predicted that the orientation of the link with relation to gravity would have a large effect on the cooling rate of the link. However, after some experimentation it was found that in practice this had a 10% impact on the total performance of

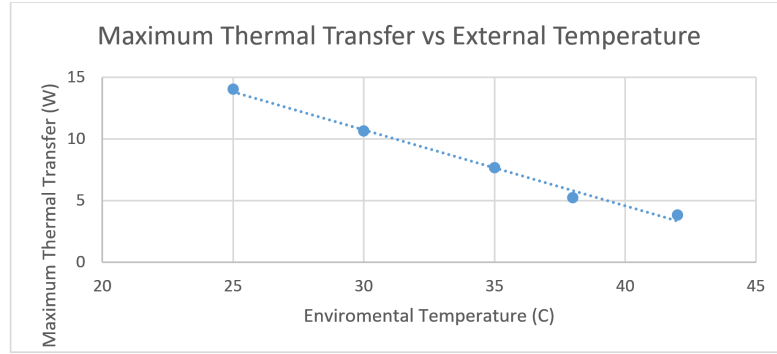


Figure 16.8: Maximum disipation from each motor controller as a funciton of external temperature

the system. When the axis of the link was oriented vertically, the convective cooling had a higher impact. This follows with free convection theory, as the buoyant forces are able to increase the velocity of the fluid across the surface of the link body. All other tests were performed horizontally to create a worst case heating scenario.

16.2.4 Forced Air Convection Performance

Actively cooling the structure of the link provides a generous boost in performance. After a few tests, it was determined that the cooling performance of the impinged nozzle design greatly exceeded the capacity of the motor controller. It averaged a surface dissipation of 50 W/m-K, more than 3.5 times greater than free convection cooling. This accounts for the total surface area fraction that the heatsink can dissipate heat through, not just the bottom of the Isogrid as calculated in Figure 15.4, which account for the perceived 5 times reduction in performance from the simulated forced cooling design.

Cooling the motor controller below 50C is not a useful metric for normal operation. The forced air convection performance was measured by holding the

motor controller at 50C, using the environmental temperature as the independent variable, and the thermal power emitted from the motor controller as the dependent variable.

16.2.5 Internal Radiative Heating

To prevent damage to the selective laser sintered (SLS) plastic holddown points on the motor controller, it is important to study the internal heating effects, not just the stable system temperatures.

The location of the resistive heater on the mock motor controllers was observed to have a direct effect on the heating rate of the holddown points. When the heater closest to the holddown point was activated (heater group 1 in Figure 16.5), the plastic surface drastically rose in temperature despite the isolating air gap. Sensors placed across the motor controller heatsink showed that there was little variation in the heatsink temperature gradient based on which heater set was activated. If this phenomena presented a greater change in temperature it would be of concern. However, as the materials used in this design are all capable of surviving the temperatures presented, this phenomena should merely be noted for when observing temperatures inside the final design.

16.3 Thermal Design Conclusions

The thermal design and analysis of Ranger resulted in a functional design that can be used in a neutral buoyancy environment. However, the design required

several special considerations to be made when operating on land. An active cooling device had to be constructed to produce acceptable operating temperatures while on land. The thermal design of RTSX is functional, but should be iterated again to see if there is a possible design that works in all required environments without modification.

Chapter 17: Internal Electronics Mounting

Mounting electronics inside of a flexible body is a non-trivial process. As discussed earlier in this paper, flexure of printed circuit boards and electronic components can have catastrophic consequences. In a typical design, a printed circuit board should be kept as rigid as possible to avoid any problems, which sits in opposition to the assumption that the link body is flexible. The following section details the design process for mounting the electronics internal to the link body of RTSX.

The overarching design concept for this refit is to sequester all electronic components in the link to a removable rack to facilitate repair and upgrades. After multiple design iterations of the rack with the electrical engineers for RTSX, it became clear that it is more efficient to set known interfaces between hardware and electronics at the expense of design flexibility. For that reason, the layout of electronics in the rack was separated into discrete regions.

Packaging of the HPUs into the wedge configuration only allows for a few regions in the cross section for continuous structure along the length of the link. As the allowed volumes for the HPUs are very well known, the design volume for all additional electronics to be housed must be maximized. After several design revisions, a minimum “accessory electronics allotment” was created. This was the

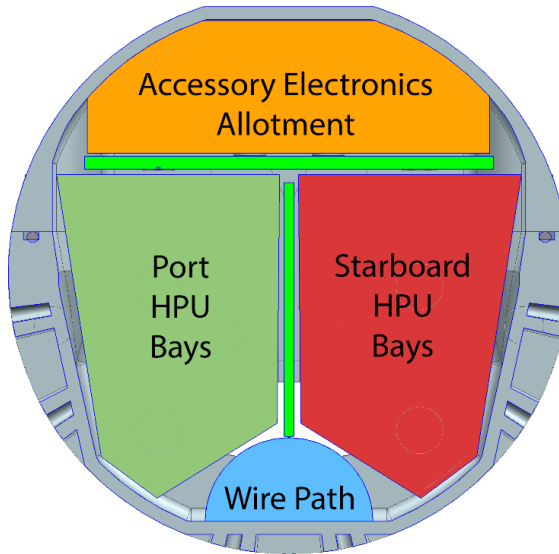


Figure 17.1: Cross section of the link depicting volume allotments

driving factor in determining the maximum thickness of the top plate, which could be no thicker than 0.125 inches.

17.1 Rack Construction Concepts

The electronics rack must be structured to hold all components securely and with adequate stiffness. The design must also be within the allowed budget to construct. Due to the complexity of the required geometry, multiple concepts were tested to find an affordable design.

17.1.1 Externally Framed Rack

Placing the bulk of the structure for the rack about the external perimeter certainly has its benefits. With a large separation between the mounting plates, the structure is very resistant to bending. It also affords an additional layer of protection

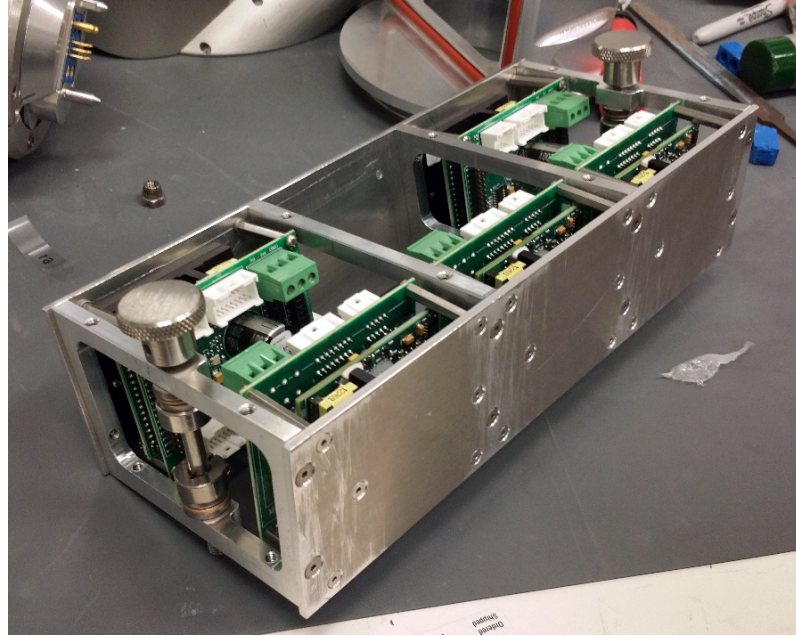


Figure 17.2: Prototype electronics mounting rack demonstrating an externally framed rack concept

for the electronics contained within. The design in Figure 68 uses a series of thin beams to separate the two mounting plates. As the plates are compressed together during insertion into the link, these beams act as high stiffness springs. They are designed to buckle when compressed to apply a firm contact between the mounting plates and the body of the link for thermal transfer.

This design was used in the original prototype link. Multiple issues were found with the implementation of this design. The rack design is fairly massive, and should be mass optimized on future iterations. The contact area between the mounting plates and the link structure is extensive, but does not contact evenly, resulting in poor thermal transfer. The clamping method is not statically determinant, making the vibrational properties of the cage unknown, even varying between assembly/disassembly cycles.

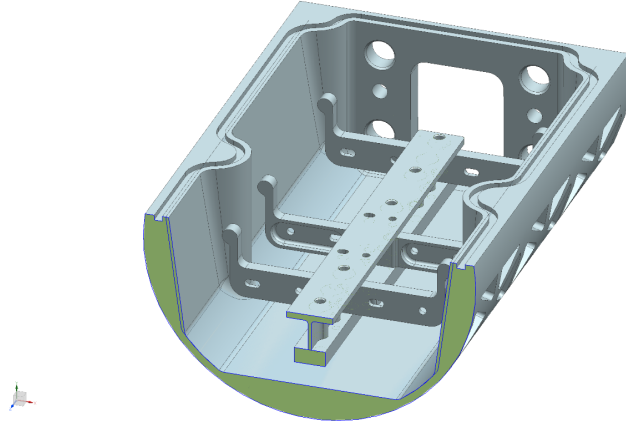


Figure 17.3: Internally framed rack with an underslung structure

17.1.2 Monolithic Internally Framed Rack

For completeness in the design space, we must entertain the idea of machining the rack from a single monolithic piece of stock. This has the benefit of eliminating all structural fasteners and can allow an overall lighter structure. However, given the complexity of the geometry inside the design volume, the complexity of machining and its associated costs will greatly outweigh any performance benefit.

17.1.3 Built-Up Internally Framed Rack

Two layouts were pursued for an endoskeleton-style rack. Early design exploration created the concept of the cantilever retaining arms, which are detailed in chapter 14. However, the structure that mounts all of the retaining arms together takes on a variety of shapes. The structure can fill the entire volume, but it was limited to either above or below the HPUs.

$$E = \frac{4FL^3}{(\Delta y)bt^3}$$

Figure 17.4: Required Young's Modulus for a given deflection

$$f_n = \sqrt[4]{\frac{3EI}{ml^3}} \sqrt[2]{2\pi}$$

Figure 17.5: Natural frequency of a massless cantilever beam with a tip mass

17.2 Structural Analysis

It is assumed that the mass of electronics on the top plate is approximately 2 kg and the vibrational loading on the link will not exceed 5Gs. Based on these estimations, the maximum loading across the face of the top plate is approximately 100N. Packaging provides limiting geometry for the design of the top plate. The plate will be 208mm by 111mm to give the most amount of useful surface area to the electronics team. The plate has a maximum thickness of 3.2mm and a maximum allowed deflection of 1.2mm. Given these constraints, the required stiffness of the plate can be calculated by modeling it as a cantilevered beam.

The required Young's Modulus for the top plate to prevent static deflection based collisions is an order of magnitude less than the Young's Modulus for aluminum. Since static deflection is of no concern, we must examine the fundamental frequencies of the rack.

Initial analysis yields a harmonic frequency of the electronics rack of approximately 6 Hz. As the expected harmonic frequency of the arm is below 10 Hz, this would be unacceptable. However, if the top plate is manufactured from high modulus carbon fiber, the harmonic frequency of the rack becomes 45 Hz. As construction

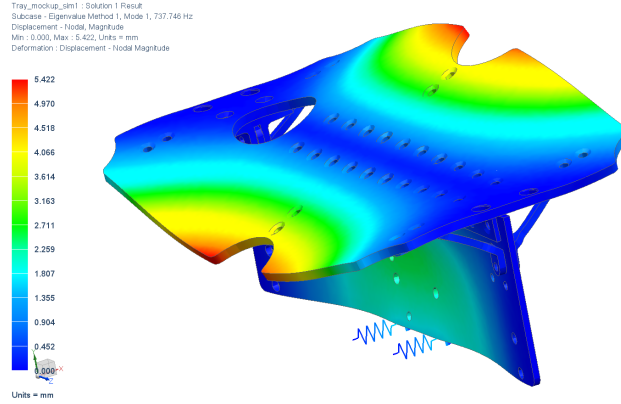


Figure 17.6: Finite element simulation showing the first vibratory mode

with carbon composites can be costly, alternates must be considered. By adding several stiffening struts across the body between HPU bays, the first harmonic node is eliminated. This structure becomes far more difficult to calculate analytically with the addition of the struts, so instead finite methods are used. A mesh model was generated from the existing geometry and a set of idealized springs were added in place of the HPU spring arms. Vibratory analysis was performed using NASTRAN SOL 103, Real Eigenvalues, to find the un-damped fundamental frequencies of the whole system. This analysis revealed that the first harmonic frequency of the rack is increased to approximately 700 Hz.

The stiffening struts are a critical component of the rack body, and are a good candidate to optimize for manufacture. Initial assessment of manufacturing techniques rules out the use of low scale sheet metal forming as too inaccurate and of subtractive milling as too costly. Instead, additive manufacturing methods were considered.

Multiple geometry options such as the design above were considered. These designs were optimized using the manufacturer's costing function using several dif-



Figure 17.7: Concept for a stiffening beam for the top plate



Figure 17.8: Final stiffening beam design, tessellated to reduce manufacturing cost

ferent starting designs, such as the multi-node truss pictured above. Ultimately it was found that the costing function was most effective if the design can be tessellated into the smallest build area per strut. The final design was created considering Euler buckling and the potential for manufacturing defects, leading to a simple geometry that is thicker than normally required.

The shear clips used to retain the top plate to the vertical plate in the electronics rack design were limited by machining requirements. To eliminate as many vibrational nodes as possible, the shear clips were attached through the contiguous length of the vertical plate. The rivets used to affix the plates to the shear clips are double-countersunk, designed to sit flush on both sides of the material, to prevent any damage to the wiring harness that will be occupying the same area. This type of rivet is a new design is relatively new, so a large safety factor must be used to avoid any unexpected failures. To prevent any corrosion between the aluminum of the rack and any of the fasteners used to hold it together, the aluminum components

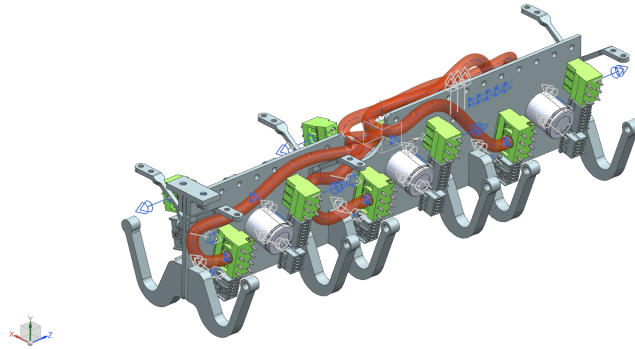


Figure 17.9: Wiring harness path generated in NX for the power cabling for the servo drives

were individually Alodined¹ to provide a wear resistant oxide layer which electrically insulates the fasteners from the structure.

17.3 Wire Harnessing Consideration

Allotments must be made for wiring harness paths in the design of the electronics rack. To calculate the cable harness diameter, a series of interface documents were created for each electronic module. An example page taken from this document can be found in appendix E. Paths were then generated in NX, using these documents to generate approximate cable harness diameters.

As can be seen in figure 17.9, the wiring harness for the motor controllers passes between the stiffening rib and the tray body. This method makes good use of the space, but required multiple design considerations to prevent abrasion of the cable harness. All corners in this area are curved to prevent abrasion, including the stock used to create the shear clips used to assemble the tray.

¹Also known as yellow chromate, a conversion coating applied to the surface of metals to inhibit oxidation.

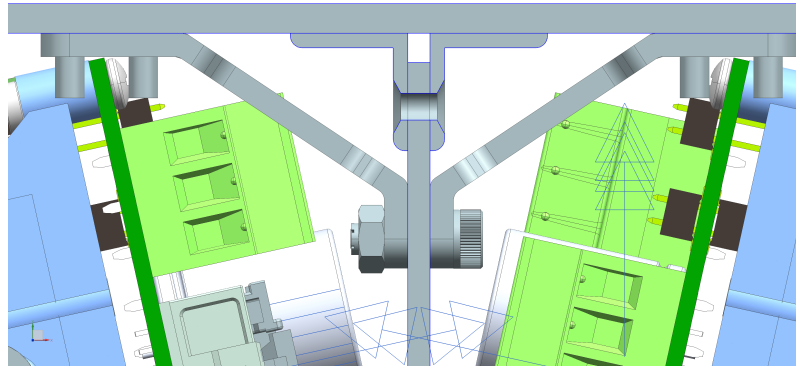


Figure 17.10: Gap in the built-up structure used for harnessing

The double-countersunk rivets have a fairly small range of acceptable plate thicknesses. Compounding that with the need for building up the joint with two shear clips and the tolerances for countersinking holes (figure 17.10), the required precision for constructing this section becomes very strict. This increases the cost of the shear clips greatly, but is an allowable trade off for the gained harnessing volume.

17.4 Parallel Design Development with Electronics Designs

One of the major challenges in designing the upgrades for RTSX were the parallel development of electrical and mechanical design. Multiple methods for coordinating this design process were tried with varying degrees of success. While current detail designs could be conveyed with relative ease, design intent is frequently lost. The use of Interface Control Documents, colloquially known as ICDs, was found to be the most effective in retaining design intent and establishing design requirements. This frequently took the form of allowed design volumes, mounting

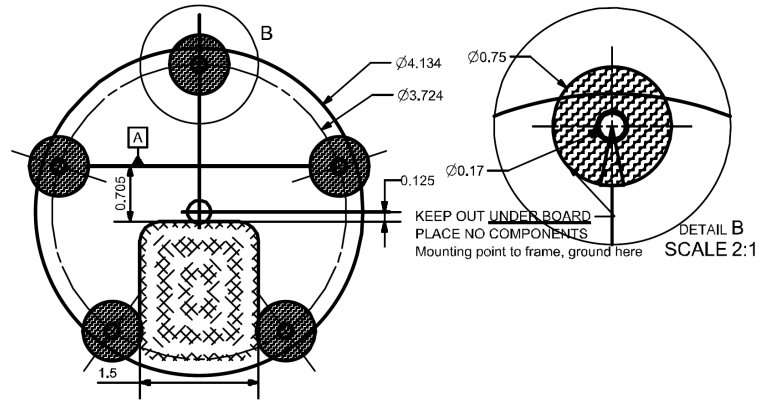


Figure 17.11: Subsection of the mechanical ICD issued for the status indicator housing

regions and methods, as well as enforced keep-out zones. Expanding ICD constraints to be as overreaching as possible was useful for design iteration, reserving extra area as a system level allowance.

17.5 Electronics Mounting Conclusions

Building up an internal mounting rack in this manner allows for a wide variety of mounting options for electronics. The concept behind this design was to maximize internal mounting volume while still retaining good heat sinking and rigid structures. While this has been shown to be true in the preceding sections, such a design is not inherently easy to manufacture. Cable harnessing is a non-trivial task for such a design. Although it was shown to be possible in Section 17.3, there is little margin for error in creating such a harness. Given the design constraints of this system, there is little alternate for this design. Implementing a floating connector between all of the electronics and the rest of the system reduces the manual labor executed on the manipulator itself during maintenance, but also increases cost and part count.

In all, this design works appropriately and no design defects have yet to be found, but designing for such a large bulk of cabling inside a small housing is difficult.

Chapter 18: Link Extension Design

Up until this chapter, we have alluded to the existence of link extensions, a method by which the kinematics of RTSX can be modified. This chapter details both the mechanism for extension, as well as the governing equations for designing an extension link. Link extensions add to the existing link length. They range in extension from a few centimeters to multiple meters. Of course, the longer the link, the lower the allowable tip mass. For very long lengths, it is not possible to operate RTSX without a gravity offset, such as in neutral buoyancy or microgravity. We can extend the operability region of RTSX slightly by applying lightening techniques to minimize the material used in their construction.

18.1 Thin Walled Beam

A formula [12] for determining the buckling stress of a thin walled tube in bending was empirically derived by a team of NASA researchers to form equations for space vehicle design. The equations 18.1 and 18.1 defining the critical buckling stress are taken from that monograph.

$$\gamma = 1 - 0.731(1 - e^{-\frac{1}{16}\sqrt{\frac{r}{t}}}) \quad (18.1)$$

$$\sigma_B = \frac{\gamma E}{\sqrt{(3(1 - \nu^2))}} \frac{t}{r} \quad (18.2)$$

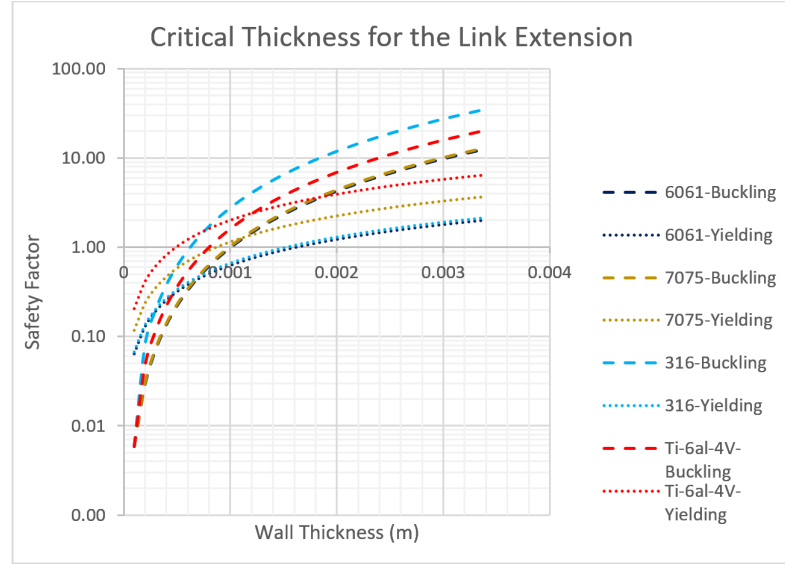


Figure 18.1: Critical thickness of the link extension given various material properties

Using equation 18.1 we can examine the design space to determine the wall geometry. Both yielding and buckling loads must be observed to establish a minimum wall thickness. Materials with a smaller modulus ratio¹ are more susceptible to failure by buckling than by yielding. This can be observed in figure 18.1.

Given these design limitations, aluminum 7075 was selected for the link. Although greater performance can be achieved using titanium, the added material and subsequent machining cost makes the design too expensive. Stainless steel is to be avoided for large structures, as its specific stiffness is too low to produce a tenable system mass. However if manufacturability is desired over performance, it is simpler to weld and form stainless steel; this would be a good alternate for producing extremely long link lengths.

¹The modulus ratio is termed here as E/σ_{yield} , the ratio of the Young's Modulus to the yielding stress

Table 18.1: Design limits of a 0.33m link extension

	Modulus Ratio	Safety Factor of 1			Safety Factor of 2			Stock Cost
Material	E/σ_{yield}	Defining Factor	Thickness (mm)	Mass (kg)	Defining Factor	Thickness (mm)	Mass (kg)	USD
6061	250	Yielding	1.7	0.65	Yielding	3.4	1.3	26
7075	143	Buckling	1	0.4	Yielding	1.8	0.71	55
316	666	Yielding	1.6	1.8	Yielding	3.2	3.62	125
Ti-6AL-4V	128	Buckling	0.8	0.5	Buckling	1.1	0.69	455

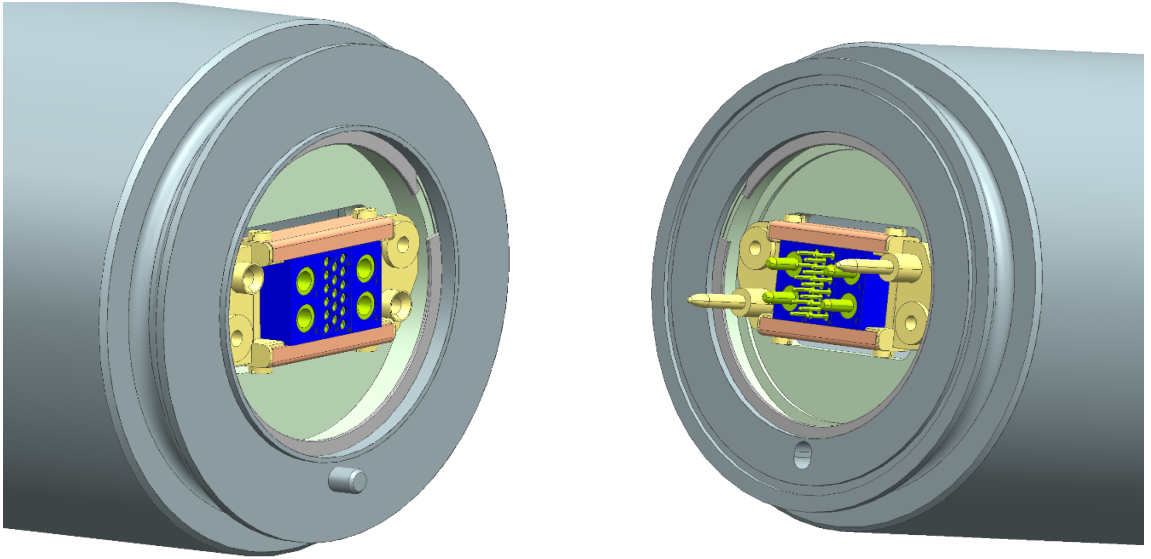


Figure 18.2: Proximal link extension inner- Figure 18.3: Distal link extension interface

18.2 Link Extension Interface

The link extension interface uses several features to align and transfer loads. These features are original to the first RTSX design, and have been reused to reduce the remanufacture of mating components. The inter-link connection is done with a marman clamp, which preloads the connection, and transfers bending and axial loads. A lip machined into the connection transfers shear loads across the joint, and works in combination with a pin to transfer torsional loads.

Internal to the mechanical interface are interconnects for the electrical system. RTSX uses three high power connector modules manufactured by Smith Connectors, known as Hypertronics connectors. These have the power density and the connection density required to pass the power and data busses through the links. The original design used a purpose built floating connector housing which aligned the connectors physically before mating. The new design standard has made use of a COTS floating connector housing manufactured by Smiths Connectors to house these modules. This makes manufacturing cheaper and tolerance simpler for the extension interface, eliminating the tight tolerance parts from the design.

The link extension interface geometry was retained in the redesign because it is effective and simple. However, the interface hardware was changed from stainless steel to hard anodized aluminum to reduce mass. There were many concerns for this interface originally. Galling and cold welding are a big concern for a high stress joint like this when operating in vacuum. However, as this joint will be operated terrestrially, and the chance of cold welding is highly reduced when aluminum is hard anodized, this design choice was deemed acceptable.

18.3 Link Extension Design

With the link extension wall thickness and the end interfaces established, the method of manufacture needed to be established. With such a thin outer wall and thick end features to be made, the possibility of welding the components had to be entertained. After a brief dimensional analysis looking at the shrinkage and

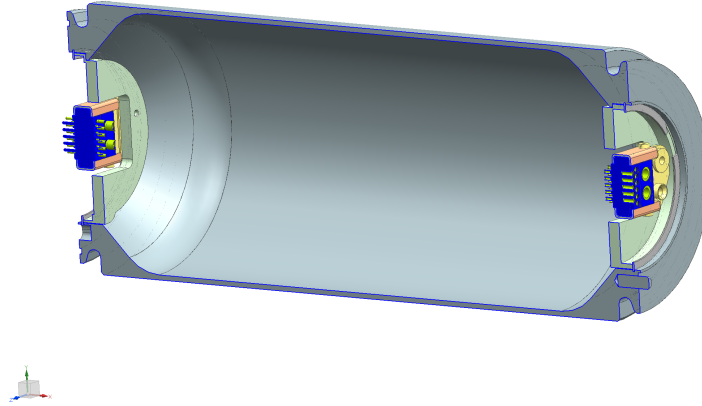


Figure 18.4: Cross section of the link extension assembly

warping due from welding process, this method was deemed unsuitable for a part of this scale, due to the inaccuracies in parallelism between the two end interfaces from welding. A built-up assembly was also considered; however, in a bid to reduce component count, this was not pursued.

The final assembly consists of a monolithic structure bored from a single piece of stock, with both the thin walled beam and the RTSX link extension interface integral. The connection to the floating connector assembly is made with a retaining ring and an alignment notch. This simplifies the manufacturing to two lathe setups and two milling setups. If this can be manufactured on a milling lathe then the setup is reduced to only two lathe positions. There is a challenge to boring a component this long, as a useful length for this link extension design is between 5 and 20 inches in length. A survey of several machine shops showed that while this is not commonly possible to manufacture, specialty lathes exist with a long enough bed to

manufacture this component.

This design for the link extension provides a nearly perfect stiffness to strength ratio using aluminum. Although it is theoretically possible to achieve a more optimum design by using more complex geometry, ie isogrids, the design selected sits nearly perfectly between yielding and shell buckling. Unfortunately this design is not scalable beyond about 15 inches for manufacturability reasons. For such an arm, using a built up design with a common extrusion is preferable. No such extrusion is commercially available, so a custom extrusion is a likely but costly alternative.

Chapter 19: Conclusions

The design of new electronics housings for RTSX transformed from a simple structure with complicated electronics to a complex structure with simple electronics. While the utility of altering the electronics in such a manner is beyond the scope of this paper, this new design is far more capable both electronically and mechanically. We have formed a much more comprehensive understanding on the interplay between electronics packaging and structural design. By taking a holistic approach to design, the new system has improved thermal performance, structural stiffness, and maintainability without the use of exotic materials or drastic changes to the manipulator's architecture.

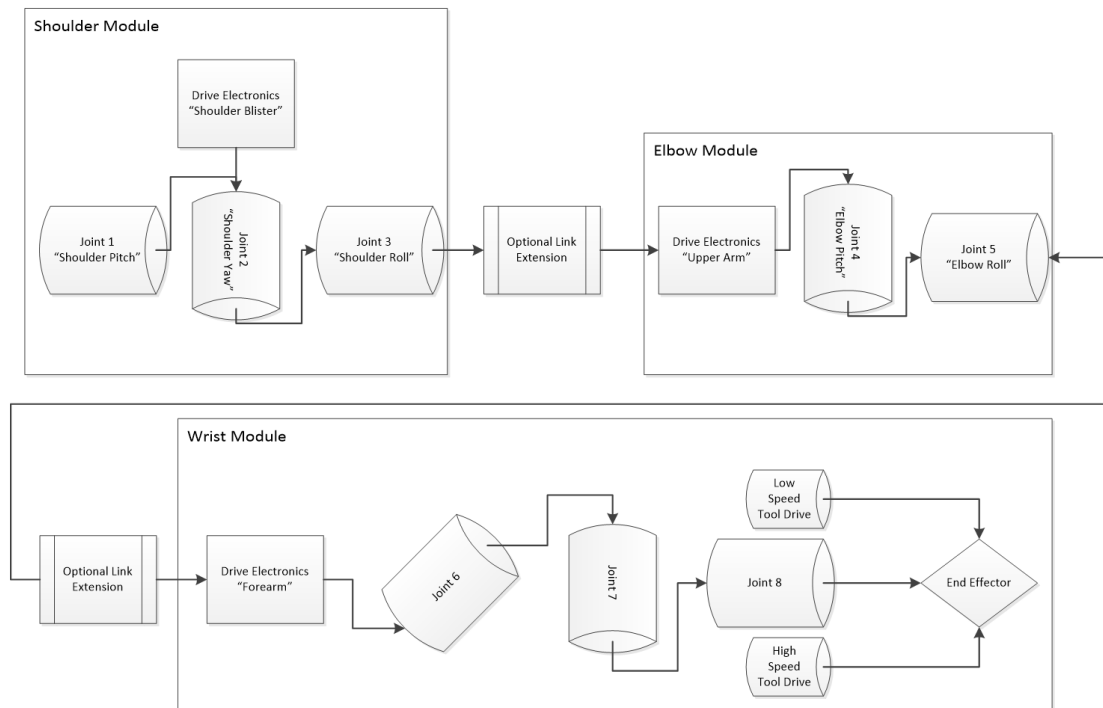
Many design guidelines were established in the production of this thesis. Minimum parent material geometry for a threaded feature is useful knowledge, however the real life performance of this method was never established as the feature was rendered unnecessary in the final design. The ultem hold down arms for the HPUs appear to be very effective, however the design will need to be proved with further testing, including vibratory and vacuum tests. The utility of forcing such a rigorous top-down method for this design has yet to be established. It is certainly effective for larger projects, but the size of this study borders on being too small to be

effective. As of the completion of this thesis, all of the design guidelines created appear to be of great value, but further testing will be required.

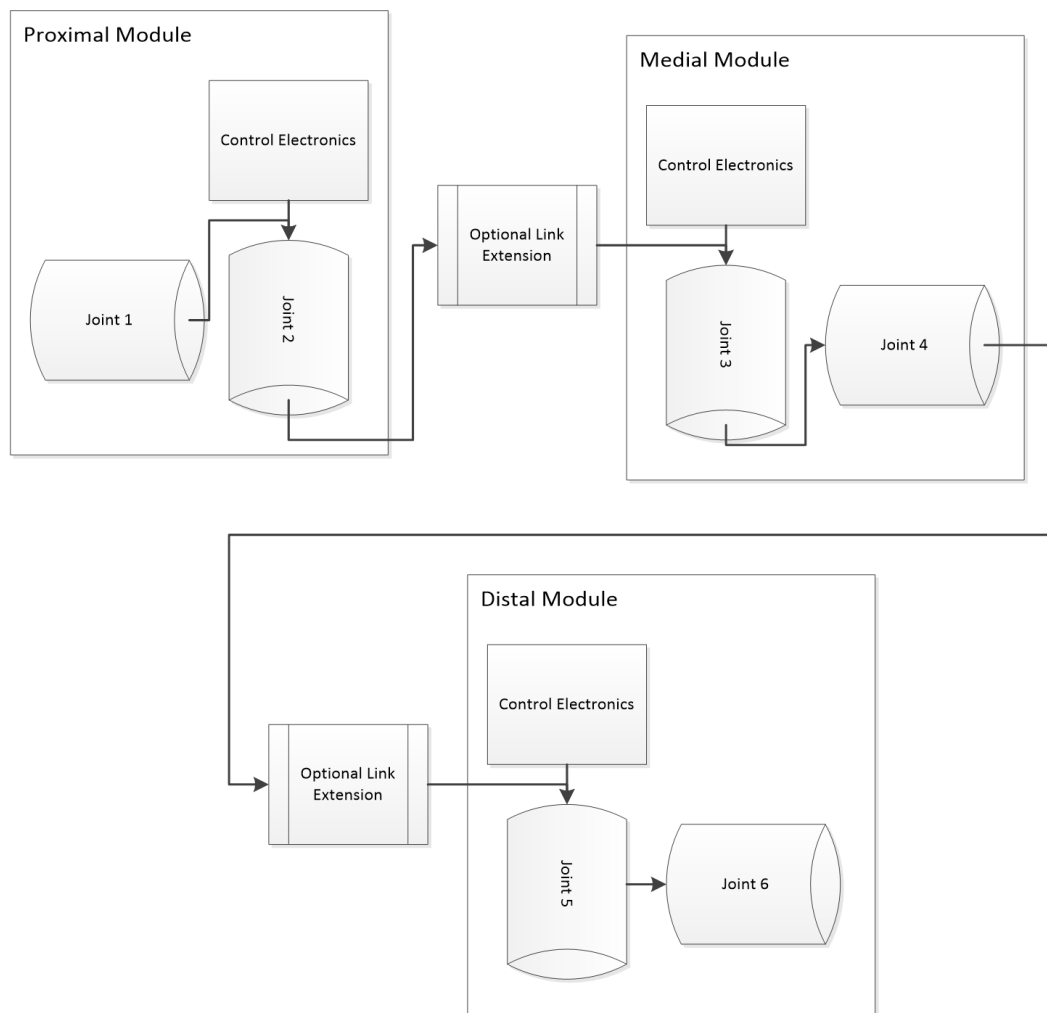
A goal of this design was to reduce the part count and manufacturing complexity from the previous design. Comparing current production costs with accounts of previous costs, this appears to have been an effective method. This design makes use of off-the-shelf components as much as possible, even using the prototyping breakout board for the servo drivers instead of producing our own. Using so many off-the-shelf components does present many other design constraints, as evidenced from the extensive design work done to package the large servo driver package. This appears to have been a worth while pursuit, but this may not be fully understood until the improved RTSX design has been in service for several years.

Appendices

Appendix A: RTSX DXE Kinematic Chain



Appendix B: RTSX PXL Kinematic Chain



Appendix C: Experimental Results Studying Minimal Parent Material Geometry About a Threaded Surface

In order to better understand the failure mode of a threaded surface and to establish minimum geometry for surrounding material, a test was designed to examine parent material during a bolt pullout event. Prior to this experiment, it was conceptualized that failure could occur at any of the helical threads, depending on the ratio of the tensile load taken by each thread [13]. The thread loading distribution is assumed to be approximately 30% on the first three threads because helical inserts are used. Otherwise it may be near 80% on the first thread.

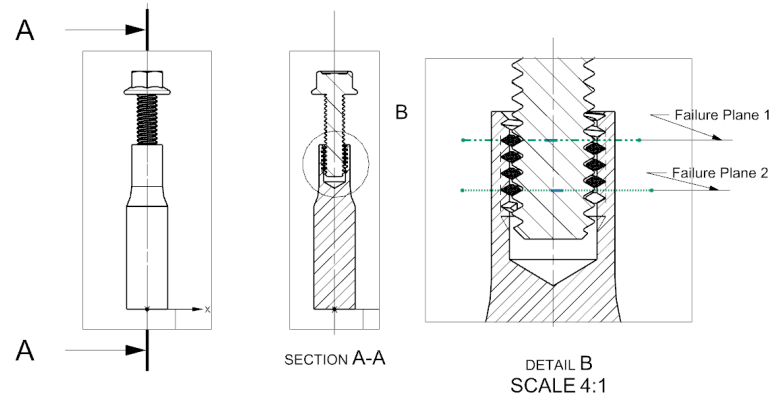


Figure C.1: Detailed cross section of the test sample

C.1 Experimental Setup

Forty two test samples were machined from 5/8 inch aluminum stock with varying diameters about the threaded area. Six samples of each diameter, ranging from 0.35 to 0.6 inches were machined and inspected in multiple dimensions to conform to the mechanical drawing in Figure C.2. This inspection included four diameters taken about the necked area to ensure concentricity and a Go-NoGo gauge inspection of the tapped feature. Six samples were rejected for not conforming to one or more dimension. It was noted that although all accepted threaded features conformed to the acceptable helical manufacturers standard, their frequency of failure increased along with their batch number, likely due to the wear of the tap used. Six samples were rejected for not conforming to one or more dimension. A helical threaded insert, part number 1185-4CN250, was then inserted into each accepted test sample and its insertion tang was recovered.

The material used was chemically and mechanically evaluated by the manufacturer. A material test report was received from the manufacturer and used as the bulk material properties for this test. While this could have taken into account the statistical deviation of the material, the material properties were merely the average measured properties for simplicity. No significant deviation was found between the samples used in the results of this experiment.

The test was performed using 1/4-20-3B bolts with a yield strength of 160 Ksi, all from the same batch. To ensure there was no damage to the threads due to plastic deformation, bolts were tagged with each destroyed sample and not reused.

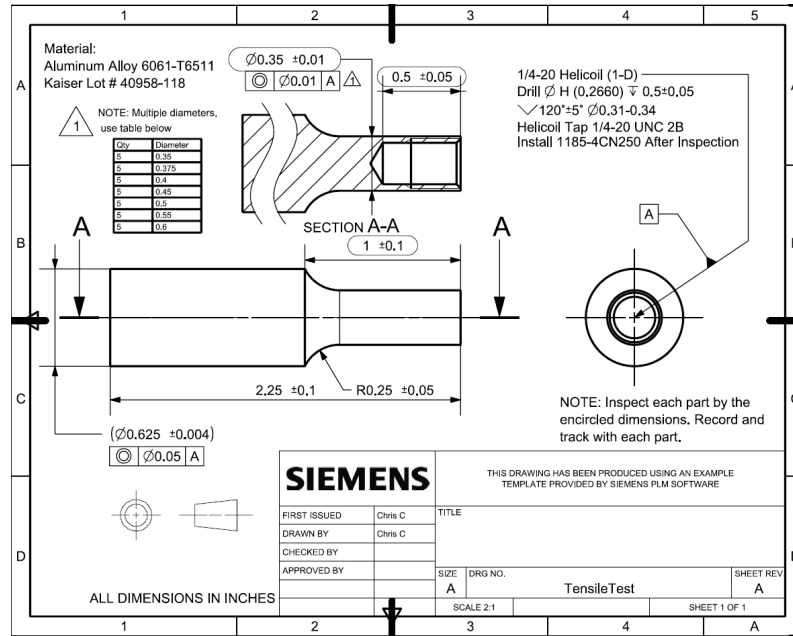


Figure C.2: Mechanical drawing for tensile test samples

An index test was performed using several samples from the batch to confirm their properties. In place of a test sample, the bolts were indexed by being threaded into a Grade 2H double height steel nut with a yield strength of 180 Ksi. This index test found that the bolts were sufficiently strong as to not interfere with the test results. Additionally, no batch defects were found across all of the index bolts. A force-strain chart of all index bolts can be found in figure C.3 below.

C.2 Comparison to Expected Values

Stanley Engineering estimates the pullout force for a 1D helical to be approximately 4200 lbf in aluminum 6061. In this experimental setup, the maximum pullout force was found to be near 4000 lbf, falling close to the manufacturer's value but not matching it. This is of some concern and is addressed in the conclusion of this

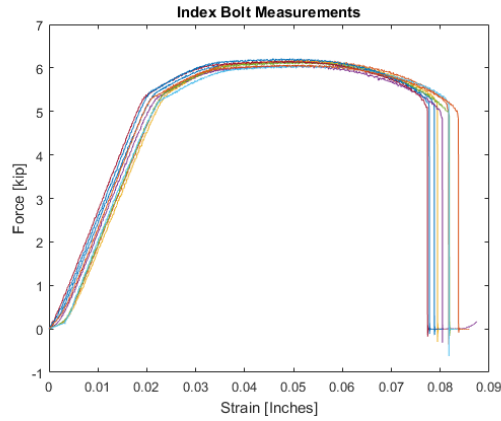


Figure C.3: Index test of bolts until failure

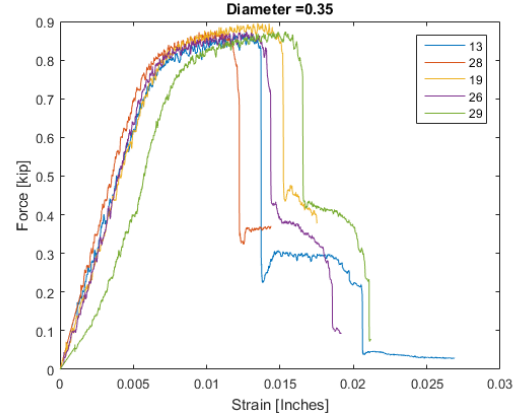


Figure C.4: Sample test results for 0.35 inch diameter billet

Table C.1: Experimental results of test sample failure

Sample Diameter (inches)	Ultimate Tesile Force (kip)	Yield Tensile Force (kip)	Tensile Stress (ksi)		Shear Stress (ksi)	
			Ultimate	Yield	Ultimate	Yield
0.35	0.9	0.7	31.7	24.6	5.5	4.2
0.375	1.5	1.3	35.2	30.5	9.1	7.9
0.4	2.2	1.75	38.0	30.3	1.4	10.6
0.45	3.75	3.2	4.1	35.1	22.8	19.4
0.5	4	3.5	31.1	27.2	24.3	21.2
0.55	4	3.5	23.6	20.6	24.3	21.2
0.6	4	3.5	18.6	16.3	24.3	21.2

appendix.

Comparing these values to the experimental material properties provided by the material manufacturer, the effect of parent material geometry becomes very apparent. Observing the failure methods visually during testing, the transition region between failing in tension and thread pullout is about the 0.45 diameter region. Inspection of the results in Figure 86 show 0.45 inches as the region of maximum tensile failure. As a point of comparison, % of Max Load compares the tensile failure force to the maximum pullout force according to the helical insert manufacturer. Total yield and ultimate forces reach their maximum at a diameter

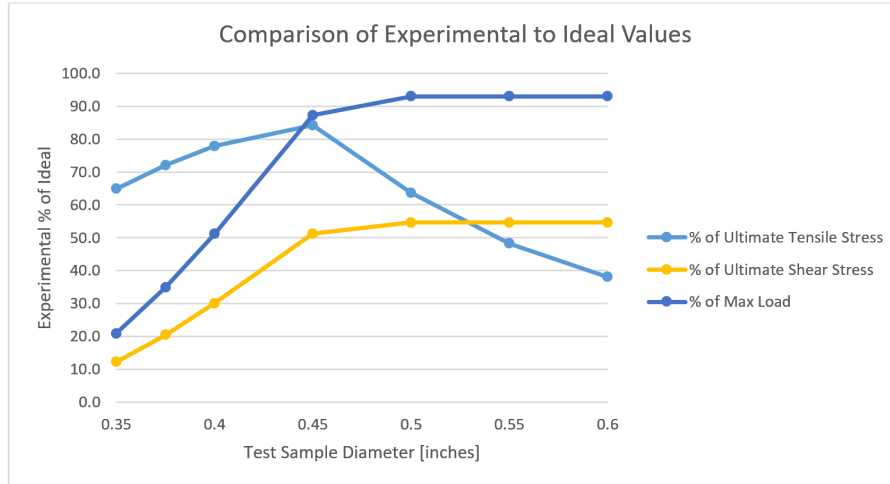


Figure C.5: Comparison of experimental results against ideal results

of one-half inch.

Figure C.6 and figure C.7 illustrate the differences between tensile failure and thread pullout. Note the region one-quarter of the length from the top of the test sample in Figure C.6. This is a tensile failure point directly after the helical insert. This showed that there was no failure within the helical insert itself, but the exact distribution of yield within the last few threads is questionable.

C.3 Conclusions

This experiment demonstrated that, for a bolted connection, the maximum tensile strength can be achieved by having the parent material threads fail in shear before the parent material fails in tension. For a 1/4-20 1D helical connection, the tensile yield force was found to be approximately 85% of the manufacturer's yield strength. While this may have been due to a manufacturing defect, it would be wise to apply a 1.2 safety factor to the presumed failure load of a helical connection.

The region of peak strength begins just after the intersection between tensile and pullout failure. By this observation we can infer that the minimum amount of bulk material about a threaded feature should result in a shearing or pullout failure to maximize strength to weight ratio of the joint. This is in keeping with the “One-Horse Shay” design principle by the American writer Oliver Wendell Holmes Sr., where in all failure modes should occur at once to maximize the lifetime of the design.

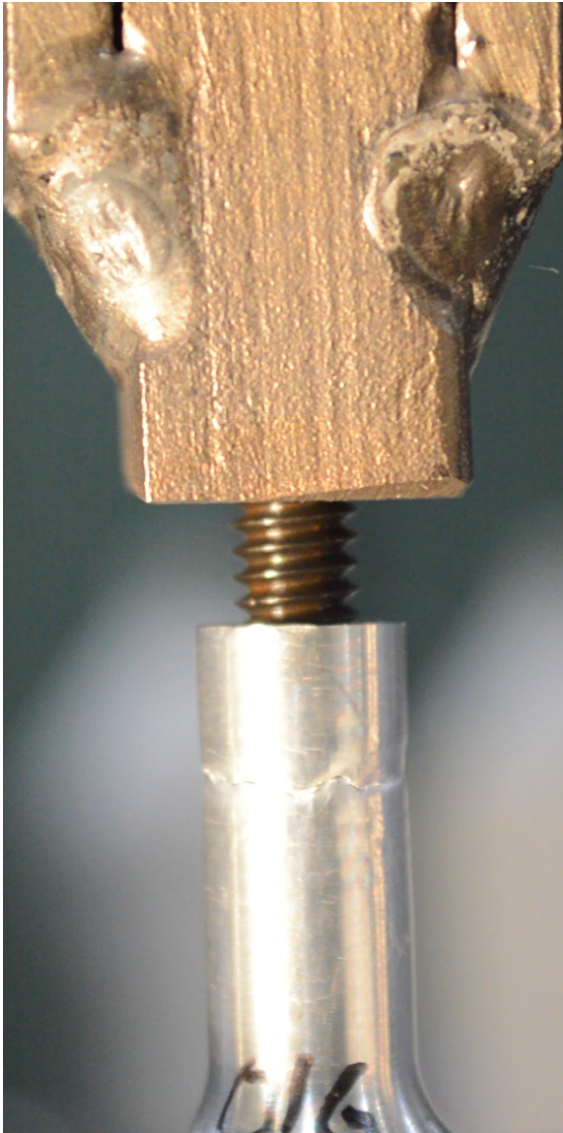


Figure C.6: Test sample 016 showing tensile failure

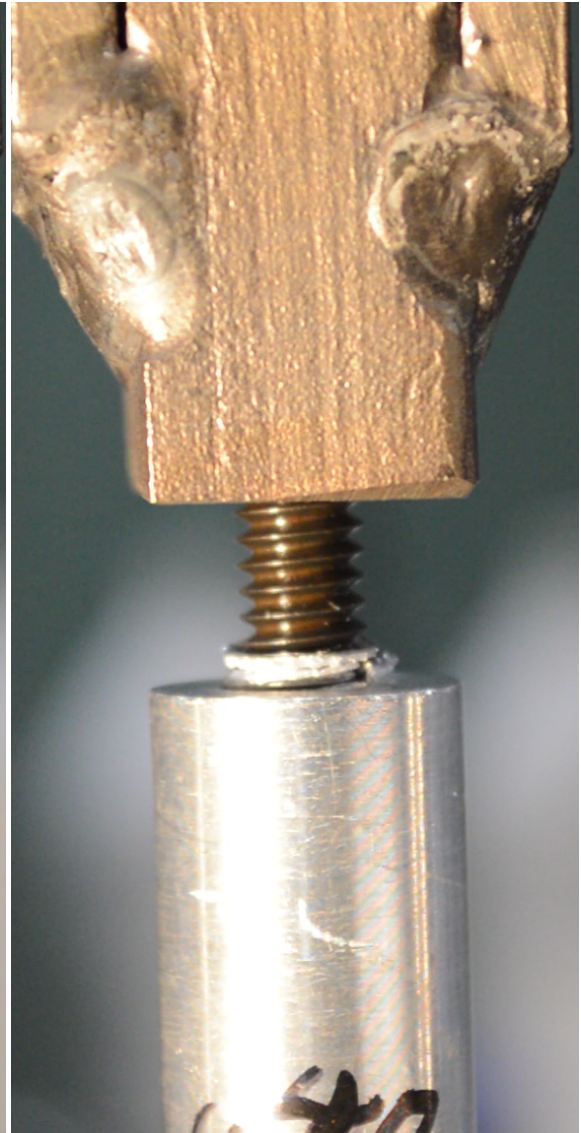


Figure C.7: Test Sample 040 showing pull-out failure

Appendix D: Conceptual Limits for Joint Design

All of the design work contained in this thesis studies the design of the link segments of a serial-link manipulator with revolute joints. To complement this study, an additional design study was conducted to characterize the design limits of the revolute joints themselves. This study was conducted using data from previous space-based manipulators and actuators, as well as off the shelf industry designs for powertrains.

This design study was conducted for a specific application. Many space based manipulators are currently used through a long series of tasks, such as the Space Shuttle Remote Manipulator System (SSRMS). Now there is a push for mission-specific robotic manipulators. For example, an asteroid retrieval mission would require a manipulator to contact and capture a rock for return to earth. Such a task would benefit greatly from a dexterous manipulator, but the mass required to make the manipulator resilient and long-lasting would be much better used for sensors and propulsion systems. To better align with future robotic missions, this conceptual design was conducted for a dexterous manipulator with a very limited lifetime.

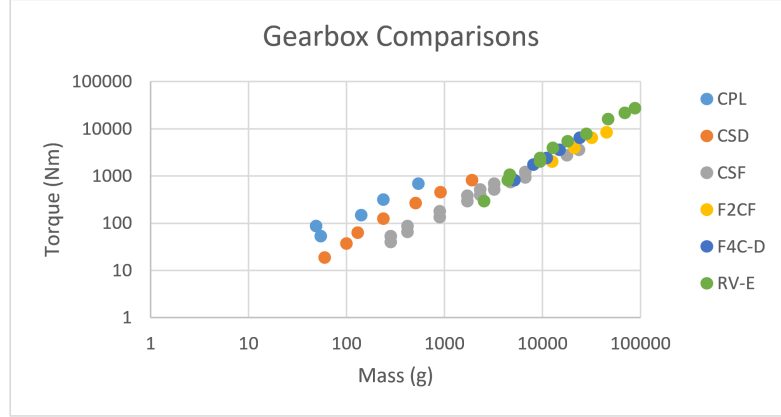


Figure D.1: Comparison of various hypocycloidal gearbox performances

D.1 Powertrain Design

RTSX and many other space-based serial link manipulators have a similar design for their powertrains. The design typically consists of a brushless DC motor that drives a hypocycloidal gearbox, typically a flexspline design such as a harmonic drive gearbox. A systems level review of available brushless DC motors revealed that the high performance torque densities are relatively the same. Various hypocycloidal gearboxes were surveyed, comparing the maximum operating torque with their masses. It was found that the CPL series manufactured by Harmonic Drive was able to yield the highest torque density, which is unsurprising as this model was designed explicitly as a light weight variant of the CSD model.

Several revolute joints were designed using drive train components that were optimized for their specific torque output. This resulted in an actuator torque density on par with flight heritage actuators such as those used on the Pathfinder mission. The number of mechatronic components in the actuator were minimized to a motor, harmonic gearbox, joint bearing, motor bearing and encoder. From

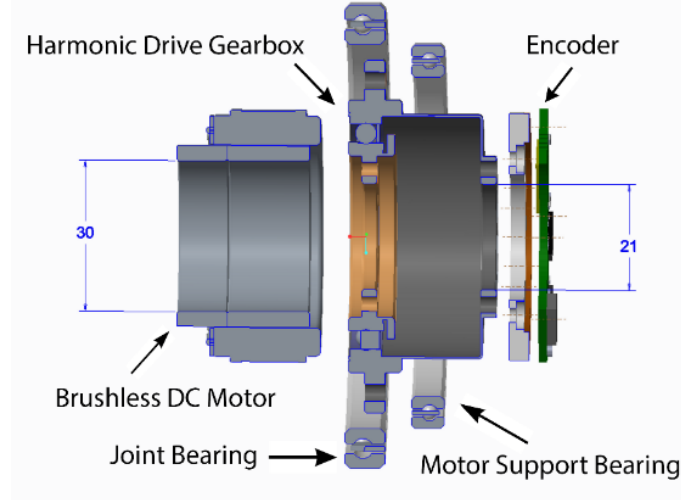


Figure D.2: Baseline arrangement of components inside a robotic joint

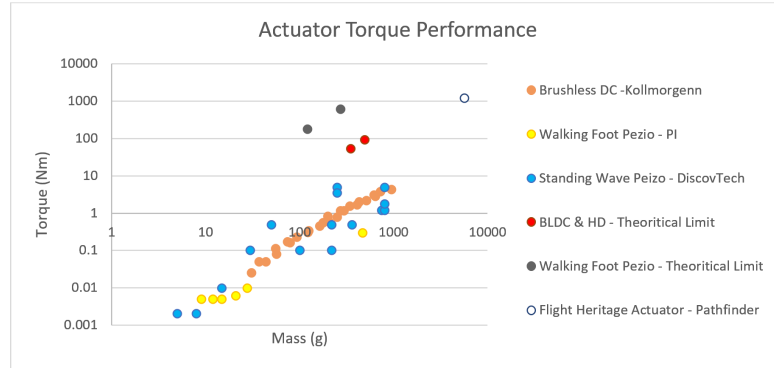


Figure D.3: Surveyed actuator torque performances

this layout it was considered that all intermediate structures could be optimized for minimal mass.

Surveying available actuators and their performances resulted in an unexpected insight. Actuator designs follow the rough formula shown in equation D.1. Values for a and c are dependent on the design of the actuator. The higher the constant values are, the higher the specific torque of the actuator, and thus the more desirable it is in a mass constrained manipulator. While classic brushless direct current motors follow a fairly tight trend, piezoelectric actuators greatly exceed

their performance.

$$Torque \approx a \times mass^{1.5} + c \quad (D.1)$$

D.2 Piezoelectric Motors

Piezoelectric motors are a comparatively recent technology, but are already wide spread in their use. Ultrasonic motors, a subset of piezoelectric motors, were first invented by Toshiiku Sashida [14] in 1980 and are now widely used in areas where a high packing factor and high precision is needed. These motors can commonly be found in the focus mechanism in high end camera lenses.

There are three basic designs for a piezoelectric motor. A standing wave ultrasonic motor, such as Toshiiku Sashida invented, generates harmonic vibrations in a stator ring using an array of piezoelectric devices equally spaced about the stator. Varying the driving frequency results in motion. A traveling wave motor excites a flexible shaft, causing contact points about the perimeter to process as they are forced against each other. The traveling wave motor requires much more hardware than the standing wave motor to generate motion, but locks the rotor in place when unpowered, where the standing wave motor cannot. A walking foot motor uses a pair of conjoined piezo devices to allow the contact point to bend and pull the stator along. This design generates considerably higher forces and has a much higher positioning accuracy.

Piezoelectric motors have had limited implementation in the field of robotics. More commonly, they are found in micro manufacturing, where their exceptionally

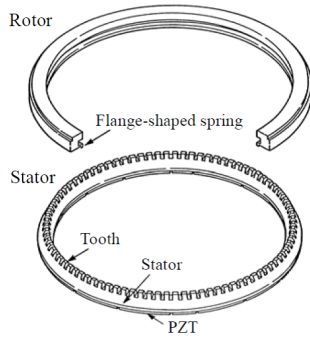


Figure D.4: Standing Wave Motor [15]

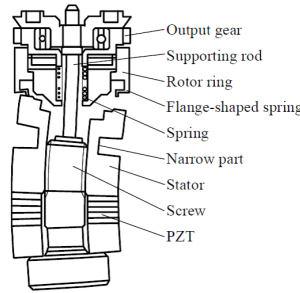


Figure D.5: Traveling Wave Motor [15]

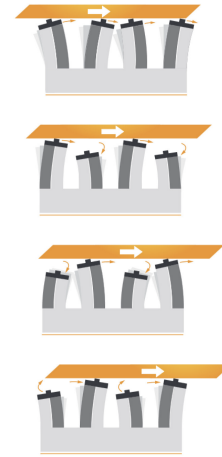


Figure D.6: Walking foot motion [16]

high precision and stiffness is required. These technologies are very mature for that field, but have yet to be designed for a high torque to mass ratio. Even so, this technology has exciting potentials for the field of robotics for several benefits.

1. **High Torque Output Using Direct Drive:** Designs like the Walking Foot actuator have a high power to torque output, eliminating the need for gearing. This also greatly reduces the inertia of the actuator.
2. **High Precision:** High positional accuracy and movement are a must for any robotic actuator. This technology is already being implemented in precision manufacturing for this.
3. **Unpowered Braking:** The Traveling Wave and the Walking Foot actuator both clamp the stator to the rotor when unpowered, eliminating the need for a discrete brake to be added to the powertrain in an actuator.
4. **Low Part Count:** Compared to conventional actuators, the Walking Foot

and the Standing Wave actuator have only two moving parts.

5. **Compact:** With no need to generate a magnetic field and manipulate magnetic flux, all of the volume in Standing Wave and Walking Foot actuators is devoted to mechanical support of the actuator and movement.

After examining these technologies on a systems level, I believe that there is great potential to using piezoelectric motors in robotics and their application should be further researched and matured.

D.3 Bearing Design

A trade study was conducted for selecting bearing sets to be used in the actuator. The force that governs the sizing of bearings is the rocking moment on the joint. Instead of relying on the separation distance and radial reaction force of a pair of bearings to resist a rocking moment, angular contact bearing pairs are treated differently. The rocking moment does not push radially on the bearings, instead it uses the virtual distance between the conical tips of the contact lines of the ball bearings. This virtual distance, also known as the resistance moment arm, is visualized in Figure 96. While matched angular contact bearings are typically used to resist rocking moments, there is a design space in which they are not necessarily as efficient.

Thin section angular contact bearings are frequently used in the configuration above. They can be pre-loaded by external geometry and fasteners, eliminating any non-linearity in the system. However, two angular contact bearings packaged back

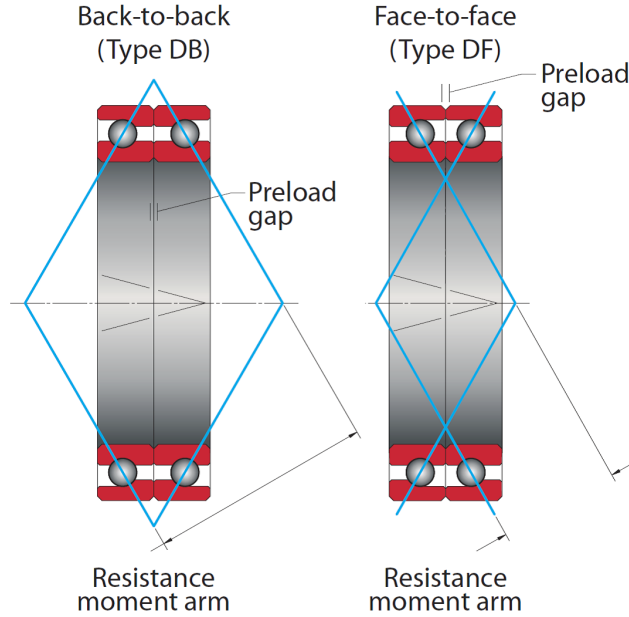


Figure D.7: Geometry depicting how angular contact bearings resist rocking moments [17]

to back have approximately 15% higher moment carrying capacity than a single four point contact bearing, while massing twice as much. Four point contact bearings can be pre-loaded by assembling them with oversized ball bearings, eliminating their non-linearity. This method of preloading works but is not nearly as precise or as fatigue resistant as that used for a pair of angular contact bearings. For our purposes, this is acceptable.

D.4 Kinematic Configuration

The minimal mass joint concept was designed into a notional serial-link manipulator called Strongman. This serial-link manipulator was envisioned to mimic the basic kinematics of the human arm while matching the performance. The design

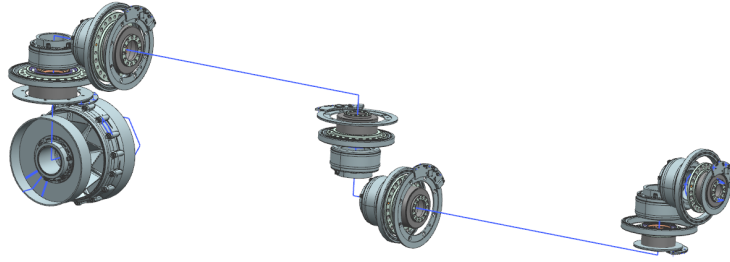


Figure D.8: Mockup of the light weight actuators inside the kinematic chain of Strongman

goal for the whole manipulator system was to mass under 5kg for use on a small satellite. RTSX omitted as many joint offsets as possible to reduce the systems kinematic complexity. This means that pitch joints such as in the elbow and wrist require bearings on both sides of the joint to react the load. Strongman ignores this requirement to reduce the total mass of the system at the cost of increased computational complexity.

Strongman is designed to operate with a tip load of 9 kg on earth and generate a torque at the tool tip of 20 Nm. To increase the tip mass, the powertrain for each joint is reduced successively to optimize for total system mass. The shoulder joints require a maximum torque of 90 Nm, the elbows need 54 Nm, and the wrist requires an output of 20 Nm. The mass of all the actuators in the system is 2.2 kg, leaving 2.8 kg for structure, wiring, and electronics.

D.5 Mechanical Design

The preliminary mechanical design of Strongman was conducted to minimize the mass of the manipulator while still maintaining the same waterproofing that

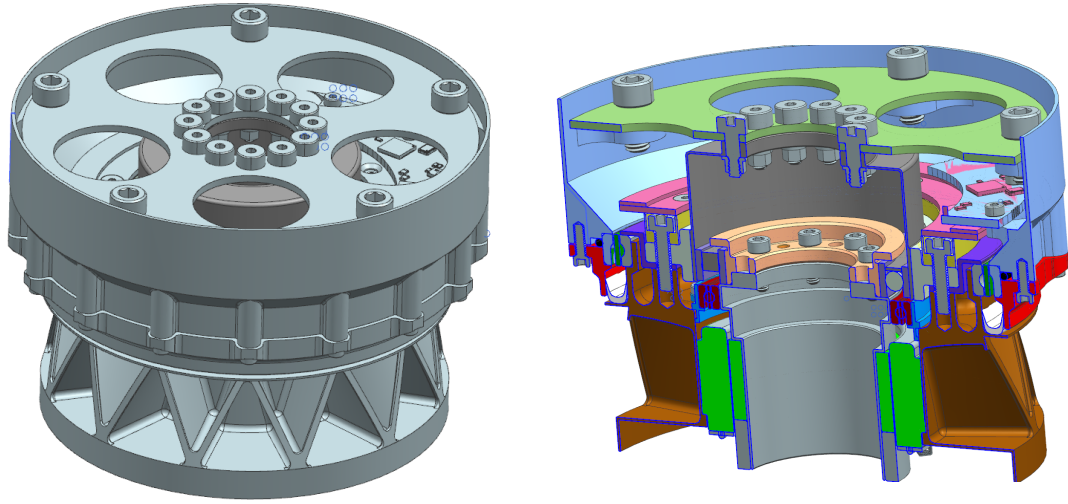


Figure D.10: Strongman joint cross section

Figure D.9: Strongman joint structural design

RTSX has. The intent was to maintain a minimum safety factor of two above the maximum actuator loads. The joint structure was designed to be manufactured from aluminum using an additive process such as Selective Laser Melting (SLM). Strongmans structure was limited to a minimum thickness of 0.040 inches for manufacturability.

The structural ribs surrounding the brushless DC motor, pictured in green in Figure D.10, serve to fill the void left by the small diameter of the stator. These also serve as a radiative cooler for the motor, increasing the effective view factor directly about the motor. The ribs are sized to withstand buckling modes; however, vibrational modes were not studied, and would need to be.

Another mass minimization technique used in the design of Strongman was the use of composite layup for the thin walled link tubes. This presents a myriad of challenges, including how to properly seal the composite from water intrusion, how

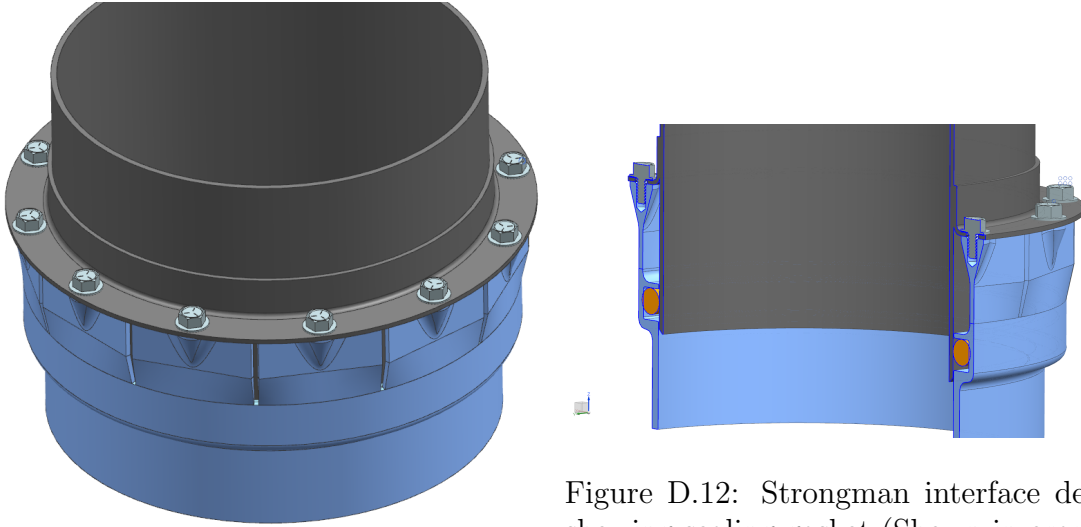


Figure D.12: Strongman interface detail showing sealing gasket (Shown in orange)

Figure D.11: Strongman joint-link interface

to mechanically mate to the composite, and how to design for the large difference in coefficient of thermal expansion. Preliminary solutions were found for all of these challenges and were added to the link design.

To allow for a bolted interface, a pre-fabricated composite flange is adhered to the exterior of the composite link tube. The composite link is attached to the metallic structure of Strongmans joints by a series of circumferential shear clips. These are designed to eliminate stresses caused by radial thermal expansion of the joint, and still carry the structural loads of the serial link manipulator. The tapered parent material about the threaded feature uses geometry established in the experimental study detailed in Appendix C. At the base of the joint sits an o-ring to seal the interior of Strongman from the environment. This o-ring is highlighted in orange in Figure D.12.

D.6 Design Study Conclusions

This design study was conducted to observe the highest performance design space possible for a serial link manipulator. The design was conducted with the goal of minimizing the manipulator mass, which in turn reduced the load requirement for the joints when operating in Earth's gravity. Strongman is designed to lift 9 kg in earth gravity and has a mass of under 5kg. By comparison, RTSX DXE is designed to lift 9kg at full extension and has a mass of nearly 200kg. The DXE design emphasized tip manipulability, packing three motors and two tool drives into the wrist. This had a large weight penalty associated with it, but resulted in a more dexterous system.

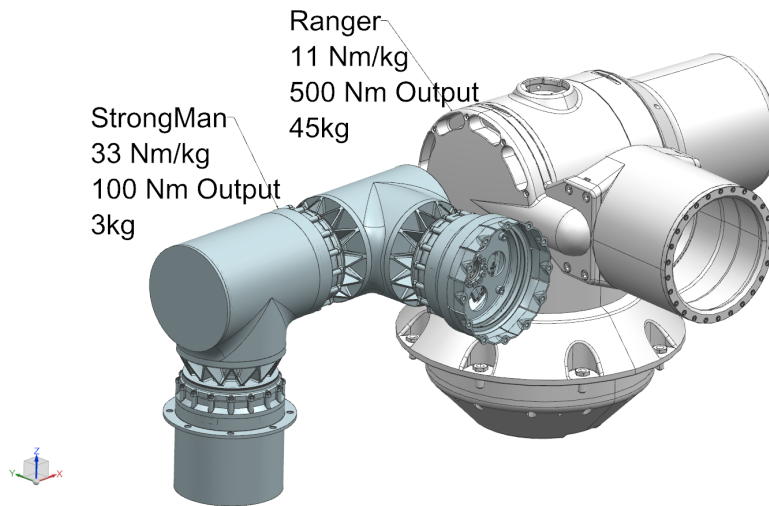


Figure D.13: Comparison of Strongman shoulder with RTSX DXE Shoulder

Strongman would present a new design paradigm for space robotics. By making system mass and cost lower by an order of magnitude, it may make the use of robotic manipulators far more appealing to systems engineers. Many actuators and

mechanisms used in space today operate for only a limited number of cycles, but this has not been allowed for robotic manipulators yet. Assuming a very limited cycle life on a dexterous robotic manipulator could allow a single manipulator to replace many of the deploying actuators on a vehicle, and thereby reducing mass and cost. Strongman may also be an enabling technology for more complex experiments on small satellites, allowing experiments to be conducted on-board a small satellite that would normally be performed by a human.

Appendix E: Wire Harnessing Guide

This appendix page is an example of one of the wiring control documents for the design of RTSX. This is designed to include all necessary information and background for mechanical design.

E.1 Connector P4

Connection Overview:

This connector provides the power to run the Servo Driver logic (known colloquially as Control Power) and multiple I/O connections to the distribution board. Pins 1 and 2 carry control power, pin 4 is an analog pin read by the Servo Drivers ADC, and all remaining pins are for digital communication. Not all digital pins may be used, but for the purpose of this document we will treat them as fully populated.

Connector Type:

Molex: P/N 51353-1600 (housing)
56134-9100 (contacts)

Table E.1: Connector P4 Pinout Wire Chart

Pin#	USED	AWG	Logical Name
1	YES	20	+5V Logic
2	YES	20	GND
3	YES	26	PDI-3
4	YES	26	PAI-1+(REF +)
5	YES	26	PDI-2
6	NO	-	PAI-1-(REF -)
7	YES	26	PDI-1
8	YES	26	PDO-3
9	YES	26	GND
10	YES	26	PDO-2
11	YES	26	PDI-5+
12	YES	26	PDO-1
13	YES	26	PDI-5-
14	YES	26	PDI-5+
15	YES	26	GND
16	YES	26	PDI-4-

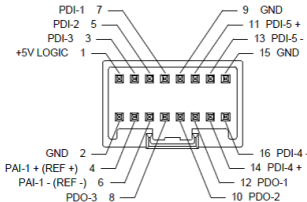


Figure E.1: Connector P4 Pinout

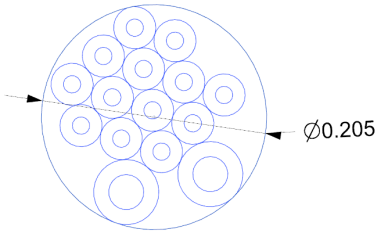


Figure E.2: Connector P4 cable cross section, showin in inches

Appendix F: Interpart Connections

The flow of design requirements and interfaces is traditionally done by forming interface control documents and manually checking for compliance. To decrease design time, this process was automated within the Siemens design software. Interfaces in the form of numerical values, two dimensional geometry, and even complex surfaces are linked between components in this design.

The Interpart connections follow almost the exact same structure as the design tree. Note the similarities between Figure 6.1 and Figure F.1. The only discrepancies occur between the structures are due to the design history associated. The Interpart tree persists across all design revisions, so components that were deprecated still exist on the tree. In Figure F.1 the part “BackBone Top Template V3” was eliminated from the design, but its model is still dependent on variables in “Rack Template V4. ”

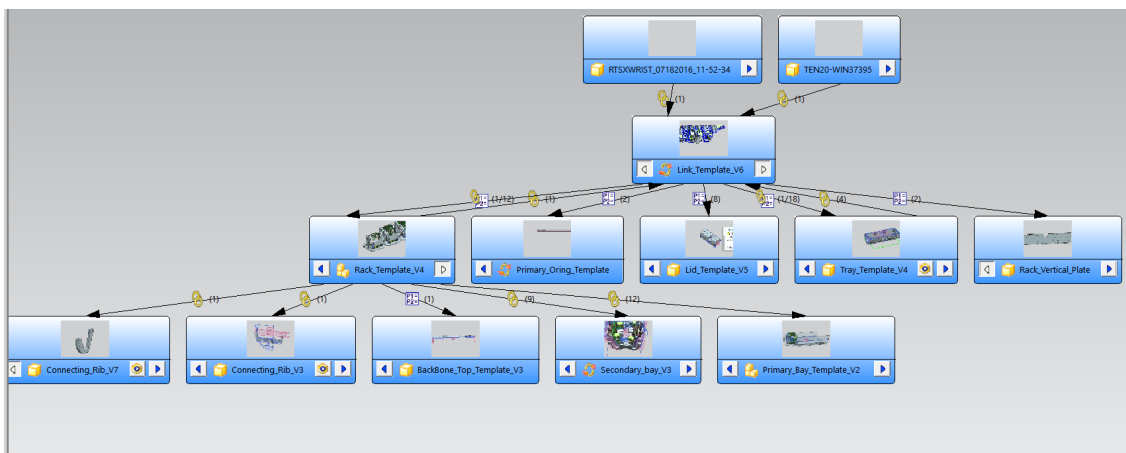


Figure F.1: Sample of RTSX Interpart Tree, generated using Siemens NX

Bibliography

- [1] McDonnell Douglas Astronautics Company, *NASA CR-124075*, 1973. Produced for NASA.
- [2] Seimens, *Design Sensitivity and Optimization User's Guide*. Seimens Product Lifecycle Management Software Inc., 2014.
- [3] M.-Z. Lee, "How bolt patterns react to external loads," *Machine Design*, pp. 60–74, September 2011.
- [4] K. J. N. Richard G. Budynas, *Shigley's Mechanical Engineering Design*. New Dehli, India: McGraw Hill, 2013.
- [5] "Ces edupack," tech. rep., Grata Material Intelligence, 2016.
- [6] *MIL-A-8625F*, September 1993.
- [7] Atrenne Integrated Solutions, *AIS-WP-OpenVPX-Thermal-Chassis-Management*, 2016.
- [8] D. C. Friedrich, "Precision manufacturing processes applied to miniturization technologies," tech. rep., MTU, 2017.
- [9] A. S. I. F. P. D. D. P. Bergman, Theodore L.; Lavine, *Fundamentals of Heat and Mass Transfer*. No. pg 447-485, John Wiley & Sons, 2011.
- [10] Sanyo Denki, *SanAce38GA28E*.
- [11] Stratasy Ltd., *DOC-34025 Rev. B*, 20016.
- [12] NASA Langley Research Center, *NASA SP-8007 Buckling of Thin-Walled Circular Cylinders*, 1965.
- [13] S.-W. Tseng, "A simplified simulation on loading distribution at bolt threads," tech. rep., Bastio Technologies, Houston, Texas, 2010.

- [14] T. Sashida, *An Introduction to Ultrasonic Motors*. Clarendon Press, January 1994.
- [15] T. Maeno, ed., *Recent Progress of Ultrasonic Motors in Japan*, (Yokohoma, Japan), The First International Workshop on Ultrasonic Motors and Actuators, 2005.
- [16] P. Bendixen, “Nanometer positioning wit piezo legs and dmc-30019 galil controller,” tech. rep., PI, 2014.
- [17] R. Roos, “The Importance of Properly Mounted Thin Section Bearings,” tech. rep., Kaydon Bearings, 2014.